Gesellschaft für Mikro- und Nanoelektronik

GMe Forum 2011

Proceedings of the Seminar at the
Vienna University of Technology

Organized by the
Society for Micro- and Nanoelectronics
(Gesellschaft für Mikro- und Nanoelektronik – GMe)

April 14 and 15, 2011

Gesellschaft für Mikro- und Nanoelektronik

GMe Forum 2011

Proceedings of the Seminar at the
Vienna University of Technology

Organized by the
Society for Micro- and Nanoelectronics
(Gesellschaft für Mikro- und Nanoelektronik – GMe)

April 14 and 15, 2011

Sponsored by:

Gesellschaft für Mikro- und Nanoelektronik
Bundesministerium für Verkehr, Innovation und Technologie

Program Committee:

Bernhard Jakoby
Karl Riedling
Friedrich Schäffler
Martin Schrems
Gottfried Strasser
Karl Unterrainer
Michiel Vellekoop

Editor of the Proceedings:

Karl Riedling

Seminar Organization:
Claudia Benedela
Karl Riedling

Production of the Proceedings:
Karl Riedling
Claudia Benedela

ISBN: 978-3-901578-23-6

c/o Technische Universität Wien
Institut für Sensor- und Aktuatorsysteme
Gusshausstrasse 27-29/366, A-1040 Vienna

Preface

The GMe Forum continues a long series of seminars on microelectronics technology which have been organized by the Society for Micro- and Nanoelectronics (*Gesellschaft für Mikro- und Nanoelektronik* – GMe; originally "*Gesellschaft für Mikroelektronik*") since its foundation in the mid-1980s. The original seminars addressed a purely academic audience. The first GMe Forum in its current form has taken place at the Vienna University of Technology in 2001. The GMe Forum is designed to appeal to university researchers as well as to more application-oriented participants, particularly from Austrian industrial enterprises and governmental organizations. Most of the oral presentations are reviews presented by top-level speakers from international industry and research facilities. A number of Austrian university institutions also present their results as oral presentations or as posters.

The Society for Micro- and Nanoelectronics is mainly financed by the Federal Ministry for Traffic, Innovation and Technology (*Bundesministerium für Verkehr, Innovation und Technologie*). Its goal is to promote micro- and nanoelectronics research and technology at Austrian universities with the main aim to stimulate the transfer of know-how to the Austrian industry. The GMe endeavors to meet its goals by organizing seminars such as the GMe Forum and by fostering the communication between the micro- and nanoelectronics oriented Austrian university groups, thus creating cooperations and synergies by coordinating the introduction of new technology infrastructure in this equipment extensive research field.

We hope that the proceedings will promote the impact of the GMe Forum 2011, and that they will contribute to an even better international cooperation of the Austrian micro- and nanoelectronics research at academic institutions and in industry.

Univ.Prof. Dr. Karl UNTERRAINER
President of the GMe

Ao.Univ.Prof. Dr. Karl RIEDLING
Secretary General of the GMe

Forum Program

Thursday, April 14, 2011

10:00 – 10:30	Welcome, Coffee
10:30 – 11:00	Opening
11:00 – 12:00	**Keynote:** O. HÄBERLEN (Infineon Villach): *Power Semiconductors – Key Enablers for Energy Efficiency* – ***page 3***
	Organic Thin Film Solar Cells:
12:00 – 12:45	M.C. SCHARBER (Konarka Austria Linz): *Organic Thin Film Solar Cells* – ***page 11***
12:45 – 14:00	Lunch Break
	Sensors:
14:00 – 14:45	R. LUCKLUM (Otto-von-Guericke-University Magdeburg): *Merging the Ultrasonic and Acoustic Sensor Principle* – ***page 15***
14:45 – 15:30	J. KASBERGER (RECENDT GmbH, Linz): *An Integrated IR-Sensor for Vibrational IR-Spectroscopy* – ***page 17***
15:30 – 16:30	Poster Session & Coffee Break
16:30 – 17:15	P. ERTL (AIT, Wien): *LAB-ON-A-CHIP: Applications to Cell Biology* – ***page 25***

Friday, April 15, 2011

	Nanostructures and Nanotechnology:
09:30 – 10:15	H. KOSINA (TU Vienna): *Semiconductor Device Modeling: The last 30 Years* – ***page 29***
10:15 – 11:00	A. FONTCUBERTA I MORRAL (EPFL Lausanne): *MBE Growth of III-V Nanowires and Related Heterostructures – Application to Photovoltaics* – ***page 31***
11:00 – 11:30	Coffee Break
11:30 – 12:15	J.P. REITHMAIER (University Kassel): *Next Generation of Quantum Dot Devices Based on Tailored Nanostructured Materials* – ***page 33***
12:15 – 13:00	G. SPRINGHOLZ (JKU Linz): *Mid Infrared Active Quantum Dots* – ***page 35***

Poster Presentations

Photonics and Optoelectronics:

Nanostructures and Quantum Devices:

Novel Materials and Technologies:

Sensors:

List of Participants

Dr. Nadja ADAMOVIC
Technische Universität Wien
Institut für Sensor- und Aktuatorsysteme
A-1040 Wien

Dipl.-Phys. Alexander ALEXEWICZ
TU Wien
A-1040 Wien

Dr. Aaron Maxwell ANDREWS
Technische Universität Wien
Institut für Festkörperelektronik
A-1040 Wien

Ermin ARNAUTOVIC
A-1200 Wien

O.Univ.-Prof. Dr. Günther BAUER
Johannes Kepler Universität Linz
Inst. f. Halbleiterphysik und Festkörperphysik
A-4040 Linz

Alexander BENZ
TU Wien
Institut für Photonik
A-1040 Wien

O.Univ.-Prof. Dr. Emmerich BERTAGNOLLI
Technische Universität Wien
Institut für Festkörperelektronik
A-1040 Wien

Ole BETHGE
Technische Universität Wien
Institut für Festkörperelektronik
A-1040 Wien

Felicia BRAME
A-1050 Wien

Dipl.-Ing. Martin BRANDSTETTER
Technische Universität Wien
A-1040 Wien

Dr. Gerhard BRUNTHALER
Johannes Kepler Universität Linz
Inst. f. Halbleiterphysik und Festkörperphysik
A-4040 Linz

Dipl.-Ing. Samir CERIMOVIC
Technische Universität Wien
Institut für Sensor- und Aktuatorsysteme
A-1040 Wien

Stefan CLARA
Johannes Kepler Universität Linz
Inst. f. Halbleiterphysik und Festkörperphysik
A-4040 Linz

Dipl.-Ing. Hermann DETZ

Dipl.-Ing. Mathias EBERL
A-2123 Unterolberndorf

Dr. Peter ERTL
AIT Austrian Institut of Technology GmbH
A-1190 Wien

Dr. Anna FONTCUBERTA I MORRAL
École polytechnique fédérale de Lausanne EPFL
CH-1015 Lausanne

Prof. Dr. Günter FÜRNSINN
TAVR
A-1010 Wien

Marco GAVAGNIN
Technische Universität Wien
Institut für Festkörperelektronik
A-1040 Wien

Martin GLASER
Johannes Kepler Universität Linz
Inst. f. Halbleiterphysik und Festkörperphysik
A-4040 Linz

O.Univ.-Prof. Dr. Erich GORNIK
Technische Universität Wien
Institut für Festkörperelektronik
A-1040 Wien

Dipl.-Ing. Heiko GROISS
Johannes Kepler Universität Linz
Inst. f. Halbleiterphysik und Festkörperphysik
A-4040 Linz

BSc. Peter GRUBER
A-8240 Friedberg

Dr. Oliver HÄBERLEN
Infineon Villach
9500 Villach

Florian HACKL
Johannes Kepler Universität Linz
Inst. f. Halbleiterphysik und Festkörperphysik
A-4040 Linz

Dipl.-Ing. Christoph HAIDEN
Technische Universität Wien
Institut für Sensor- und Aktuatorsysteme
A-1040 Wien

Alma HALILOVIC
Johannes Kepler Universität Linz
Inst. f. Halbleiterphysik und Festkörperphysik
A-4040 Linz

Dipl.-Ing. Martin HEINISCH
Johannes Kepler Universität Linz
Inst. f. Halbleiterphysik und Festkörperphysik
A-4040 Linz

Wolfgang HILBER
Johannes Kepler Universität Linz
Institut für Mikroelektronik und Mikrosensorik
A-4040 Linz

Dipl.-Ing. Astrid HOCHREINER
Johannes Kepler Universität Linz
Inst. f. Halbleiterphysik und Festkörperphysik
A-4040 Linz

Martin HOLZBAUER
A-2860 Kirchschlag

Mag. Nina HRAUDA
Johannes Kepler Universität Linz
Institute of Semiconductor and Solid State Physics
A-4040 Linz

Dipl.-Ing. Markus HUMER
Johannes Kepler Universität Linz
Institute of Semiconductor and Solid State Physics
A-4040 Linz

Bassem ISMAIL
A-1220 Wien

Univ.-Prof. Dr. Bernhard JAKOBY
Johannes Kepler Universität Linz
Institut für Mikroelektronik und Mikrosensorik
A-4040 Linz

Dipl.-Ing. Stefan KALCHMAIR
Technische Universität Wien
Institut für Festkörperelektronik
A-1040 Wien

BSc. Tobias KAPOSI
A-1180 Wien

Dr. Jürgen KASBERGER
Research Center for Non Destructive Testing GmbH (RECENDT)
A-4020 Linz

Dr. Michael KAST
EV Group E. Thallner GmbH
A-4782 St. Florian am Inn

Dipl.-Ing. Christian KOLLER
VCQ - TU Wien Atominstitut
A-1020 Wien

Ao.Univ.-Prof. Dr. Hans KOSINA
Technische Universität Wien
Institut für Mikroelektronik
A-1040 Wien

BSc. Sebastian KRAL
A-1140 Wien

Dipl.-Ing. Elisabeth LAUSECKER
Johannes Kepler Universität Linz
Inst. f. Halbleiterphysik und Festkörperphysik
A-4040 Linz

Mag. Thomas LEDERER
Johannes Kepler Universität Linz
Inst. f. Halbleiterphysik und Festkörperphysik
A-4040 Linz

Dr. Ralf LUCKLUM
Otto-von-Guericke-Universität Magdeburg, Institut für Mikro- und Sensorsysteme (IMOS), Lehrstuhl für Meßtechnik/Sensorik
D-39016 Magdeburg

O.Univ.-Prof. Dr. Gottfried MAGERL
Technische Universität Wien
Dekanat der Fakultät für Elektrotechnik und Informationstechnik
A-1040 Wien

Bernhard MANDL
Johannes Kepler Universität Linz
Institute of Semiconductor and Solid State Physics
A-4040 Linz

Dr. Jovan MÁTOVIC
Technische Universität Wien
Institut für Sensor- und Aktuatorsysteme
A-1040 Wien

M.Sc. Nicola MOSCELLI
Technische Universität Wien
Institut für Sensor- und Aktuatorsysteme
A-1040 Wien

Mahdi MOSSAVAT
A-1140 Wien

Elvis MUJAGIC
A-1040 Wien

Vedad MUJAN
A-1100 Wien

Dipl.-Ing. Alexander PFNIER
Technische Universität Wien
Institut für Festkörperelektronik
A-1040 Wien

Dr. Dionyz POGANY
Technische Universität Wien
Institut für Festkörperelektronik
A-1040 Wien

BSc. Jovana POPOVIC
A-1200 Wien

Dietmar PUCHBERGER-ENENGL
Technische Universität Wien
Institut für Sensor- und Aktuatorsysteme
A-1040 Wien

Peter REININGER
Technische Universität Wien
Institut für Festkörperelektronik
A-1040 Wien

Univ.-Prof. Dr. Johann Peter REITHMAIER
Universität Kassel
Institut für Nanostrukturtechnologie und Analytik
D-34132 Kassel

Ao.Univ.-Prof. Dr. Karl RIEDLING
Technische Universität Wien
Institut für Sensor- und Aktuatorsysteme
A-1040 Wien

Matthias SACHSE
IISS-ÖAW
A- 2700 Wiener Neustadt

Dr. Bolormaa SANDUIJAV
Johannes Kepler Universität Linz
Inst. f. Halbleiterphysik und Festkörperphysik
A-4040 Linz

O.Univ.-Prof. Dr. Friedrich SCHÄFFLER
Johannes Kepler Universität Linz
Inst. f. Halbleiterphysik und Festkörperphysik
A- 4040 Linz

Dr. Markus C. SCHARBER
Konarka Austria Forschungs- u. Entwicklungs GmbH
A-4040 Linz

Julian SCHMID
A-1050 Wien

Univ.-Prof. Dr. Ulrich SCHMID
Technische Universität Wien
A-1040 Wien

Dr. Martin SCHREMS
austriamicrosystems AG
A-8141 Unterpremstaetten

Dr. Werner SCHRENK
Technische Universität Wien
ZMNS
A-1040 Wien

Dipl.-Ing. Clemens SCHWARZER
Technische Universität Wien
Institut für Festkörperelektronik
A-1040 Wien

O.Univ.-Prof. DDr. Siegfried SELBERHERR
Technische Universität Wien
Institut für Mikroelektronik
A-1040 Wien

Giselher SOSTMANN
Agilent Technologies
D-64289 Darmstadt

Ao.Univ.-Prof. Dr. Gunther SPRINGHOLZ
Institut für Halbleiter- und
Festkörperphysik, JKU Linz
A-4040 Linz

Jan STEINKÜHLER
AIT
A-1220 Wien

Univ.-Prof. Dr. Gottfried STRASSER
Technische Universität Wien
Institut für Festkörperelektronik
A-1040 Wien

Dipl.-Ing. Almir TALIC
OeAW
Institut für Integrierte Sensorsysteme
A- 2700 Wiener Neustadt

Univ.-Prof. Dr. Karl UNTERRAINER
Technische Universität Wien
Institut für Photonik
A- 1040 Wien

Michael VELLEKOOP
Technische Universität Wien
Institut für Sensor- und
Aktuatorsysteme
A-1040 Wien

Dipl.-Ing. Heinz WANDA
A-1220 Wien

Dipl.-Ing. Tobias ZEDERBAUER
Technische Universität Wien
Institut für Festkörperelektronik
A-1040 Wien

Dipl.-Ing. Heinz ZWICK
A-1150 Wien

Contents

Keynote

Power Semiconductors – Key Enablers for Energy Efficiency

Oliver Häberlen

Senior Principal Technology Development
Infineon Technologies Austria AG, 9500 Villach, Austria

Introduction

The world wide increase in personal wealth and the growing population is continuously driving the energy consumption and consequently the demand for energy. The world energy consumption has doubled in the past four decades and the trend continues [1]. Forecast is a further rise by 45% in the next 25 years (Fig.1). About one third of this energy is based on electricity. While debate continues over the environmental impact of different means of electricity production, its final form is relatively clean and it is one of the easiest means of transporting energy over long distances.

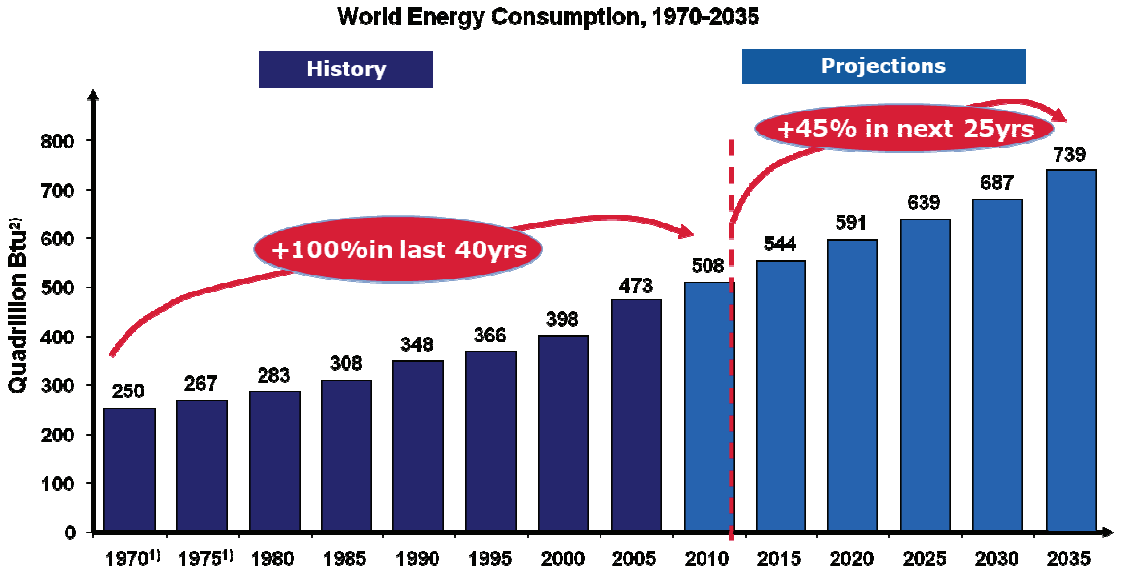

Fig. 1: World Energy Consumption in Btu (*British thermal units*; 1 Btu = 1.05506 kJ) [1]

Power Semiconductors along the Energy Supply Chain

Currently huge amounts of energy are still lost along the electrical energy supply chain (Fig. 2) from generation over distribution to final consumption. This begins with power generation for example from renewable energy sources. Generated power from wind mills has to be transformed from variable frequency AC to the constant frequency of the power grid with highest efficiency and quality. Therefore 100% of generated power is controlled by power semiconductors, namely Insulated Gate Bipolar Transistors (IGBT). Since 1995 the power density of IGBT modules has increased by 300%, allowing conversion efficiencies of 98% today [2]. DC/AC converters transform the energy

from solar cells to the power grid with a world record efficiency of 99% by the use of state-of-the-art IGBTs in conjunction with silicon carbide devices.

Since electricity generation and its consumption are often quite distant (e.g. for offshore wind parks) the power losses during transmission also play an important role. Here thyristors enable HVDC (high voltage direct current) energy transmission across more than 1000 kilometers distance with only 2% losses. Voltage levels used for transmission have reached 800 kV in the meantime. Finally transmission ends in the consumer's world where electricity is being used throughout our daily life spanning from all kinds of electrical motors in industry, transportation, home appliances to lighting and consumer electronics. Every of those previously mentioned conversion steps needs its own adapted power electronics topology which in turn requires specific properties of the power semiconductors.

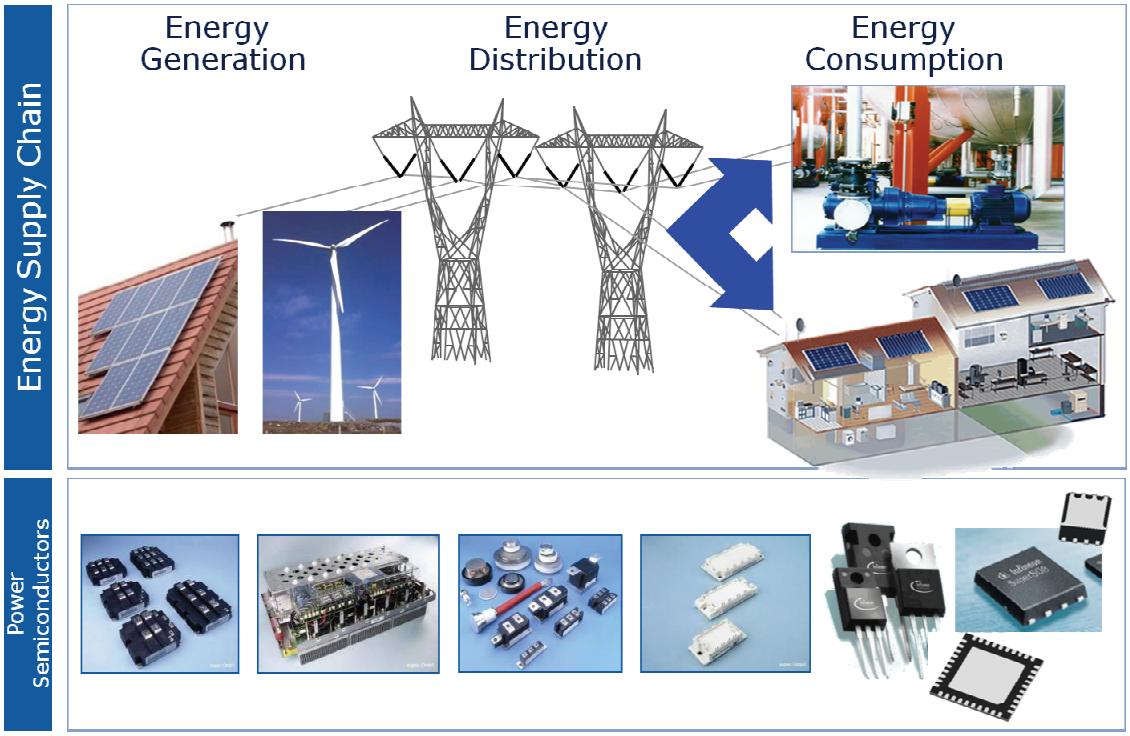

Fig. 2: The energy supply chain from generation to consumption

Modern Power Semiconductors in Energy Conversion

To exemplify the influence of modern power semiconductors on energy conversion efficiency we will have a look at a switched mode power supply (SMPS) that is being used throughout our electronic world from servers in data centers (as being used e.g. by Google) to personal computers and laptops down to chargers for mobile devices.

Main task of a power supply is to convert the power line input (typ. 110V or 220V AC depending on country) to several different DC voltages in the range of 48V, 12V and lower. A modern power supply topology consists of three major functional blocks (besides the input bridge rectifier): the power factor correction stage (PFC), the pulse width modulation stage (PWM) and the secondary rectification stage (see Fig. 3).

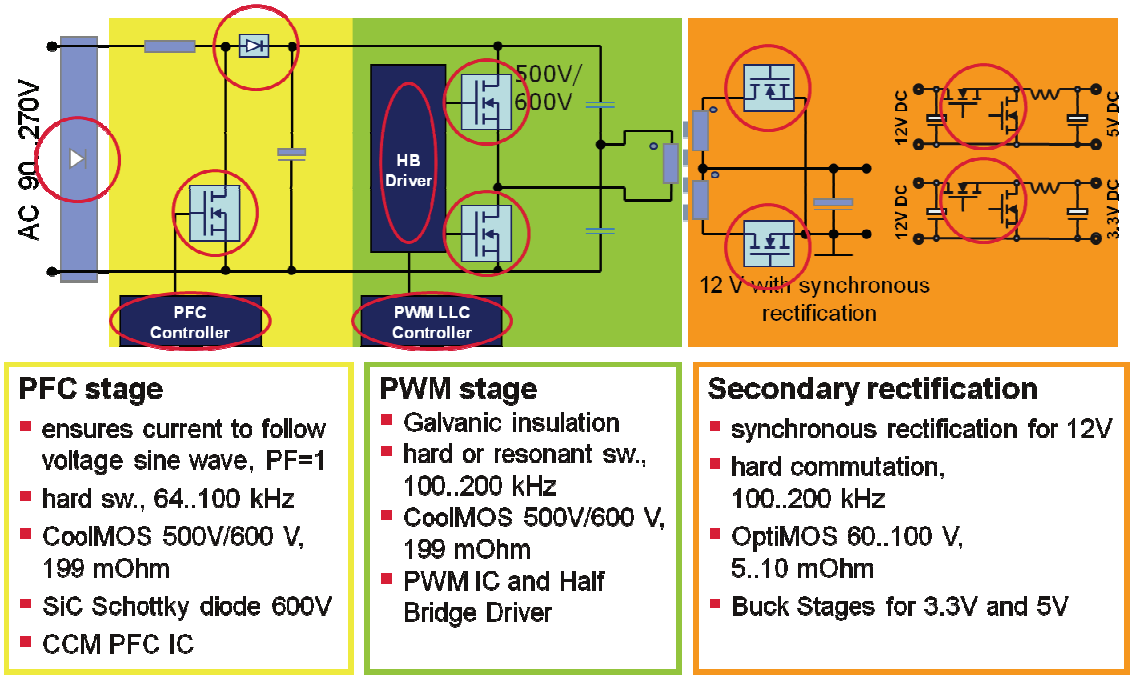

Fig. 3: New circuit topologies need to be combined with advanced power technologies: red circles indicate power semiconductor content

The PFC stage controls the ratio of real power drawn from the line to the unwanted reactive power. There was a change from a passive stage to an active stage in the last decade due to legal restrictions (like the Energy Star regulation in the US). An active PFC stage is typically operated up to 100 kHz, so the demands to the power semiconductors in terms of switching losses are quite challenging. The diode shown in the PFC in Fig. 3 is preferably a Schottky diode to avoid the high amount of stored charge connected to bipolar diodes. Unfortunately silicon as semiconductor material did not allow building Schottky diodes with blocking voltages exceeding 300 V due to the low electric breakdown field of 250 kV/cm. This changed when Infineon started to offer 600 V silicon carbide based Schottky diodes that exploit the new materials' ten times increase in electrical breakdown field of 2.2 MV/cm [3]. These diodes are virtually free of reverse recovery charge due to their unipolar current conduction and allow PFC efficiencies up to 99%.

The PWM stage generates the high frequent input for the primary side of the transformer. Also here the switching losses of the power semiconductors are a key focus due to the frequencies beyond 100 kHz. The half bridge consists of two high voltage power MOSFETs (500 V to 650 V depending on power line) that have to unite two contradicting features: a low on-state resistance to minimize conduction losses and low parasitic capacitances to minimize switching losses at the same time. For a long time progress in high voltage silicon MOS technology seemed to saturate since the on-state resistance was dominated by the voltage sustaining epitaxial drift layer. Through the invention of Infineon's CoolMOS™ which exploits a three dimensional folded source-drain p-n junction throughout the epitaxial drift layer (super junction principle) it was possible to break the so-called silicon limit and shrink the transistors by a factor of 10 since then [4], offering less than 100 mΩ in a standard TO220 package now. The die shrink in turn allowed the reduction of the parasitic capacitances, boosting the efficiency of the PWM stage.

The task of the secondary rectification stage is to convert the high frequent output from the transformer's secondary side to various low DC voltages. For a long time this recti-

fication has been done with fast silicon diodes. This limits the efficiency of the stage as the diodes have a finite voltage drop in forward conduction mode (typ. 0.8 V for silicon pn diodes and 0.4 V for silicon Schottky diodes). The so-called synchronous rectification allows cutting those losses by replacing the diode by an active switch that bypasses the diode voltage drop. This again was made possible by innovation and development of a new type of power semiconductor, namely Infineon's OptiMOS™ series of medium voltage trench MOSFETs. Trench field plates in the epitaxial drift layer allow reducing the on-state resistance below the silicon limit and cut parasitic switching losses at the same time [5].

By replacing standard power semiconductors with modern state-of-the-art power semiconductors like described previously the 70% to 80% typical efficiency of a conventional power supply can be pushed to well above 90% for the whole load range (Fig. 4). With this efficiency jump the about 5 € additional spending in power semiconductors can be amortized within one to two years assuming electricity rates of the western hemisphere [6].

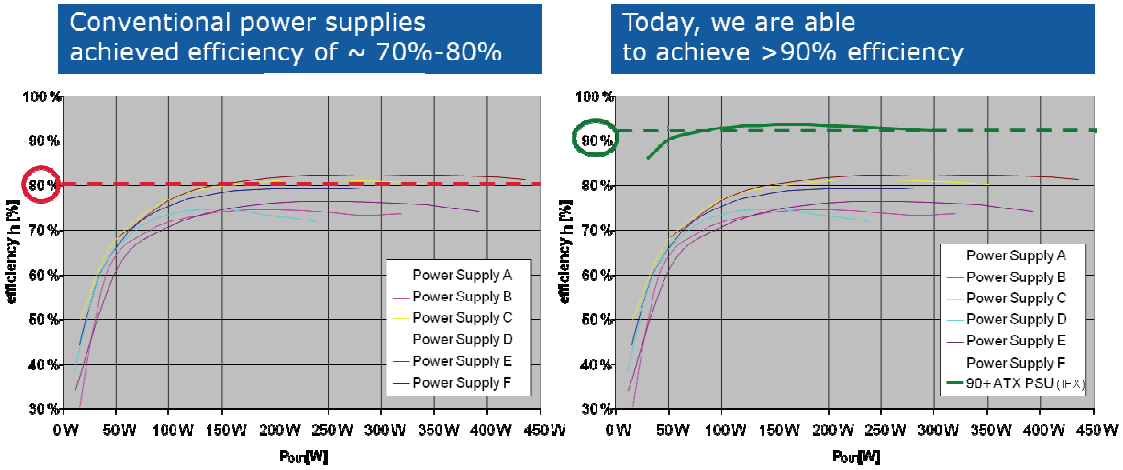

Fig. 4: Comparison of power supplies based on conventional topologies and semiconductors (left diagram) to a power supply with newest topology and leading-edge power semiconductors from Infineon (right diagram, green line)

Summary

Energy is a precious resource and therefore energy efficiency is a key enabler for the future demands of our modern world. The flow of energy from its generation to its final usage undergoes many steps of conversion and therefore the efficiency goal for each conversion step is beyond 99%. This is only possible with the aid of modern power semiconductors. Silicon based technologies like IGBTs, CoolMOS™ and OptiMOS™ have brought efficiency to levels unimagined a decade ago. Emerging technologies based on new semiconductor materials like silicon carbide and gallium nitride will continue this trend for a greener future.

References

[1] Energy Information Administration (EIA), International Energy Outlook 2009, 2010, Infineon estimates based on IEA 2006

[2] M. Hierholzer, T. Laska, M. Loddenkotter, M. Münzer, F. Pfirsch, C. Schäffer, T. Schmidt. 3rd generation of 1200 V IGBT modules, 34th IAS Annual Meeting, Conf. Rec. IEEE, 1999, vol.3, pp. 1787-1792.

[3] I. Zverev, M. Treu, H. Kapels, O. Hellmund, R. Rupp. SiC Schottky rectifiers: Performance, reliability and key application, Proc. 9th Conf. Power Electronics and Applications, 2001, pp. DS2.1-6.

[4] G. Deboy, M. März, J.-P. Stengl, H. Strack, J. Tihanyi and H. Weber. A new generation of high voltage MOSFETs breaks the limit line of silicon, Proc. IEDM, 1998, pp. 683-685.

[5] R. Siemieniec, O. Häberlen, J. Sanchez. Wege zu mehr Effizienz, Design & Elektronik, 09/2009, pp. 10-11.

[6] A. Mittal. Energy Efficiency Enabled by Power Electronics, Proc. IEDM, 2010, pp. 1.2.1-7.

Organic Thin Film Solar Cells

Thin Film Organic Solar Cells: Power Plastic Converting Light to Energy – Anywhere

Markus Scharber

Konarka Austria, Altenbergerstrasse 69, 4040 Linz, Austria
www.konarka.com

Achieving efficient solar energy conversion at both large scale and low cost is one of the most important technological challenges for the near future. In this respect solution-processed thin film organic solar cells have gained serious attention during the last few years. Among all the photovoltaic technologies, organic solar cells are outstanding in their potential as a true low cost photovoltaic technology because of their compatibility to conventional, large volume printing and coating processes.

World wide research in organic solar cells has started around 10 years ago. Since then the number of scientific publications is growing exponentially indicating the enormous interest in this technology. In 2006, about 10 % of the scientific publications in the field of photovoltaics reported on organic solar cells. At the same time the performance of organic solar cells was improving gradually from 1 % in the year 2000 to over 8 % in 2011.

Konarka Technologies is leading the development and commercialization of thin film organic solar cells and launched the first solution-processed thin film organic solar cell product in 2009. The company is currently developing large scale production capabilities and is exploring new materials and components for next generation products with improved performance.

Fig. 1: Portable chargers with Konarka's thin film organic photovoltaic material

In the presentation the basic concepts and advantages of thin film organic solar cells are discussed. Realized and potential applications of thin film organic solar cells will be described and an outlook on the future development of the technology is given.

Fig. 2: Pico/Power Plastic® Lantern

Fig. 3: Transit shelter, San Francisco

Sensors

Merging the Ultrasonic and Microacoustic Sensor Principle

Ralf Lucklum

Institute of Micro and Sensor Systems, Otto-von-Guericke-University, Magdeburg, Germany

Ultrasonic sensors and acoustic (resonant) microsensors are well accepted devices in many application fields. Both principles are based on acoustic wave propagation in a way that the value of interest perturbs wave propagation in a distinct manner. The sensing capabilities of ultrasonic sensors rely on time of flight measurement of an ultrasonic burst traveling through the object of interest. This value can be determined with high accuracy. Similarly, the impressive sensing capabilities of resonant microsensors result from the high Q-factor of the resonator and precise determination of the resonant frequency. Both principles face however, severe limitation in size and integration into microsystems.

Acoustic band gap materials, so-called phononic crystals, provide a new platform for sensing material properties in small cavities. Phononic crystals are periodic composite materials with spatial modulation of acoustically relevant parameters like elasticity, mass density and longitudinal and transverse velocities of elastic waves. Their most exiting feature is the existence of acoustic band gaps, i.e. a frequency range where (ultra)sound cannot propagate through the structure. The sensor concept just recently introduced employs specific transmission windows within the band gap. In this application it is most reasonable that the material of interest constitutes one component of the phononic crystal, e.g., a fluid in the holes of a solid plate. If the value of interest, e.g. the concentration of a contaminant in a liquid mixture, changes its acoustic properties, the acoustic properties of the phononic crystal will change as well.

Transmission or reflection coefficients are appropriate parameters for measurement and used to find a characteristic feature of the phononic crystal. For a sensor application, a transmission peak within the band gap or a transmission dip outside the band gap is the most favorable feature since the respective frequency of maximum/minimum transmission is easy to determine. The sensor scheme therefore relies on the determination of the frequency dependence of maximum/minimum transmission on the physical or chemical value of interest. The transmission peaks can be considered as being based on resonance-like effects, their examination therefore merges basic features of ultrasonic and acoustic microsensors.

Three realizations of the phononic crystal sensor will be introduced. The simplest version is the parallel arrangement of several layers of metal plates and a liquid in between. The transmission properties can be analytically calculated; the results can serve as proof-of-principle. The sensitivity related to those peaks is in the order of macroscopic sensors. Sensors utilizing 2D phononic crystal have been studied in two basic arrangements, with in-plane excitation and detection of waves and an incidence direction perpendicular to the plate. In both realizations a liquid fills all holes of the phononic crystal plate; in the latter case it also covers both surfaces. In the in-plane arrangement specific peaks could be identified which represent changes in liquid properties. When using normal incidence of waves, the extraordinary transmission peak has been found

to be strongly dependent on liquid sound velocity. The effect is more robust and the insertion loss of the device is much lower, an important issue from a practical point of view.

An Integrated IR-Sensor for Vibrational IR-Spectroscopy

Jürgen Kasberger

Research Center for Non Destructive Testing GmbH (RECENDT), Hafenstraße 47-51, 4020 Linz, Austria

Introduction

In industry, a vast variety of processes can be optimized by means of online measurements of chemical properties of fluids in order to reduce costs of maintenance or increase productivity as well as production quality. Considering the vast verity of fluids present in industrial applications suggests the utilization of a vibrational spectroscopic method, which offers high selectivity as well as high sensitivity. As an alternative to commercial IR-spectrometers, which are in general expensive and bulky instruments, different components related to miniaturized spectrometers have been investigated in the recent years. In particular, a lot of work has been done in the field of the spectroscopic measurement method, where a number of publications are dedicated to absorption in the evanescent optical field. The most prominent representatives of optical waveguides are optical fibers, which have been investigated thoroughly (e.g., [1] – [3]). However, due to the geometrical dimensions of conventional fibers, the evanescent field is relatively small and hence a lot of effort has been done to improve the sensitivity, e.g., by means of tapered structures [4], [5]. To exploit the advantages of guided optical waves for measuring purposes, also photonic structures [6] – [9] have been considered.

Working with photonic elements (waveguides), which utilize the absorption in the evanescent field, requires coupling of an optical beam into the waveguide. The guided optical wave of an evanescent field sensor is often excited by means of (slanted) front end coupling (e.g., [6], [8]) or prism coupling [10]. For spectroscopic measurements usually either optical fibers in conjunction with an interferometer or recently quantum cascade lasers (QCL) [11] – [13] are deployed.

In addition to the evanescent field sensor element, a lot of work has also been subjected to miniaturize spectrometers. Most of the work is dedicated to miniaturize the dispersive element [14]. There have also been attempts to integrate a wavelength selective measurement in conjunction with an evanescent field sensor element [15], [16]. For example, in [15] the IR-radiation is excited by heating the suspended waveguide itself, which results in broadband IR-radiation guided in the waveguide. However, due to the applied band-pass filter, the setup is limited to a specific wavelength.

In contrast to [17], [18], where the dispersive features of gratings (couplers) are exploited as a sensing mechanism, we utilize the gratings as dispersive elements as well as for waveguide coupling. Thus, our approach to fully integrate an IR-absorption sensor is different from the work done so far focusing on specific features of single parts of a sensor system like, e.g., grating couplers.

Concept of a Fully Integrated IR-Absorption Sensor

We aim at a fully integrated absorption sensor, as sketched in Fig. 1, based on IR-absorption in the evanescent field of an integrated slab waveguide utilizing thermally generated and detected IR-radiation. For the proposed sensor system, the coupling by means of grating couplers is advantageous, since front end coupling is not suitable for the considered mono-mode waveguide of the proposed setup.

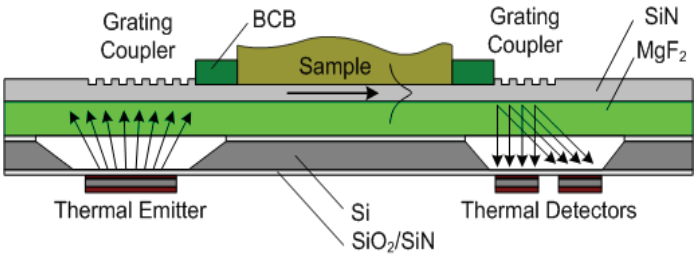

Fig. 1: Concept of a fully integrated sensor system for the mid IR-range. Two grating couplers are utilized (1) to couple broadband IR-radiation into the waveguide and (2) subsequently for spectral separation when coupling out of the waveguide.

The thermal radiation excitation and detection – influencing the design of the grating couplers – was selected due to the targeted mid-IR-region. Even though non-thermal elements exhibit outstanding features like, e.g., the high sensitivity of cryogenic detectors, those non-thermal elements are not suitable for integration into a micro-sensor due to the associated comparatively large dimensions.

In various targeted applications the measurement of the IR-absorption at a limited number of wavelengths is suitable to characterize a certain chemical property. For example, in order to reduce the interval of scheduled maintenance of lubrication oil, e.g., in combustion engines, the quality of the deteriorated oil has to be determined. The occurring oxidation of lubrication oil can be used as monitoring feature for the aging process. Since this oxidation can be characterized by measuring the IR-absorption at two distinct relatively broad wavelength ranges [19], low spectral resolution is required to determine the deterioration of lubrication oil. Therefore, the monitoring of lubrication oil [20], [21] was chosen as example application for the first experimental investigations.

Validation of the Waveguide as Transducer

In order to characterize the proposed mono-mode waveguide as an IR-absorption element, we have fabricated a waveguide structure including two grating couplers with a SiN-waveguide residing on a MgF_2-substrate. The concept of the fully integrated absorption sensor, as shown in Fig. 1, utilizes the angular coupling characteristics of grating couplers for the spectral separation of the measurement wavelength. To characterize the mere waveguide as absorption element, we have built up a measurement setup, where the spectral measurement is done with an IR-spectrometer [23]. For the characterization of the waveguide prototype, comprising the input grating coupler, the waveguide and the output grating coupler, the total transmission through the sample is measured for a certain fixed coupling angle.

In order to demonstrate the sensitivity of the propose mono-mode waveguide, measurements obtained with a commercial ATR-element (three reflections) are compared to

those obtained with our waveguide structure, as shown in Fig. 2. For both evanescent field absorption elements (ATR and mono-mode waveguide) a reference measurement as well as the corresponding oil measurement, where the oil is loaded on top of the waveguide without changing the optical setup, are depicted. The decrease in transmission for the oil measurement compared to the corresponding reference measurement, which is only recognizable for the mono-mode waveguide (Fig. 1), confirms the fundamental sensitivity of the proposed mono-mode waveguide structure. With the obtained sensitivity, this measurement setup can also be applied for monitoring the deterioration of the investigated lubrication oil, as demonstrated in [23].

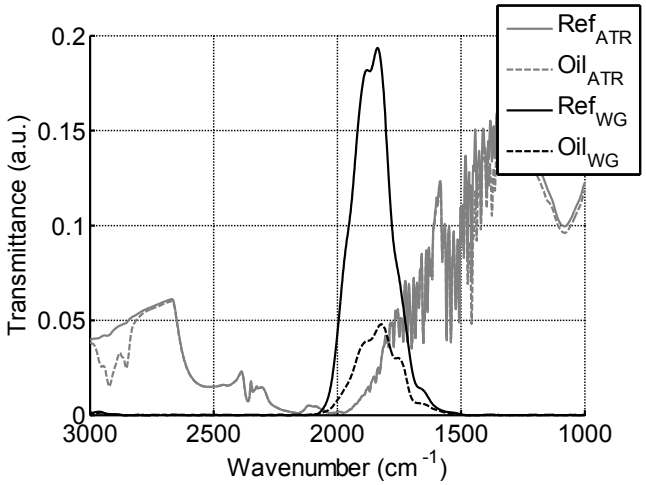

Fig. 2: Total transmission through the gratings and the waveguide of reference (i.e., no oil loaded on the waveguide) and oil measurements. Here a commercial ATR-element and the investigated waveguide prototypes are compared regarding the absorption in the evanescent field of devices.

Application to Deteriorated Lubrication Oil

In order to demonstrate that the concept, depicted in Fig. 1, can be utilized as oil aging sensor, the dispersive manner utilized for spectral separation has to be taken into account. Instead of using two IR-detectors, as shown in Fig. 1, a single element has been positioned with a motorized translation stage to scan the spectral range in the used lab setup.

For the application of the setup as oil aging sensor, the IR-emitter is positioned to obtain the maximum intensity at the IR-detector at about $\nu \approx 1800\text{cm}^{-1}$ ($\lambda = 5.5\mu\text{m}$), which corresponds to a coupling angle of about -10°. The center wavelength of 1800cm^{-1} is chosen due to the special characteristics of the considered lubrication oil, which does not change the absorption below this wavelength but has its typical oxidative absorption above this wavelength [19]. Once the IR-emitter is positioned, a reference measurement (without oil) is carried out followed by an oil sample measurement, where the optical setup is not changed between the reference and the oil measurement. To obtain a normalized transmission curve, characterizing the oil quality, it is necessary to relate the oil measurement to the reference measurement, which results in normalized transmission measurement with respect to the coupling angle. The normalized oil measurements are corrected to match in the region between -12° to -5°, as shown in Fig. 4, corresponding to the spectral region that is not affected by oil oxidation.

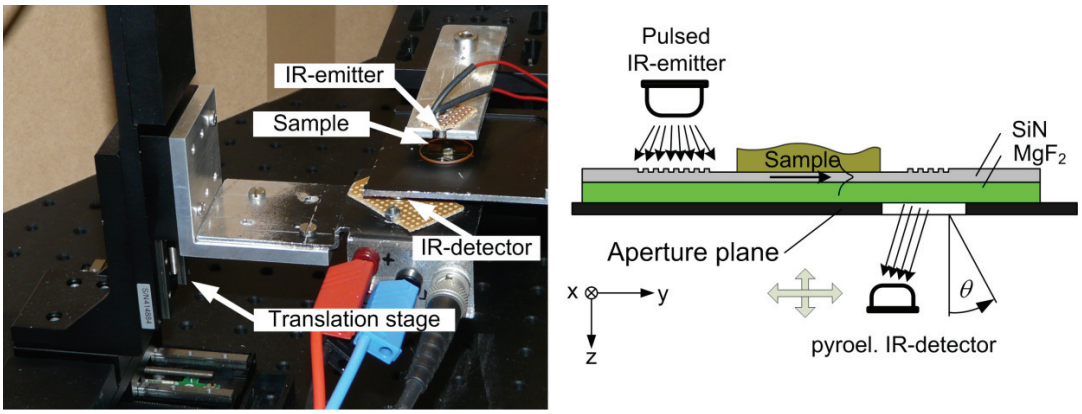

Fig. 3: Measurement setup including a motorized translation stage to investigate the spectral separation. The IR-emitter is positioned at the opposite side of the waveguide because this configuration makes the positioning easier. In a final setup both the emitter and the detector could be placed on the same side of the waveguide element.

Even though the aging can be clearly distinguished from the normalized transmission measurements of the differently aged oils, shown in Fig. 4, it is apparent that this prototype setup is not optimized regarding the noise behavior. Already a simple housing of the entire setup or the utilization of an IR-detector array, which would enable a simultaneous measurement of the considered coupling angles, would improve the signal to noise ration significantly. Even though the spectroscopic measurement, obtained by means of the dispersive features of a grating coupler, could be realized with an IR detector array, we have carried out our experiment with a mechanically positioned single element thermal detector in order to reduce the technical complexity.

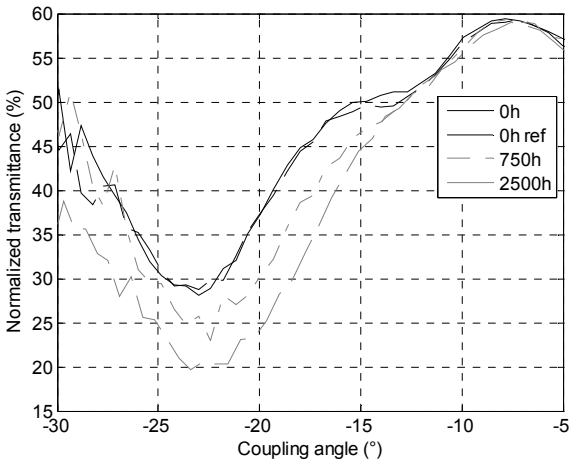

Fig. 4: Normalized (oil to reference measurements) transmission of different artificially aged oils versus coupling angle. The normalized transmission is shown twice (0 h and 0 h ref) in order to illustrate the degree of reproducibility.

Improved Sensor Performance

In the mid-IR-range the available power is limited, which results in high requirements with respect to the signal to noise ration. Since we utilize in the proposed fully integrated sensor thermal IR-detectors with less sensitivity than cryogenic cooled IR-detectors, we attempt to improve the sensitivity by means of exploiting the features of photonic structures, as shown in Fig. 5.

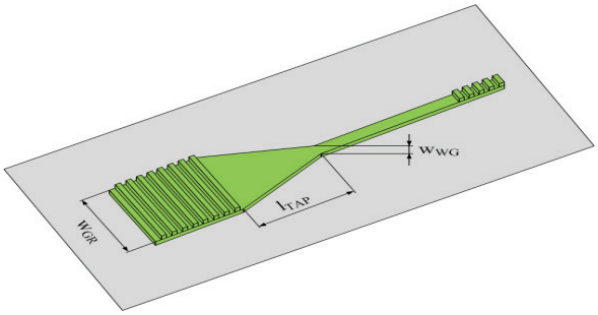

Fig. 5: Sketch of an integrated taper structure of a SiN-waveguide on an MgF_2 substrate. The insertion of the taper structure features an improved energy density resulting in a better signal to noise ratio.

A thermal IR-source simply represents a heated body emitting IR-radiation described by Planck's law. In case of a thermal emitter the power emitted by the surface is proportional to the surface area and the temperature. Thus, increasing the width (coupling area) of a grating coupler increases the energy coupled into the waveguide but not the energy density. A taper structure on the other hand increases the energy density (see Fig. 6) but not the total guided energy. In consequence, introducing a taper structure, as shown in Fig. 5, enables the implementation of a wide grating coupler – yielding high energy in a wide waveguide – in conjunction with a small waveguide guiding the IR radiation. This configuration can be utilized in combination with a small IR detector (array) obeying less noise than larger detectors.

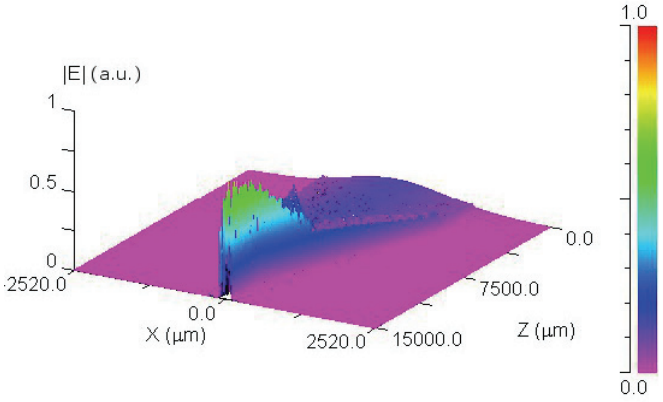

Fig. 6: Numerical simulation of the taper structure using the beam propagation method (BPM, RSoft). The calculations have been carried out in cooperation with the Center for Surface- and Nanoanalytics, Johannes Kepler University Linz.

Spectral Resolution

Even though the requirements regarding the spectral resolution are very low for the considered application regarding oil aging, it is of general interest to find out what spectral resolution can be achieved with the proposed sensor setup. Thus, in contrast to our previous work dealing with the sensor principle, we considered in [24] the achievable spectral resolution of the proposed concept, which represents a major requirement for further work. Using grating couplers, broadband IR-radiation can be coupled into and out of the waveguide, where the coupling angle determines the wavelength of the coupled radiation. Thus the couplers also facilitate separation of the prescribed wavelength. Besides the coupling efficiency of thermal radiation of the utilized grating couplers [22], the design of the mono-mode slab waveguide also affects the performance of the entire sensor system with respect to the signal to noise ratio (SNR) of the detected IR-radiation. However, considering the achievable spectral resolution requires a special consideration on the design of the grating coupler, which couples the IR-beam towards the IR-detector featuring the spectral separation. In order to confirm the numerical results obtained in [24], we also have carried out measurements by means of an experimental setup utilizing a single element detector and a simple 3 dimensional mechanical positioning setup.

Conclusion

Vibrational spectroscopy is a powerful method in characterizing chemical substances regarding their quantitative and qualitative composition. However, the application of vibrational spectroscopy in the different fields from process monitoring to lab applications requires a sophisticated interface between the IR radiation and the sample under investigation. Especially the emerging microsystems technology shows features beating the conventional measurement equipment. The investigations carried out so far, have shown promising theoretical and experimental result. However, there is still a lot of work to do in order to understand and exploit the full potential of photonic structures in vibrational spectroscopy.

Acknowledgment

This work has been supported by the European Regional Development Fund (EFRE) in the framework of the EU program Regio 13, the Austrian research funding association (FFG) under the scope of the COMET program within the research network “Process Analytical Chemistry (PAC)” and the federal state Upper Austria. The preliminary studies have been carried out at Integrated Microsystems Austria GmbH within the PhD study of the author at the Institute for Microelectronics and Microsensors, Johannes Kepler University Linz.

I would like to thank Ahmad Saeed (Center for Surface- and Nanoanalytics, Johannes Kepler University Linz) and Thomas Fromherz (Institute of Semiconductor and Solid State Physics, Johannes Kepler University Linz) and their colleagues for supporting the work related to microsystems technology. The fruitful cooperation and the thus facilitated access to the clean room facilities at the physics department enabled the sophisticated research in the field of microsystems technology.

References

[1] L. Küpper, J.V. Gulmine, P.R. Janissek, H.M. Heise, Attenuated total reflection infrared spectroscopy for micro-domain analysis of polyethylene samples after accelerated ageing within weathering chambers, Vib. Spectrosc. 43 (2004), pp.63-72.

[2] P. B. Tarsa, P. Rabionwitz, K.K. Lehmann, Evanescent field absorption in a passive optical fiber resonator using continuous-wave cavity ring-down spectroscopy, Chem. Phys. Letters 383 (2004), pp.297-303.

[3] B. Mizaikoff, K. Taga, R. Keller, Infrared fiber optic gas sensor for chlorofluorohydrocarbons, Vib. Spectrosc. 8 (1995), pp.103-108.

[4] M. Ahmad, Larry L. Hench, Effect of taper geometries and launch angle on evanescent wave penetration depth in optical fibers, Biosens. Bioelectron. 20 (2005), pp. 1312-1319.

[5] J. Keirsse, C. Boussard-Pl´edela, O. Lor´ealb, O. Sirec, B. Bureaua, P. Leroyerb, B. Turlinb, J. Lucasa, IR optical fiber sensor for biomedical applications, Vib. Spectrosc. 32 (2003),pp.23-32.

[6] G. Pandraud, T.M. Koster, C. Gui, M. Dijkstra, A. van den Berg, P.V. Lambeck, Evanescent wave sensing: new features for detection in small volumes, Sensor Actuators A 85 (2000), pp.158-162.

[7] M. Ishifuji, T. Suzuki, M. Mitsuishi, T. Miyashita, Molecular orientation of nonlinear optical polymer nanosheets on silica nanoparticle monolayer studied by optical waveguide spectroscopy, Thin Solid Films 518 (2009), pp.457-461.

[8] B. Mizaikoff, Mid-infrared evanescent wave sensors - a novel approach for subsea monitoring, Meas. Sci. Technol. 10 (1999), pp.1185-1194.

[9] G. Pandraud, P.J. French, P.M. Sarro, Fabrication and characteristics of a PECVD SiC evanescent wave optical sensor, Sens. Actuators A 142 (2008), pp.61-66.

[10] M. Zourob, S. Mohr, B.J. Treves Brown, P.R. Fielden, M. McDonnell, N.J. Goddard, The development of a metal clad leaky waveguide sensor for the detection of particles, Sens. Actuators B 90 (2003), pp.296-307.

[11] Ch. Charlton, A. Katzir, B. Mizaikoff, Infrared Evanescent Field Sensing with Quantum Cascade Lasers and Planar Silver Halide Waveguides, Anal. Chem. 77 (2005), pp.4398-4403.

[12] L. Hvozdara, N. Pennington, M. Kraft, M. Karlowatz, B. Mizaikoff, Quantum cascade lasers for mid-infrared spectroscopy, Vib. Spectrosc. 30 (2005), pp.53-58.

[13] Ch. Charlton, M. Giovannini, J. Faist, B. Mizaikoff, Fabrication and Characterization of Molecular Beam Epitaxy Grown Thin-Film GaAs Waveguides for Mid-Infrared evanescent Field Chemical Sensing, Anal. Chem. 78 (2006), pp.4224-4227.

[14] R. F. Wolffenbuttel, State-of-the-Art in Integrated Optical Microspectrometers, IEEE Trans. on Instr. and Meas. 53 (2004), pp. 197-202.

[15] R. Siebert, J. Müller, Infrared integrated optical evanescent field sensor for gas analysis Part I: System design, Sens. Actuators B 119 (2005), pp.137-148.

[16] G. de Graaf, W. der Vlist, R.F. Wolffenbuttel, Design and fabrication steps for a MEMS-based infrared spectrometer using evanescent wave sensing, Sens. Actuators A 142 (2008), pp. 211-216.

[17] C. Maims, J. Hulme, P.R. Fielden, N.J. Goddard, Grating coupled leaky waveguide mirco channel sensor chips for optical analysis, Sens. and Actuators B 77 (2001), pp. 971-978.

[18] W.A. Challener, J.D. Edwards, R.W. McGowan, J. Skorjanec, Z. Yang, A multilayer grating-based evanescent wave sensing technique, Sens. and Actuators B 71 (2000), pp.42-46.

[19] A. Agoston, C. Ötsch, J. Zhuravleva, B. Jakoby, An IR-Absorption Sensor System for the Determination of Engine, Proceedings IEEE Sensor 2004, pp.463-466.

[20] J. Kasberger, P. Rauter, T. Fromherz, B. Jakoby, A Slab Waveguide Sensor For a Fully Integrated IR-Absorption Sensor System – Theoretical and Experimental Verification, Proc. Transducers (2009), pp.999-1002.

[21] J. Kasberger, B. Jakoby, Design of a Novel Fully Integrated IR-Absorption Sensor System, Proc. IEEE Sensors (2007), pp.515-518.

[22] J. Kasberger, B. Jakoby, Grating-Coupling of Thermal Radiation as an Essential Element of a Fully Integrated.

[23] J. Kasberger, T. Fromherz, A. Saeed, B. Jakoby, Miniaturized Integrated Evanescent Field IR-Absorption Sensor: Design and Experimental Verification with Deteriorated Lubrication Oil, Vib.Spectrosc. (2011), doi:10.1016/j.vibspec.2011.01.003.

[24] J. Kasberger, A. Saeed, T. Fromherz, S. Katletz, B. Jakoby, Spectral Resolution of the Grating-Coupler of a Miniaturized Integrated Evanescent Field IR-Absorption Sensor, J. Quantum Electronics, accepted, 2011.

LAB-ON-A-CHIP: Applications to Cell Biology

Peter Ertl

Department of Health & Environment/ Nano Systems
AIT Austrian Institute of Technology, Vienna, Austria

Cell cultures and cell-based assays are an essential tool for drug discovery, tissue engineering and stem cell research. Although studying cell cultures has become an essential tool in cell and molecular biology, medicine and biotechnology, it has fallen far behind in the pace of progress as demonstrated by genome sequencing, imaging probes, and high-throughput testing of biochemicals. One major drawback of employing conventional cell cultures is that they do not consider adequate nutrient supply, fluid mechanical shear forces, waste removal, and constant temperature. It is well known that cell responses are profoundly influenced by the cellular microenvironment or biological niche. Additionally using classical cell-based assays, particularly in combination with prevailing screening technologies, employ immortalized cell lines exhibiting phenotypes that differ significantly from those found in human pathology. Consequently, to gain a deeper biological understanding of the complex cellular interactions with their microenvironment, it is necessary to first make progress in experimental devices and analytical methods.

Microfabrication technology has shown potential for providing the next generation of cell analysis tools where large numbers of single cells or small numbers of cell populations can be tested in a cellular environment that better mimics *in vivo* situations. Microfluidic biochips or lab-on-a-chip systems are vital for cell analysis because they allow spatial and temporal control of growth conditions. An important aspect in cell analysis also relates to the ability to investigate dynamic cell responses to changing external parameters. Consequently, to advance cell based *in vitro* methodologies we have developed lab-on-a-chip systems capable of monitoring cellular dynamics continuously and non-invasively in a nanoliter environment under near-native conditions. The Cell-on-Chip system comprises of external pumping and heating stations, valves, injection ports and the microfluidic biochip containing embedded optical and electrical microsensors. The presented work addresses aspects of chip design and sensor characterization as well as their applications to cell biology including nanotoxicology, tumor invasion studies and personalized medicine. The presented technology could, therefore, provide medicine with a diagnostic tool exhibiting better sensitivity, specificity and reliability.

Nanostructures and Nanotechnology

Semiconductor Device Modeling: The Last 30 Years

Hans Kosina

Institute for Microelectronics, TU Vienna, Vienna, Austria

Numerical simulation of semiconductor devices has evolved to a wide and viable research field over more than three decades. The various subjects considered reflect the tremendous progress in semiconductor technology. The term Technology CAD (TCAD) has been coined to describe classical device simulation, which is based on continuum theory and classical transport theory. By solving the continuity equations for electrons and holes self-consistently with the Poisson equation for the electrostatic potential, the operation of various unipolar and bipolar devices can be well understood, both qualitatively and quantitatively [1]. The main drivers for TCAD tool development were silicon integrated circuit technology and silicon power devices. According to the scaling rules of CMOS technology, the doping levels and the electric field strengths in the junctions were continuously increased, which eventually resulted in reliability problems due to hot carriers. To study hot carrier effects theoretically, end of the 1980s Monte Carlo simulation including a numerically tabulated electronic band structure has been introduced. The Monte Carlo method solves the classical Boltzmann equation for the charge carriers and is often considered a reference method for the simpler transport models used in TCAD. The continuous reduction of the supply voltage below three Volts, however, alleviated the hot carrier problem significantly. With the advent of strain engineering in the 1990s the electronic band structure was intentionally distorted by imposing appropriate strain conditions. Full-band Monte Carlo calculations helped to quantify the effect of the band structure changes on the electronic transport properties. For the classical TCAD tools new mobility models have been developed taking the strain dependence into account. With continued down-scaling of the oxide thickness the classical TCAD tools needed to be augmented by quantum correction models which approximate the quantum mechanical charge distribution in the channel. Besides silicon main stream technology, a variety of new semiconductor nano-structures and nano-devices came into the focus of device simulation, but also a variety of new materials. Examples are carbon nano-tubes, graphene, and organic semiconductors, to name a few. Device modeling has entered the field of mesoscopic physics, where quantum mechanical effects such as confinement, tunneling, interference and charging effects determine the characteristics of a device [2]. This extended field of research is commonly referred to as Computational Electronics [3]. Mesoscopic physics still uses concepts from continuum theory, such as band structure, band diagrams, and envelope functions which are wave functions where the lattice-periodic part has been factored out. At the small end of mesoscopic structures the tight-binding method is often used, which is an empirical atomistic method for electronic structure calculation. Specific problems need to be considered on an atomistic level and require so-called *ab initio* methods. An example is the degradation of gate insulators, where *ab initio* calculations give insight into the type of field-induced defects and their kinetics. Another important subject of device modeling deals with electrical devices coupled to some non-electric system, as it is the case for optoelectronic devices, including various types of semiconductor lasers, or thermoelectric devices, but also MEMS and sensor devices for various applications. In summary, it can be concluded that device modeling has evolved to a

wide multidisciplinary field. Numerical mathematics, computer science, and various fields from physics such as solid state physics, quantum mechanics, and statistical mechanics, are closely interlinked. Today, Computational Electronics provides a multitude of approaches and tools to cope with the ever increasing number of new semiconductor devices and structures, and the new materials being introduced.

References

[1] S. Selberherr, Analysis and Simulation of Semiconductor Devices, Springer 1984.

[2] S. Datta, Quantum Transport: Atom to Transistor, Cambridge University Press 2005.

[3] D. Vasileska, S. Goodnick, G. Klimeck, Computational Electronics, CRC Press 2010.

MBE Growth of III-V Nanowires and Related Heterostructures – Application to Photovoltaics

Anna Fontcuberta i Morral

Ecole Polytechnique Fédérale de Lausanne (EPFL), Switzerland

Nanowires are filamentary crystals with a diameter of few to a hundred of nanometers. Thanks to their dimensions they are the perfect playground for fundamental studies and for improving devices such as solar cells. Nanowires are typically obtained by the vapor-liquid-solid method in which a metal catalyst is used for the gathering of the precursor species and nanowire growth. In most of the cases gold is used, though it has been shown to affect negatively the electronic and optical properties of semiconductors. We obtain ultra-high purity GaAs nanowires by avoiding the use of gold and by the use of molecular beam epitaxy (MBE). MBE offers also the unique possibility of combining an extremely high purity of materials with the possibility of growing with epitaxial quality on the nanowire facets. Prismatic quantum wells and Stranski-Krastanov quantum dots are obtained with a very high quality, as demonstrated by the optical spectroscopy measurements. Finally, we discuss how these nanowires are excellent candidates for the fabrication of solar cells and high mobility transistors by using a modulation doped structure.

Next Generation of Quantum Dot Devices Based on Tailored Nanostructured Materials

Johann Peter Reithmaier

Technische Physik, Institute of Nanostructure Technologies and Analytics (INA), University of Kassel, 34132 Kassel, Germany

By nano-structuring of semiconductors, the macroscopic material properties can be directly controlled by the geometric dimensions of the nano-objects rather than by the chemical composition. However, by using the most commonly applied Stranski-Krastanov growth mode the control of the quantum dot geometry in most cases is suffering by size fluctuations and the statistical distribution of nucleation sites.

This presentation gives an overview about our recent work on developing improved and new growth processes for quantum dot materials, exhibiting an enhanced degree of freedom for tailoring the material properties for specific optoelectronic device applications.

Improvements obtained in quantum dot growth techniques will be discussed in different quantum dot material systems (GaAs and InP based) and by using different growth techniques, like Stranski-Krastanov growth mode, droplet epitaxy and growth on pre-patterned surfaces. Device examples will be given, where this new generation of quantum dot material is used to tailor specific devices properties. This includes, e.g., 920 nm cooler-less high power pump modules based on quantum dot laser arrays with internal temperature compensation, 1060 nm high brightness single mode lasers for frequency doubling based on a tunneling injection design, and new generation of high-gain InP quantum dot material for high-speed lasers and optical amplifiers.

Finally, an outlook will be given on the potential of tailored quantum dot material to realize ultra-fast optoelectronic devices approaching the THz frequency regime.

Mid-Infrared Active Quantum Dots

Gunther Springholz

Institute of Semiconductor Physics, University of Linz, Austria

In spite of extensive research, mid-infrared emission from self-assembled semiconductor quantum dots produced by the usual heteroepitaxial Stranski-Krastnow growth has remained elusive due to the unfavorable type II band alignments of most narrow band gap material systems. In this talk, I will present an alternative synthesis approach, based on epitaxial PbTe quantum dots (QDs) embedded in a wide band gap CdTe matrix. These materials are practically strain free due to the almost perfect lattice matching but exhibit a huge quantum confinement due to the very large 1.2 eV difference in the band gaps. Our synthesis approach is based on phase separation rather than on lattice-mismatch strain and is driven by the large miscibility gap between IV-VI and II-VI materials due to the difference in lattice structure. As a result, in epitaxial structures phase separation occurs at elevated temperatures, resulting in the formation of well isolated, nearly spherically and wetting-layer free PbTe quantum dots with atomically abrupt interfaces. The quantum dots exhibit intense mid-infrared emission even at room temperature and the dot size can be varied over a wide range by changing the deposited layer thickness or composition or by variation of the growth temperature. Due to the large quantum confinement, mid-infrared emission can be tuned over the whole 1.5 – 4 μm wavelength region. Application of these quantum dots in the form of MID LEDs and microdisk lasers is demonstrated, where the latter represent the first quantum dot lasers emitting at wavelengths longer than 1.6 μm. Potential applications of such devices are in molecular gas analysis, environmental monitoring and medical diagnostics.

Photonics and Optoelectronics

Narrow Photoluminescence Emission of Ge Islands Grown on Pit-Patterned Si(001) Substrates at Various Temperatures

F. Hackl, M. Grydlik , M. Brehm, H. Groiss, F. Schäffler, T. Fromherz and G. Bauer

Institut für Halbleiter- und Festkörperphysik, Universität Linz, 4040 Linz, Austria

The advantages of Ge islands grown on pre-patterned Si(001) substrates as compared to randomly nucleated ones are the control over the nucleation sites as well as the island's homogeneous composition distribution. In this work we investigate the dependence of the island morphology and homogeneity on the substrate pattern period. By photoluminescence experiments the influence of the statistical size distribution on the optoelectronic properties of an island ensemble is monitored.

Ge islands were grown by molecular beam epitaxy at different temperatures (650 °C, 690 °C, 725 °C and 760 °C) on substrates pit-patterned by e-beam lithography with various pit periods p from 300 nm to 900 nm. Low Si capping temperature (300 °C) was used to preserve the island shape, size and Ge composition. Uncapped samples were grown for atomic force microscopy investigation.

We determine from the uncapped samples a clear correlation between the deposited amount of Ge per pattern unit cell with the size distribution and the morphological shapes of the islands. For the optimal amount, we observe significantly narrowed island photoluminescence emission peaks that are ascribed to the improvement of the Ge distribution homogeneity in the islands rather than to their shape homogeneity [1].

Beyond this optimal amount, dislocated superdomes are formed (see Fig.1 (c)). As a consequence, the island PL becomes almost completely quenched for these samples.

These findings emphasize the importance of accurate control over a parameter space including the deposition rate, the amount of deposited material, the pit period and the growth temperature of heteroepitaxial island growth on pre-defined positions.

References

[1] F. Hackl, M. Grydlik, M. Brehm, H. Groiss, F. Schäffler, T. Fromherz, and G. Bauer, Nanotechnology **22** (2011) 165302

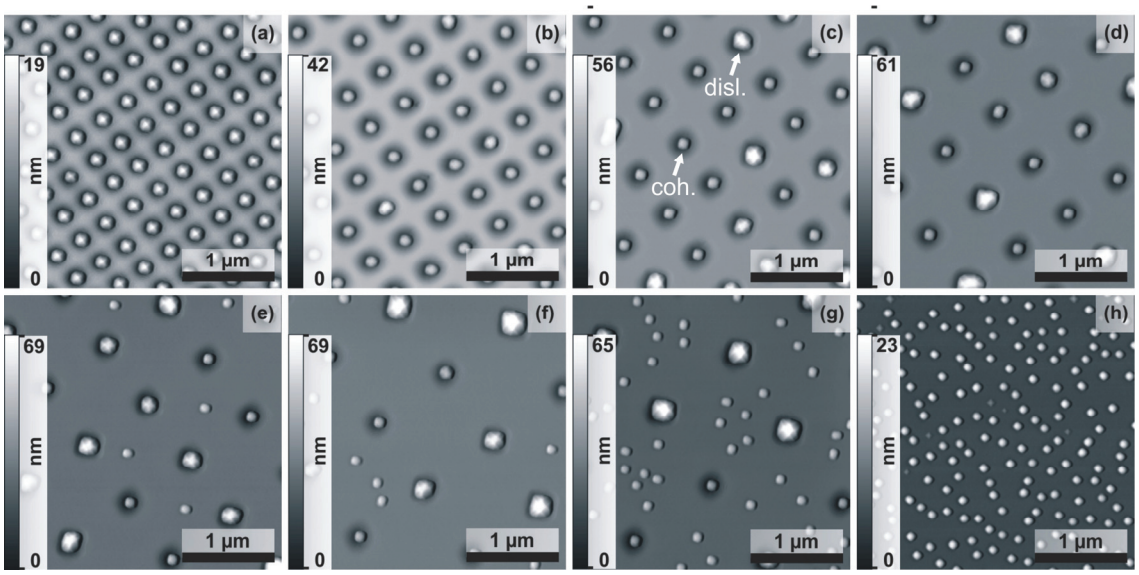

Fig. 1: AFM micrographs in height mode showing Ge islands grown at 690°C and at a rate of 0.05 Å/s on pit-patterned Si substrates with periods of 300 nm (a) to 900 nm (g). (h) islands grown on planar Si(001) substrate. In (c) dislocated super-domes, labeled “disl.” and coherent islands labeled “coh.” are indicated.

Mid-Infrared Quantum Dot LEDs and Microdisk Laser Grown by MBE

A. Hochreiner[1], M. Eibelhuber[1], T. Schwarzl[1], H. Groiss[1], V. Kolkovsky[2], G. Karczewski[2], T. Wojtowicz[2], W. Heiss[1], G. Springholz[1]

[1]Institute of Semiconductor Physics, Johannes Kepler University, 4040 Linz, Austria
[2]Polish Academy of Sciences, 02668 Warszawa, Poland

In spite of extensive research, mid-infrared (MIR) emission from self-assembled Stranski-Krastanow quantum dots (QDs) has remained difficult due to the unfavorable band alignments of the most narrow band gap semiconductor material systems. For the realization of quantum dots with strong infrared emission, we have therefore developed an alternative strain-free synthesis method in which dot formation is induced by phase separation rather than by heteroepitaxial strain. The resulting QDs exhibit almost spherical shapes with abrupt interfaces, are essentially defect- and strain-free and show intense mid-infrared photoluminescence (PL) even at room temperature [1].

In this work, we show for the first time mid-infrared light emitting diodes (LEDs) operating in cw up to room temperature and we demonstrate cw optically pumped lasing up to 200 K in microdisk structures based on these unique PbTe QDs.

The samples were grown by molecular beam epitaxy on high quality CdTe buffer layers predeposited on GaAs (001) substrates and the PbTe dots are formed by nanoprecipitation from thin 2D layers embedded in CdTe. The emission wavelength of the dots can be tuned either by changing the PbTe layer thickness [1] or by varying the growth temperature of the PbTe layer. The dot emission wavelength for an initially 1 nm thick PbTe layer grown at different temperatures ranges from 2.1 µm to 2.7 µm. This corresponds to a change of the diameter of the nearly spherical dots from 8 nm to 14 nm. An even more pronounced change of the emission wavelength can be achieved by changing the PbTe layer thickness. A variation of the layer thickness from 0.3 nm to 80 nm results in the tuning of the dot emission from 1.4 µm to 4 µm with dot diameters ranging from 5 nm to 30 nm.

For LED emission, p-i-n structures were fabricated, where the active PbTe dot layer is embedded in the center of a 0.5 µm thick CdTe intrinsic region. Cw electroluminesensce (EL) spectra were measured at various temperatures up to 300 K for dots with average diameters of 10 and 12 nm, respectively. The LED emission was compared to PL spectra from the same sample region using a 1064 nm laser with photon energy well below the CdTe band gap. At all temperatures from 30 K to 300 K the EL exactly matches the PL for both samples proving that the EL indeed arises from the embedded PbTe QDs. At 300 K the total output power was found to be 0.7 µW at 8 mA diode current [2].

To obtain lasing from the PbTe QDs, microdisks with a diameter of 40 µm were fabricated by photolithography and wet chemical etching. The single active PbTe dot layer is positioned in the center of the 2 µm thick CdTe waveguide. The QD microdisks were optically excited in cw below the CdTe band gap at a wavelength of 1030 nm, resulting in laser emission up to temperatures as high as 200 K with a maximum output power at

50 K of 0.15 mW considering homogenous emission. Thus, our unique PbTe QDs proof their suitability for novel mid-infrared optoelectronic devices.

References

[1] W. Heiss, et al., Appl. Phys. Lett. 88, 192109 (2006); H. Groiss, et al., Appl. Phys. Lett. 91, 222106 (2007).

[2] A. Hochreiner, et al., Appl. Phys. Lett. 98, 021106 (2011).

Coupling Strategies for Coherent Operation of Ring Cavity Surface Emitting Intersubband Lasers

C. Schwarzer[1], E. Mujagić[1], M. Nobile[1], H. Detz[1], S. Ahn[1], W. Schrenk[1], J. Chen[2,3], C. Gmachl[2] and G. Strasser[1,4]

[1]Institute for Solid State Electronics, Vienna University of Technology, 1040 Vienna, Austria
[2]Department of Electrical Engineering, Princeton University, Princeton, NJ 08544, USA
[3]Shanghai Institute of Technical Physics, Chinese Academy of Science, Shanghai, China
[4]Departments of Electrical Engineering and Physics, SUNY at Buffalo, NY 14260, USA

Since quantum cascade lasers (QCLs) [1] represent compact reliable coherently emitting devices in the mid infrared (MIR) and terahertz (THz) spectral region, investigations with respect to their material system and especially their resonator design are highly appreciated. The fact that their emission spectrum is rich in molecular absorption lines opens a wide field of real world applications including gas analysis for environmental and medical uses as well as chemical sensing. Since several tasks call for high optical output power, considerations in this direction become essential. Here, we report fundamental investigations on the capability of coherent operation of an arbitrary number of QCL devices. The gained results open up numerous future prospects for coupled QCLs, up to two dimensional QCL arrays for powerful, monochromatic emission at room temperature. Recently, our group presented an ideal elementary building block for two-dimensional laser arrays, the ring cavity surface emitting lasers (RING-CSELs) [2]. This resonator type provides the feasibility of producing symmetric low divergence optical beams combined with single-mode operation, reduced thresholds and enhanced radiation efficiency. It incorporates a ring shaped resonator, holding a second order distributed feedback (DFB) grating on top that acts as a Bragg reflector for surface light extraction. Its comparable large emission area in combination with an absence of facets make RING-CSELs show considerably enhanced properties in comparison to conventional edge emitting Fabry-Perot lasers. The present investigations on coherent coupling are executed using high performance RING-CSELs based on a InGaAs/InAlAs/InP material system with 8.05 µm nominal emission wavelength, as recently published by our group [3 and references therein].

Coherent coupling plays an important role since it results in a significant enhancement of the spatial and spectral brightness. This application promises not only power enhancement under retention of coherence, coupled devices with different resonators can achieve remarkably increased overall mode selectivity by exploiting the Vernier effect. Different approaches showed optimal coupling for a coupling- gap of 1 µm. At this geometry, where two separated lasers couple via their evanescent field, a balanced relation between intercavity losses and sufficient coupling strength for robust coherence was achieved [4]. Furthermore, a geometry of directly coupled resonators is presented

that features single mode emission at room temperature. These coherently coupled device pairs exhibit an interference far field pattern.

References

[1] J. Faist *et al.*, Science 264, 553-556 (1994).

[2] E. Mujagić *et al.*, Appl. Phys. Lett. 93, 161101 (2008).

[3] E. Mujagić *et al.*, Appl. Phys. Lett. 96, 031111 (2010).

[4] C. Schwarzer *et al.*, Appl. Phys. Lett. 97, 071103 (2010).

Investigation of Double Metal THz Quantum Cascade Lasers by Terahertz Time-Domain Spectroscopy

M. Martl, D. Dietze, J. Darmo, C. Deutsch, A. Benz, M. Brandstetter, K. Unterrainer, P. Klang, A.M. Andrews, W. Schrenk, G. Strasser and E. Gornik

Vienna University of Technology, 1040 Vienna, Austria

The study of terahertz quantum cascade lasers (THz QCL) employing a single plasmon waveguide by broadband Terahertz pulses has gained a lot of physical insight [1]. In comparison to the single plasmon waveguide the double plasmon or metal-metal waveguide QCL uses a metal/semiconductor/metal structure. The generation of broadband THz radiation at the facet of a gallium arsenide filled waveguide was reported [2] recently.

We fabricated THz-QCLs in a geometry that allows the generation of broadband THz pulses in the first section of the waveguide and lasing operation within the second section. The THz transient generation on the QCL facet was investigated first. Further the coupling of the broadband THz pulses to the active QCL ridge was studied in experiment and by finite element simulation. The cavity of the emitter section and QCL section were proved to be coupled by FTIR measurements.

The coupled cavity configuration enabled the bias dependent measurement of gain and loss of the THz QCL [3]. The gain and loss processes can be explained by comparison with the calculated bandstructure.

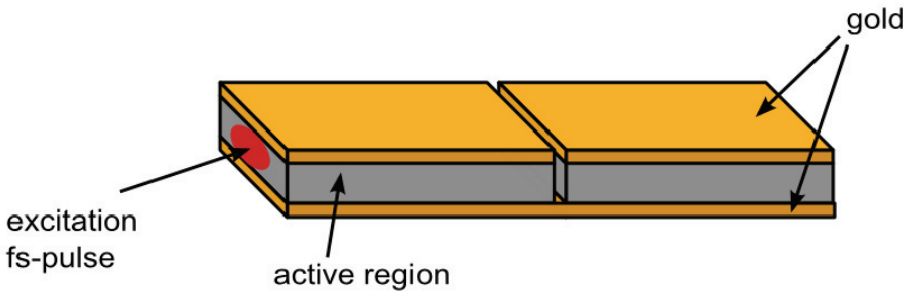

Fig. 1: Geometry used for coupling of broadband THz pulses into a double-metal.

References

[1] J. Kröll, J. Darmo, S. Dhillon, X. Marcadet, M. Calligaro, C. Sirtori, and K. Unterrainer, “Phase-resolved measurements of stimulated emission in a laser,” Nature **449**, 698 (2007).

[2] M. Martl, J. Darmo, K. Unterrainer, and E. Gornik, “Terahertz Waveguide Emitter with Sub-wavelength Confinement,” J. Appl. Phys. **107**, 013110 (2010).

[3] M. Martl, J. Darmo, C. Deutsch, M. Brandstetter, A. M. Andrews, P. Klang, G. Strasser, and K. Unterrainer, “Gain and losses in THz quantum cascade laser with metal-metal waveguide”, Opt. Express **19**, 733 (2011).

THz Quantum Cascade Lasers with Superconducting Double-Metal Waveguides

M. Brandstetter[1], A. Benz[1], C. Deutsch[1], K. Unterrainer[1], P. Klang[2], H. Detz[2], W. Schrenk[2], A.M. Andrews[2] and G. Strasser[2]

[1]Photonics Institute and Center for Micro- and Nanostructures, Vienna University of Technology, 1040 Vienna, Austria
[2]Institute of Solid-State Electronics and Center for Micro- and Nanostructures, Vienna University of Technology, 1040 Vienna, Austria

Quantum cascade lasers (QCLs) are promising sources for future applications in the terahertz (THz) regime like spectroscopy or imaging. The waveguide is crucial for the performance of the device. Double-metal waveguides are commonly used, where the active region is located in between two metal layers confining the optical mode. The waveguide loss is a limiting factor and needs to be minimized. The main contribution is the absorption of the THz radiation in the metal layers, Drude absorption. We replaced the commonly used gold layers by a superconducting material, namely niobium (Nb), to reduce the waveguide losses. We used a 4 well longitudinal optical (LO) phonon depletion design for the active region, with a designed frequency of 2 THz. We fabricated disk shaped resonators, where the optical mode is guided via total internal reflection at the facets of the disk. In this way high lateral confinement is provided. A sketch of a device is shown in Fig. 1. The next steps would be to employ an active region with lower frequency and a superconducting material with higher critical temperature.

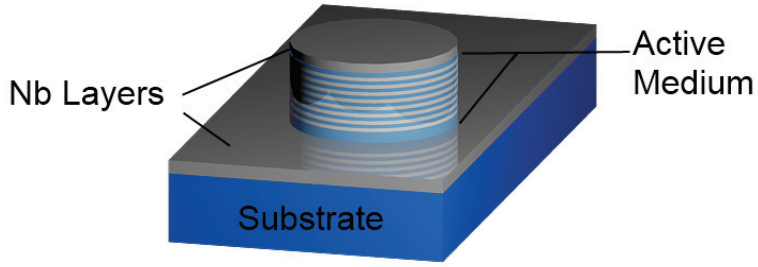

Fig. 1: Schematic of a THz QCL with a niobium disk resonator

THz Conductivity of Graphene

A. Urich, T. Mueller, J. Darmo and K. Unterrainer

Photonics Institute and Center for Micro- and Nanostructures, Vienna University of Technology, 1040 Vienna, Austria

Since its discovery [1] in 2004, graphene, a single layer of carbon atoms arranged in a honeycomb lattice, attracted enormous attention in many scientific fields. This is not only due to the fact that two-dimensional crystalline systems like graphene were supposed not to exist, but mainly due to the unique electronic properties and possible applications in nanoelectronics.

The crystal structure of graphene consists of two equivalent sublattices. Interaction of electrons between these sublattices leads to the formation of two energy bands that intersect at the points K and K' in k-space. In contrast to conventional metals and semiconductors, the electron dispersion relation is linear and gapless around these crossing points. Under certain conditions, this fact is expected to result into strong interaction between graphene and terahertz radiation and hence makes graphene a very interesting material for the terahertz spectral range.

We present an experimental approach to measure the optical conductivity of a graphene monolayer by means of THz time-domain-spectroscopy involving an on-chip coplanar waveguide structure for generation and detection of THz pulses. While the optical conductivity of graphene is constant in the visible spectral region, it is expected to show strong deviation from this behavior in the THz frequency region [2]. This is due to the fact that interband transitions dominate in the visible range, whereas below the mid-infrared range, intraband transitions are dominant.

References

[1] K. S. Novoselov et al., Science 306, 666 (2004)

[2] L. Falkovsky et al., Phys. Rev. B 76, 153410 (2007)

Development of Broadband, Polarization Insensitive Light Couplers for a SOI Based Integrated Optics

M. Humer, R. Guider, T. Fromherz, W. Jantsch

Institute of Semiconductor and Solid State Physics, Johannes Kepler University Linz, Austria

The growing demand for quickly transporting big amounts of data within and between Si integrated circuit chips will hit the limits set by data transfer rates achievable with *electrical* inter-connects in the near future. Intra- and inter-chip *optical* data transmission is regarded as one of the most promising future strategies for providing sufficiently fast data channels. Thus, large efforts are spent world-wide to the development of a Silicon On Insulator (SOI) based optoelectronic platform [1]. Besides the challenges faced in the development of efficient Si based light sources, detectors and fast modulators for integration, also reliable interfaces between optical fibers and chips are required.

In our work, we develop interfaces for efficiently coupling light from optical fibers into SOI based integrated optical circuits that are both interesting for research as well as for commercial applications. The emphasis is devoted to couplers with high efficiency over a broad wavelength region (from 1400 nm to 1600 nm) and for all directions of polarization. From thorough simulations, “inverted taper” structures (see Fig. 1 for a schematic) have been identified as most promising structures satisfying these demands while keeping the overall dimensions of the coupling device as small as possible. A detailed discussion of the working principle is presented that shows the matching the modes of the incident beam of light to the input of the coupler and then transforming the modes to fit the single SOI-waveguide mode at the end of the structure. We show that it is crucial to optimize the dimensions at the start and the end of the tapered waveguide according to “mode coupling” calculations for maximum coupling efficiency.

For the fabrication of our structure we use a combination of optical lithography and electron-beam lithography, exploiting the advantages of both techniques for optimal results. While optical lithography is used to quickly define waveguides over a wide working area, electron beam lithography allows to further alter and “fine-tune” the dimensions of the structures with a very high precision. Aside from this “mix and match” technique, which will also be used to define resonators, inter-chip couplers, feedback structures and devices for light amplification and detection with pinpoint accuracy, we also plan to further increase our range of possibilities for the fabrication of our samples by using nano-imprint technology.

References

[1] see for example L. Tsybeskov, D. J. Lockwood, M. Ichikawa, Proc. IEEE **97**, 1161 (2009) and references therein.

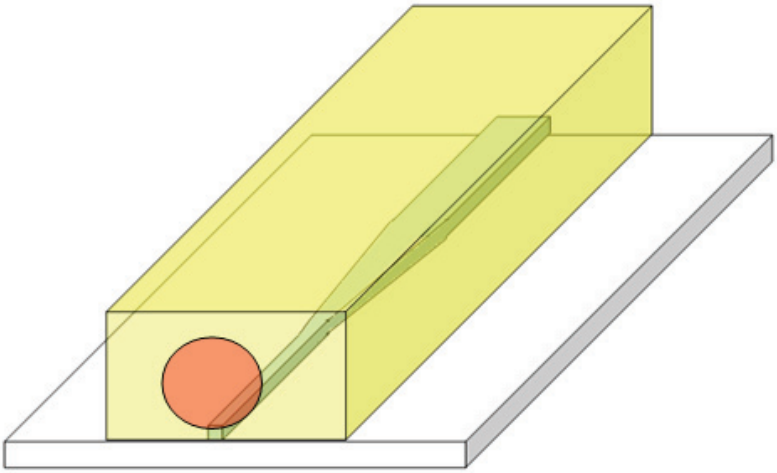

Fig. 1: Schematic of the proposed structure. Light from a lensed fiber is launched at the facet of an injection waveguide sitting on top of the “inverted taper”, which then transforms the light to fit the SOI waveguide mode at the end of the structure.

Resonant Absorption Enhancement in Photonic Crystal Slab Quantum Well Photodetectors

S. Kalchmair[1], R. Gansch[1], H. Detz[1], A.M. Andrews[1], P. Klang[1], W. Schrenk[1] and G. Strasser[1,2]

[1]Center for Micro- and Nanostructures, Vienna University of Technology, 1040 Vienna, Austria

[2]Department of Electrical Engineering and Department of Physics, The State University of New York at Buffalo, 332 Bonner Hall, Buffalo, NY 14260-1920, USA

Introduction

Photonic crystals (PCs) are structures with a periodic modulation of the refractive index, which exhibit fascinating properties for the control of light [1]. Most devices are fabricated as two-dimensional (2D) PC structures, as they are compatible to standard semiconductor processing. To confine the light in the out-of-plane direction the PC is often fabricated as a photonic crystal slab (PCS).

Here we present a photodetector, designed as a PCS for resonant absorption of infrared light and fabricated from a quantum well infrared photodetectors (QWIPs). Research on QWIPs has yielded reliable and sensitive detectors for the mid-infrared region [2]. However, the performance of QWIPs at higher temperatures is limited by thermally generated noise. By using a PCS for resonant in-coupling of the external radiation it is possible to exceed this limitation [3].

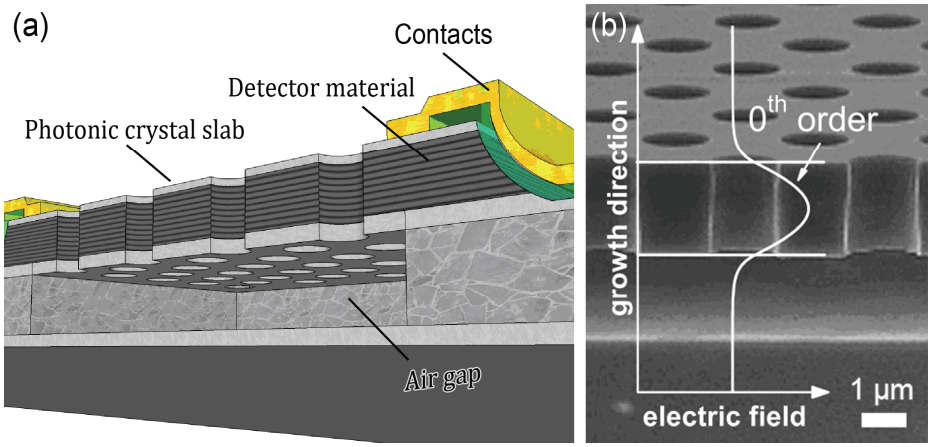

Fig. 1: PCS-QWIP design. (a) Cross section through the PCS-QWIP structure. (b) SEM image of the PCS, overlaid with the slab mode profile.

Experimental

The QWIPs are grown by molecular beam epitaxy and designed to operate at a wavelength of 8 µm. The detailed device structure can be found in [3]. From the QWIP material the PCS photodetectors and, for comparison, standard mesa photodetectors are fabricated. A schematic illustration of the finished device is shown in Fig. 1.

The processed PCS-QWIPs are illuminated at surface normal incidence. Standard QWIPs are measured at a 45° angle of illumination as they are insensitive to surface normal incidence light. The photocurrent spectrum of the standard QWIP has one broad absorption peak at 1250 cm^{-1} (Fig. 2, dashed line). Photons below this frequency do not have sufficient energy to excite electrons from the bound state into the continuum. For photons above this frequency an electronic transition becomes less probable, hence the absorption is reduced. The spectral response of the PCS-QWIP (Fig. 2, solid line) shows pronounced resonance peaks, which correspond to the photonic bands at the Γ-point [4].

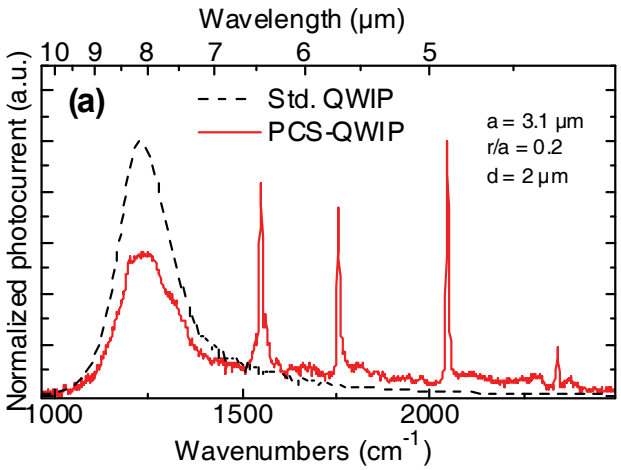

Fig. 2: Photocurrent response of a PCS-QWIP (solid line) and a standard QWIP (dashed line). The spectral response of the PCS-QWIP shows pronounced resonance peaks, which correspond to the photonic bands at the Γ-point.

Simulation

The optical properties of PCs are represented by the photonic band structure. To simulate the PCS band structure we use the 2D revised plane wave expansion method (RPWEM) [5], [6]. Compared to an ideal 2D-PC, which extends to infinity in the out-of-plane direction, the photonic bands in a PCS exhibit a blue-shift. The modes leak out of the slab into the surrounding air and “feel” a lower refractive index (Fig. 1 (b)). To model this effect an effective refractive index of a uniform slab is introduced and entered into the RPWEM algorithm as frequency dependent permittivity (Fig. 3 (a)). The equations describing the uniform slab wave guide can be solved analytically. To approximate the quantum well heterostructure an average refractive index of n_s = 3.12 is used. Figure 3 (b) shows a simulated photonic band structure of a PCS with lattice constant a = 3.1 µm, hole radius r/a = 0.2 and slab thickness d = 2 µm.

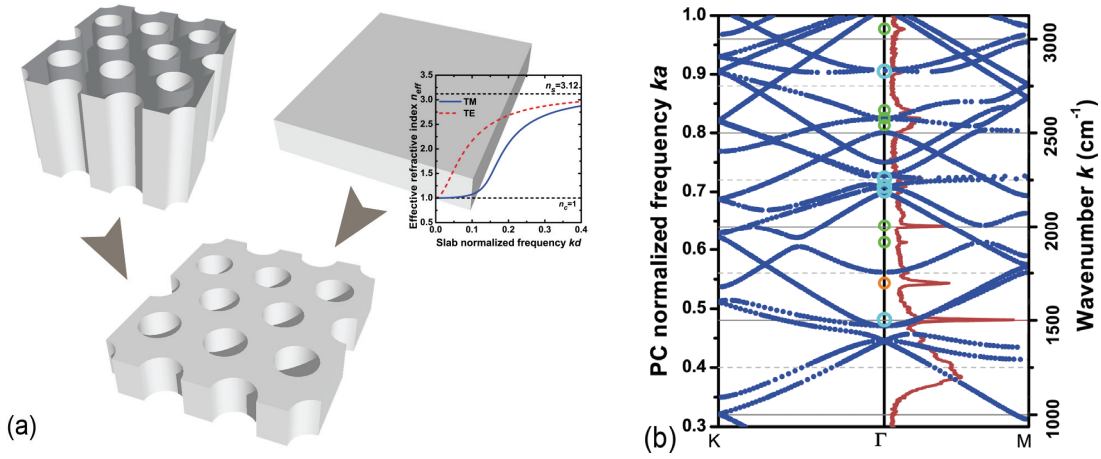

Fig. 3: RPWEM simulation of the PCS band structure. (a) The PCS is treated as a combination of a uniform slab wave guide and an ideal 2D-PC. (b) Comparison of the measured spectrum for surface normal incident light (Γ -Point) and the simulated band structure for TM-like modes. Blue circles indicate peaks that fit with the shown TM-like band structure. The orange circle fits in the not shown band structure for TE-like modes. Green circles correspond to higher order slab modes, as described in [6].

Results

The performance of standard QWIPs is usually limited by a thermally generated dark current, as it grows exponentially with temperature. In the PCS-QWIP the photocurrent is resonantly enhanced without creating additional dark current. The increased photon lifetime leads to absorption enhancement in the detector active region.

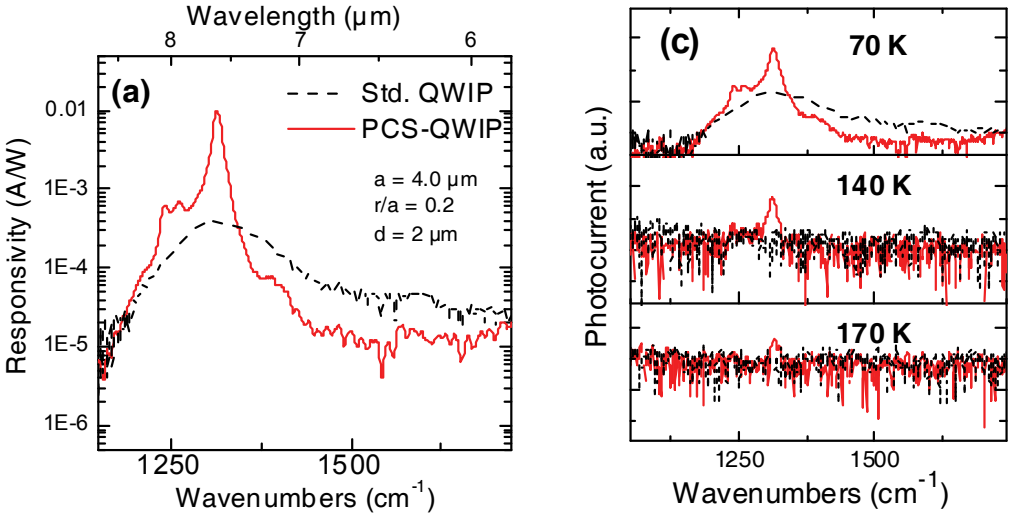

Fig. 4: Resonant absorption enhancement (a) The PCS is designed to have a resonance at the QWIP peak absorption. At the resonance frequency the responsivity is 24x larger compared to the standard QWIP. (c) Temperature dependent photocurrent spectra. At temperatures above 140 K, the standard QWIP signal disappears in the noise, while the PCS-QWIP signal is still visible.

Designing the PCS in a way that a strong resonance coincidences with the QWIP absorption peak results in a significantly higher responsivity and signal-to-noise ratio (Fig. 4 (a)). The standard QWIP signal vanishes in the noise around 140K while the PCS-QWIP resonance peak is still visible at 170K (Fig. 4 (c)).

Further, a standard QWIP is insensitive to surface normal incident light, caused by quantum mechanically forbidden electron transitions. With the PCS it is possible to achieve efficient coupling of surface normal incident light.

Conclusion

In conclusion, we presented a PCS photodetector, designed for resonant absorption of infrared light in quantum wells. The PCS photonic band structure was simulated with the 2D-RPWEM by using a slab effective refractive index. The PCS enhances the absorption efficiency by increasing photon lifetime in the detector active region. With this detector design, we were able to improve the responsivity up to 24x, compared to a standard quantum well photodetector.

Future research on this topic will include optimization of the PCS design to further increase resonant absorption enhancement. We envision that this approach will enable improved infrared photodetectors with superior detectivity compared to standard QWIPs, for applications including thermal imaging or high speed data transmission.

The authors acknowledge the support by the Austrian FWF project IRON, the PLATON project within the Austrian NANO Initiative and the “Gesellschaft für Mikro- und Nanoelektronik” GMe.

References

[1] Y. Kurosaka, S. Iwahashi, Y. Liang, K. Sakai, E. Miyai, W. Kunishi, D. Ohnishi and S. Noda, On-chip beam-steering photonic-crystal lasers, Nature Photonics **4**, 447-450 (2010)

[2] H. Schneider and H. C. Liu, Quantum Well Infrared Photodetectors, Berlin Heidelberg New York, Springer (2007).

[3] S. Kalchmair, H. Detz, G. D. Cole, A. M. Andrews, P. Klang, M. Nobile, R. Gansch, C. Ostermaier, W. Schrenk and G. Strasser, Photonic crystal slab quantum well infrared photodetector, Appl. Phys. Lett. **98**, 011105 (2011).

[4] S. Schartner, S. Golka, C. Pflügl, W. Schrenk, A. M. Andrews, T. Roch, and G. Strasser, Band structure mapping of photonic crystal intersubband detectors, Appl. Phys. Lett. **89**, 151107 (2006).

[5] S. Shi, C. Chen and D.W. Prather, Revised plane wave method for dispersive material and its application to band structure calculations of photonic crystal slabs, Appl. Phys. Lett., vol. **86**, p. 043104 (2005).

[6] R. Gansch, S. Kalchmair, H. Detz, A. M. Andrews, P. Klang, W. Schrenk, and G. Strasser, Direct measurement of higher order slab modes in Photonic Crystal Slab Quantum Well Infrared Photodetectors, submitted to Optic Express.

Nanostructures and Quantum Devices

Nanowires at Fke

A. Avdic, T. Burchhart, J. Greil, W. Molnar, F. Smecka, A. Lugstein and E. Bertagnolli

Institute of Solid State Electronics
Vienna University of Technology, 1040 Vienna, Austria

During the last 10 years, important progress has been made in the growth of ideal 1D structures, such as carbon nanotubes and semiconductor nanowires. These 1D systems promise to be an exciting field for basic and applied research. At sufficiently small sizes solids exhibit significantly different mechanical, optical, electrical and magnetic properties, when compared to bulk material of macroscopic size. Their low dimensionality means that they exhibit quantum confinement effects. For example, narrowing the wire's diameter increases its band gap, compared to the bulk material. Controlled growth of non-carbon based 1D structures at well-defined locations has been demonstrated only in few examples. Therefore, an understanding of the growth kinetics, the physical and chemical processes on the nanoscale, and their dependence on the growth parameters and template properties is necessary. Researchers are making impressive progress in growing nanowires with precisely controlled properties with all sorts of different technologies including the realization of atomically abrupt heterostructure interfaces inside a nanowire. This better control could give nanowires an edge over carbon nanotubes in some of the same early applications ranging across sensors, batteries, solar cells, medical diagnostics, and high performance electronic devices.

With respect to sensors we demonstrated the formation of a complementary metal-oxide semiconductor (CMOS) compatible micro scale pH sensor with an antimony (Sb) nanowire (NW) network as the solid state pH electrode. The sensor is formed combining well known semiconductor processing techniques with a focused ion beam (FIB) based approach inducing the self assembled formation of Sb nanowires in room temperature ambient without using any additional material source.

As reliable contacts for nanoscale electronic devices we explored an approach for the formation, of copper-germanide/germanium nanowire heterostructures with atomically sharp interfaces. The copper-germanide (Cu_3Ge) formation process is enabled by a chemical reaction between metallic Cu pads and vapor-liquid-solid (VLS) grown Ge-NWs. The atomic scale aligned formation of the Cu_3Ge segments is controlled by in situ SEM monitoring thereby enabling length control of the intrinsic Ge-NW down to a few nm. The single crystal Cu_3Ge/Ge/Cu_3Ge heterostructures were used to fabricate p-type Ge-NW field effect transistors with Schottky Cu_3Ge source/drain contacts.

Formation of Coherent PbTe Nanocrystals in MBE-Grown PbTe/CdTe Heterostructures

H. Groiss[1], F. Schäffler[1], G. Hesser[2], N. Zakharov[3], P. Werner[3], K. Koike[4], M. Yano[4]

[1]Institute of Semiconductor Physics, Johannes Kepler University, Linz, Austria
[2]ZONA, Johannes Kepler University, Linz, Austria
[3]Max Planck Institut für Mikrostrukturphysik, Halle, Germany
[4]Osaka Institute of Technology, Osaka, Japan

We have demonstrated a novel approach for the synthesis of epitaxial quantum dots, which is based on phase separation between two lattice-type mismatched, immiscible materials in a coherent heterostructure fabricated by molecular beam epitaxy [1]. This principle is applied to the PbTe/CdTe semiconductor system, a combination of a rock salt and the zinc blende lattice of CdTe, which show almost identical lattice constants. Upon thermal annealing, 2D PbTe epilayers are transformed into quantum dots (QD) with highly symmetric shapes (see Fig. 1) and atomically sharp heterointerfaces [2], [3]. Efficient photo- [1] and electroluminescence [4] from the QDs in the mid infrared spectral range has been demonstrated.

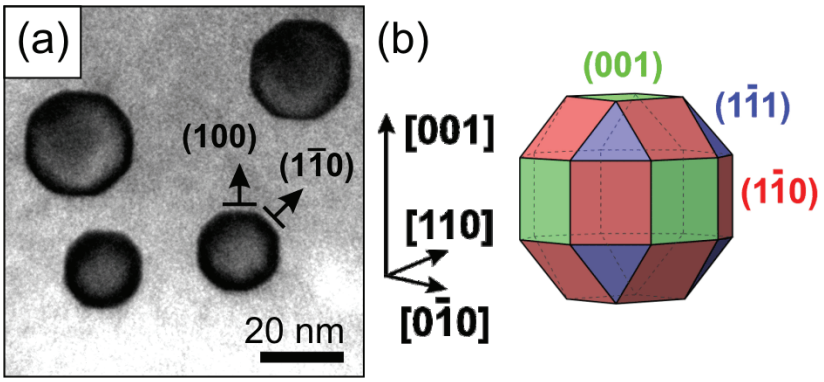

Fig. 1: (a) Plan view, bright field TEM image of PbTe QDs coherently embedded in a CdTe host. (b) Rhombi-cubo-octahedral shape of the highly symmetric QDs.

To monitor the formation kinetics, we performed in situ annealing experiments with a heatable TEM sample holder. Time resolved measurements reveal the kinetics of the complete disintegration process, which is either governed by interface or bulk diffusion processes. The starting points of this evolution are small CdTe columns penetrating the PbTe epilayer. These columns start to grow laterally and merge, which leads to local trapping of PbTe regions in the form of elongated islands. These islands then develop constrictions and finally small islands are separated. Subsequently, the islands evolve

into the highly symmetric equilibrium shape of a small rhombi-cubo-octahedron, which is defined by atomically sharp {011}, {011} and {111} interfaces (Fig. 1).

We monitored the different stages from the breaking-up of the 2D layer over the ripple-like PbTe network towards the formation of PbTe QDs in their equilibrium shape. The formation processes are governed by interface diffusion until dots with their final material volume are separated from the PbTe network. The breaking-up of the 2D layer and the disintegration of the wire-like structure are induced by capillary instabilities and driven by interface energy minimization. Separated dots can also reconnect under special conditions and can use the fast interface diffusion to reach the equilibrium shape. Only ripening processes of separated islands, which need longer annealing times or higher temperatures in comparison to the dot formation parameters, are governed by bulk diffusion. These can be quantified by following the disappearing of small dots below a critical radius.

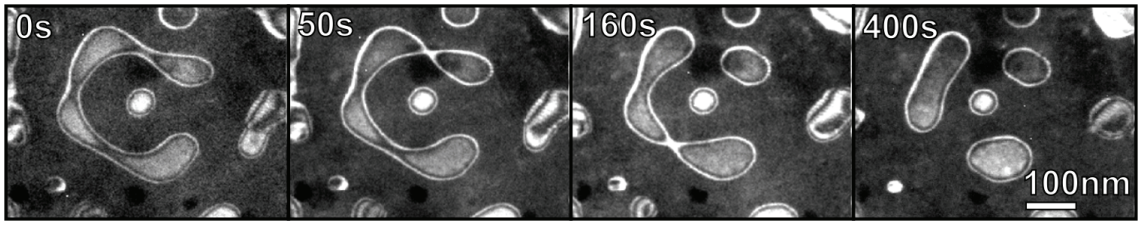

Fig. 2: Formation of three PbTe QDs from one precursor PbTe island. The precursor island shows three constrictions caused by capillary instability. One constriction disappears after separation of two QDs. The following shape transformation leads to a decrease of the distance to the dot in the centre. Also, the disappearing of a small island near the lower border of the frame is observed.

Discussions with W. Heiss and G. Springholz are gratefully acknowledged. This work financially supported by FWF, via project SFB 025.

References

[1] W. Heiss et al., Applied Physics Letter 88, 192109 (2006).

[2] R. Leitsmann et al., New Journal of Physics 8, 317 (2006).

[3] H. Groiss et al., Physical Review B 79, 235331 (2009).

[4] A. Hochreiner et al., Appl. Phys. Lett. 98, 021106 (2011)

[5] H. Groiss et al., Applied Physics Letter 91, 222106 (2007).

Self-Seeded Growth of InAs Nanowires: Fundamental Growth Study and Complex Structures

B. Mandl[1,2], J. Stangl[1], G. Bauer[1], K. Deppert[2]

[1]JKU Linz, Austria
[2]Lund University, Sweden

Due to the possibility to epitaxially grow high quality heterostructures under a large lattice mismatch, semiconductor nanowires have received a lot of interest. Especially the combination of III-V compound semiconductors with Si is an attractive combination for applications. Most nanowire growth methods use Au particles to seed the one-dimensional growth. This poses a severe setback for electronic and optoelectronic applications, as Au is a deep-trap in Si, effectively making the Si useless for electrical applications. To overcome this problem, mechanisms for Au-free III-V nanowire growth have been developed, like self-seeded particle-assisted growth (SPAG) and selective area growth (SAG).

In this poster an overview over the outcome of our group over the last years of research on this topic are presented.

The results include extensive studies performed to deepen the understanding of InAs nanowire growth using a SiO_x mask layer. In the progress of this work it is shown that SPAG is the only possibility to describe the experimental findings [1].

Additionally, the temporal development of nanowire length and diameter are studied. Results obtained by growing 3 sample series, each evaluating the nanowire dimensions over growth time, are used as basis for a surface diffusion model describing nanowire growth. Interestingly, the only way to explain the obtained results is by assuming that only a single crystal layer at a time can grow at a wire mantle facet.

Using the knowledge of these fundamental studies, we tried to understand more complex and completely new systems:

First, we studied the position-controlled growth of InAs nanowires on Si substrates, which is achieved by a SiO_2 mask layer into which openings are etched. Using patterns with different opening dimensions, we can show that the nanowire dimensions for opening dimension ranging from 80 – 250 nm are independent of the opening size. In addition, much larger openings are tested as well, yielding the growth of crystallites instead of nanowires. This result is in agreement with the observations of the growth mechanism study and can be explained by a liquid In particle seeding nanowire growth.

In a second study the possibility to growth axial InAs/InAsP heterostructures is tested. As it is known that SPAG leads to nanowire growth, such heterostructures should be possible to achieve, if the particle can be preserved during the change of the group V precursor ratio. Here we will demonstrate the method used to obtain such a result, and how such a heterostructure typically looks like.

In a last project the principal possibility to grow another material with SPAG supported by a SiO_x layer is investigated. We can demonstrate that InSb wires can be grown in a self-seeded mechanism using the same type of sample preparation [2].

In conclusion, we demonstrated that self-seeded particle-assisted growth of nanowires is a versatile tool for nanowire growth. Still, many detailed aspects of this growth method remain to be investigated, offering exciting research opportunities.

References

[1] B. Mandl *et al.*, Nano Letters, 10 4443-4449 (2010)

[2] B. Mandl *et al.*, Nanotechnology, 22 145603 (2011)

Intersubband Plasmons in InGaAs Quantum Wells

A. Pfnier[1], M. Coquelin[1], A.M. Andrews[1], P. Klang[1], H. Detz[1], P. Bakshi[2], G. Strasser[1], E. Gornik[1]

[1] Center for Micro- and Nanostructures and Institute for Solid-State Electronics,
Vienna University of Technology, 1040 Wien, Austria
[2] Physics Department, Boston College, Chestnut Hill MA 02467, USA

The excitation of intersubband plasmons (ISP) is a promising new effect for the design of novel THz emission sources. The effect studied in this work is based on the interaction of two resonant plasmon modes. To study this phenomenon a special nanostructure was designed [1], [2]. The core of the structure consists of an RTD and an InGaAs well, providing three energy levels. The idea is to bring the energy difference between the higher energies ΔE_{32} in resonance with the energy difference of the two lower levels ΔE_{21} by tuning the energy levels with occupation differences. As the lowest level is highly populated, the inversion between the levels E_3 and E_2 is achieved by injection of electrons into the third level and the extraction from the second level by the RTD. This way the ISPs can be tuned into resonance by depolarization shifts which depend on the population differences. The coupling between these two ISPs can result in a plasma instability providing growing plasma modes at a resonance frequency $\hbar\omega_r = \Delta E_{31}/2 = (\Delta E_{21}+\Delta E_{32})/2$. This process can be described as a collective electron-electron scattering process [1]. The resonance leads to a very strong extraction of trapped electrons from the lowest level. The lowest level is refilled by an efficient scattering process $3 \rightarrow 1$. The strength of the effect is related to an interplay between the extracting resonant plasmon process and the refilling scattering process. We have grown three samples with varying InGaAs well widths ((a) 31 nm, (b) 28.2 nm, and (c) 26.8 nm) resulting in a variation of E_{31}. Thereby the calculated values for E_{31} ((a) 31 meV, (b) 37 meV, and (c) 40 meV) vary around the LO phonon frequency. Due to the filling of the lowest level, charging leads to a lowering of the energy difference E_{31} resulting in a blocking of the LO phonon process. The resonant plasmon effect is also evident directly in the IV-curves. When the two ISP resonances are tuned to equal values by the injected current a sharp increase of the current is observed.

References

[1] P. Bakshi, K. Kempa, Physica E 7, 63 (2000)

[2] M. Coquelin, G. Strasser, E. Gornik, P. Bakshi, M. Ciftan, Appl. Phys. Lett. **95** (17), 172108 (2009)

Reversible Nanofacetting and 1D Ripple Formation of Ge on High-Indexed Si (11 10) Substrate

B. Sanduijav, D. Matei and G. Springholz

Institute for Semiconductor Physics, Johannes Kepler University, 4040 Linz, Austria

Silicon-germanium has been an intensely studied model system for the growth of self-assembled quantum dots by the Stranski-Krastanow mode. A prominent feature of these dots is their highly facetted pyramidal or dome-like shape [1] that is governed by the formation of energetically favored side facets. The formation of the different dot shapes not only depends on the Ge coverage and growth condition, but also on the substrate orientation [2]. The (11 10) Si substrate orientation is special because of its particular relationship to the low energy {105} facets of compressively strained Ge pyramids, in which case the intersections of these facets are parallel to the (1110) surface. In addition, local (1 1 10) Si substrate facets also play a major role in site-controlled growth of Ge islands on pit-patterned or stripe-patterned Si substrate templates [3], [4].

In the present work, Ge growth on high-indexed (11 10) substrates was studied systematically using *in situ* variable temperature scanning tunneling microscopy. The experiments were performed in a multi-chamber MBE/STM system, allowing sequential growth and imaging of the epitaxial surface structure formed after each growth step [4]. The results demonstrate that the (1110) growth properties radically differ from those on the usual (001) Si substrates. At certain critical coverage of ~4 monolayers (ML), a highly stable quasi-periodic 1D ripple structure is formed perpendicular to the dimer direction. As demonstrated by Fig. 1 (1) well defined {105} facetted ripples completely cover the whole (1110) substrate surface, in contrast to the usual isolated Ge islands formed by the Stranski-Krastanow growth mode on (001) surface.

A quantitative analysis shows that in the ripple formation process, the initial 2D Ge wetting layer is completely consumed, i.e., no wetting layer remains underneath the ripples. Thus, the ripples represent a novel pathway for lowering the free energy of the system. Moreover, the ripples show a well defined and unique width and height with a lateral periodicity of ~20 nm with a rather narrow size dispersion. Most strikingly, during thermal cycling of the Ge layers on Si (1110), a reversible transition from the rippled surface to a flat surface is found to occur when the annealing temperature is raised above a critical temperature of 600 °C. This process is reversed when the temperature is lowered again. This was demonstrated by the variable temperature STM image in Fig. 1 (2), where the rippled surface was heated from 500 °C to 590 °C and then cooled down again to 500 °C. Moreover thermal cycling was monitored using RHEED, that the intensity evolution of the ripple spot present hysteresis behavior during multiple heating and cooling cycles. Both factors clearly demonstrate that the ripples represent an equilibrium structure and their formation closely resembles a thermodynamic phase transition.

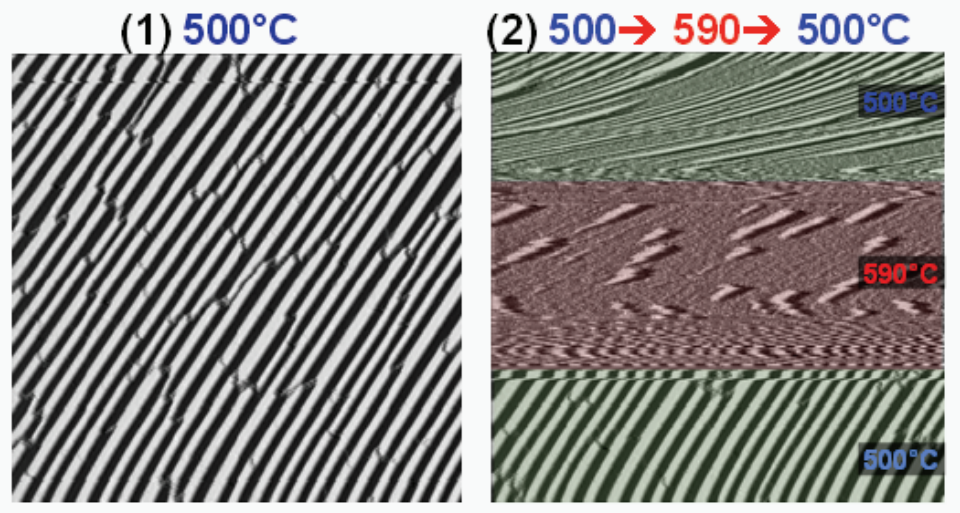

Fig. 1: Reversible ripple formation is demonstrated via variable temperature STM images. (1) {105} facetted ripple covered surface at 500 °C, corresponding Ge coverage is 4.5ML. Right: the sample was annealed from 500 °C to 590 °C using DC current. Ripple structure almost disappears at 590 °C and then reappears at 500 °C within few seconds.

References

[1] *see* M. Brehm, et al., Nanoscale Research Letters (in print) and references therein.

[2] J.T. Robinson, A. Rastelli, O. Schmidt and O.D. Dubon, Nanotechnology **20**, 085708 (2009).

Pre-Defined SiGe Island Growth on Large-Area, High-Density Pit-Patterned Si Substrates Fabricated by UV Nanoimprint Lithography

E. Lausecker[1], M. Brehm[1], M. Grydlik[1], F. Hackl[1], I. Bergmair[2], M. Mühlberger[2], T. Fromherz[1], F. Schäffler[1], G. Bauer[1]

[1]Institute of Semiconductor and Solid State Physics, University of Linz, 4040 Linz, Austria.
[2]Functional Surfaces and Nanostructures, Profactor GmbH, 4407 Steyr-Gleink, Austria.

We present the fabrication of pit-patterned substrates using ultra-violet nanoimprint lithography (UV-NIL) [1] for the ordered growth of silicon-germanium (SiGe) islands. For the realization of optoelectronic devices and circuits, it is mandatory to precisely address the position and control the size and chemical composition homogeneity of the islands by pits etched into the substrate [2].

We fabricate replica molds for imprinting by a replication process of a Si master. The molds (17.5 x 17.5 mm^2 in size) contain a pillar pattern (Fig. 1 (a)) which is transferred to a hole pattern in the resist during the imprint process. Four fields, each extending over a continuous area of 3 x 3 mm^2 are defined in one imprint step. The hole pattern is transferred to the Si substrate by reactive-ion etching to a depth of 35 nm. We increase the pattern density by reducing the pit period of each field from 260 nm down to 170 nm in steps of 30 nm. The diameter of the pits is reduced as well, down to 120 nm for the smallest period of 170 nm.

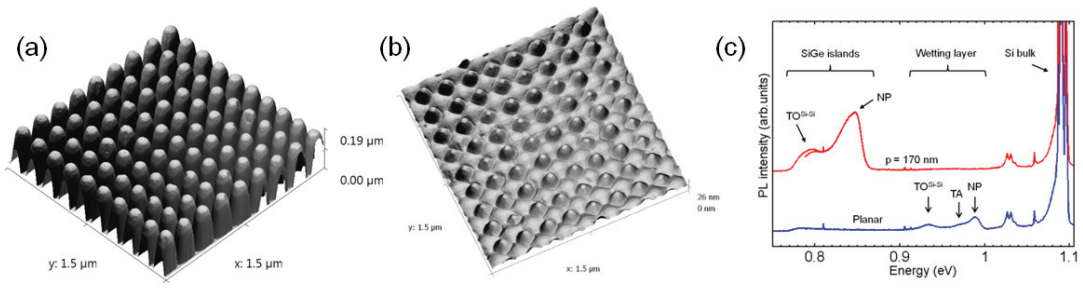

Fig. 1: AFM image of (a) the pillar pattern on a replicated nanoimprint mold and (b) ordered SiGe islands with a period of 170 nm grown at 625 °C with 8.3 ML of Ge. (c) Low temperature (5.5 K) PL spectrum recorded from ordered SiGe islands with a period of 170 nm. The bottom PL spectrum was measured on the planar substrate area.

After the molecular-beam epitaxy growth of a Si buffer layer, 8.3 monolayers of Ge are deposited at 625 °C. Then, the island surface is capped with a 10-nm-thick Si layer.

Atomic force microscopy (AFM) images reveal the nucleation of one SiGe island per pit [Figure 1 (b)]. Photoluminescence (PL) measurements show two narrow peaks for the signal of the ordered islands at 0.79 and 0.85 eV [Figure 1 (c)]. Under these growth conditions, the island-signal shifts to lower energies compared to previous work [3] in which islands were grown at 690 °C with a Ge coverage of 6 ML. Furthermore, dislocations are already introduced in the islands on the planar substrate area, and therefore the PL signal is vanishing.

Our results suggest that UV-NIL opens a route to define high-density SiGe islands with sub-100 nm period over large areas and excellent optoelectronic properties.

This work was performed in the NILaustria project cluster (www.nilaustria.at) and supported by the Austrian NANO Initiative (bmvit and FFG), the IRON project (FWF) and GMe, Austria.

References

[1] S.Y. Chou et al., Science 272, 85 (1996).

[2] Z. Zhong et al., Appl. Phys. Lett. 82, 4779 (2003).

[3] E. Lausecker et al., Appl. Phys. Lett., accepted for publication (2011).

X-Ray Diffraction and Strain Studies on a Single SiGe Quantum Dot Integrated in a Field Effect Transistor

N. Hrauda[1], J.J. Zhang[1], J. Stangl[1], D. Carbone[2], C. Biasotto[3], V. Jovanovic[3], L.K. Nanver[3], J. Moers[4], D. Gruetzmacher[4], and G. Bauer[1]

[1]Institute of Semiconductor and Solid State Physics, University of Linz, 4040 Linz, Austria
[2]European Synchotron Radiation Facility, Grenoble, France
[3]DIMES, TU Delft, Delft, The Netherlands
[4]IBN-1, Forschungszentrum Jülich GmbH, Jülich, Germany.

We report on the analysis of a single island in a 2D periodic array of SiGe dots. The sample was grown by MBE on e-beam pitpatterned Si (001) substrates and capped with Si for the realization of an n-channel DotFET device. These devices employ epitaxially grown SiGe dots for as stressor for a Si channel to achieve higher tensile strain values compared to conventional Si based MOS devices [1]. We successfully recorded reciprocal space maps of the (004) and (224) Bragg peak of a single SiGe dot with a diameter of 220 nm integrated in a fully processed device with a TiN + Al(1%Si) gate stack and source, gate and drain contacts in place, employing a 400 nm focused X-ray beam at the ID01 beamline of the ESRF in Grenoble [2]. Strain fields in the dot and the Si channel were determined using FEM and X-ray simulations, with the experimental data serving as reference. A maximum in-plane tensile strain of 1% in the Si channel was found, substantially higher than achievable for dislocation-free tensile strained Si on planar substrates.

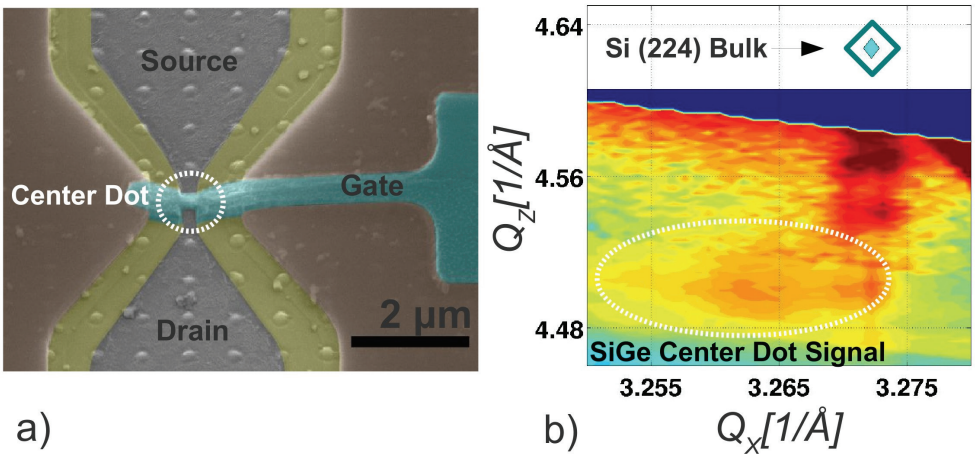

Fig. 1: (a) SEM image of the transistor structure with source and drain contacts not yet in place, the gate finger is perfectly aligned to a single dot. The region labeled 'center dot' was probed in the X-ray experiments, panel (b) shows the corresponding reciprocal space map.

The electrical evaluation of this transistor was performed by comparing to non-strained reference devices processed on the same wafers but without dots: the DotFET showed an increase of drain current between 20 and 60 % [3].

This work was supported by the EC d-DOTFET project (012150-2) and the FWF Vienna (SFB025 IR-On).

References

[1] R. A. Donaton *et al.*, IEDM'06, 346813 (2006).

[2] Mocuta *et al.*, PRB 77, 245425 (2008)

[3] Jovanović *et al.*, IEEE Electron Device Letters, 31, 1083-1085 (2010)

Novel Materials and Technologies

Microstructural and Electrical Analyses of Oxygen Diffusion into Iridium Metal Gates

A. Alexewicz[1], C. Ostermaier[1*], G. Pozzovivo[1*], W. Schrenk[1], M. Schmid[2], L. Tóth[3], B. Pecz[3], J.-F. Carlin[4], M. Gonschorek[4], N. Grandjean[4], J. Kuzmik[1,5], D. Pogany[1] and G. Strasser[1]

[1]Institute of Solid State Electronics, Vienna University of Technology, Vienna, Austria
[2]Institute of Applied Physics, Vienna University of Technology, Vienna, Austria
[3]Research Institute for Technical Physics and Material Science, Budapest, Hungary
[4]Institute of Quantum Electronics and Photonics, EPFL Lausanne, Switzerland
[5]Institute of Electrical Engineering, SAS Bratislava, Slovak Republic
***now: Infineon Technologies Austria AG, Villach, Austria**

Iridium is used as gate metal for GaN-based $In_{0,17}Al_{0,83}N$/AlN barrier High Electron Mobility Transistors (HEMTs) 0. Before annealing, a high oxygen concentration confined at the Ir/InAlN interface is detected, but neither an aluminum nor an indium oxide interfacial layer has been formed. In this work we investigate the annealing-induced diffusion of the oxygen-rich interlayer and its electrical effects on the device. No stable iridium oxide forms – instead oxygen is able to diffuse out of the interlayer into the iridium gate metal, thus the interlayer is reduced. Above 700 °C a homogeneous oxygen concentration is observed in the iridium layer, whereas at 500 °C oxygen is distributed inhomogeneously. This behavior is also verified electrically.

The diffusion length of oxygen in evaporated iridium is only in the order of 1 nm for 2 minutes annealing at 500 °C 0. Therefore, oxygen cannot diffuse efficiently in dense iridium at that temperature, so that oxygen diffusion, enhanced by crystal defects and grain boundaries, is assumed. Annealing at 700 °C increases the diffusion length to about 100 nm 0 and allows homogenous diffusion of oxygen into iridium, leading to the most complete removal of the oxygen interlayer, as seen from the C-V-measurements. Additionally, the analysis of the microstructure proves that the thickness of the InAlN/AlN barrier does not change after annealing and metal does not diffuse into the barrier. That confirms the already proven robustness of InAlN.

The rapid thermal annealing was performed for 2 minutes at 400 °C, 500 °C and 700 °C. Two samples with different gate metals (iridium and nickel) are analyzed in order to investigate the dependence on the metal. High-Resolution Transmission Electron Microscopy (HRTEM) gives detailed analysis of the microstructure at the different interfaces. Electron Energy Loss Spectroscopy (EELS) shows the two-dimensional element distribution in the samples. I-V- and C-V-measurements are used to determine the electrical properties.

References

[1] C. Ostermaier, G. Pozzovivo, W. Schrenk, M. Schmid, L. Tóth, B. Pecz, J.-F. Carlin, M. Gonschorek, N. Grandjean, J. Kuzmik, D. Pogany, and G. Strasser "Metal-related Gate Sinking due to Interfacial Oxygen Layer in Ir/InAlN High Electron Mobility Transistors", Applied Physics Letters 96, 263515 (2010)

[2] C. U. Pinnow, I. Kasko, N. Nagel, S. Poppa, T. Mikolajick, C. Dehm, W. Hösler, F. Bleyl, F. Jahnel, M. Seibt, U. Geyer, and K. Samwer *"Influence of deposition conditions on Ir/IrO_2 oxygen barrier effectiveness"*, Journal of Applied Physics 91 (12), 9591 (2002)

ALD Based La_2O_3 Ge Interface Passivation for High Performance MOS-Device Applications

O. Bethge[1], C. Henkel[1], S. Abermann[1], H. Hutter[2], J. Smoliner[1] and E. Bertagnolli[1]

[1]Institute for Solid State Electronics, Vienna University of Technology, 1040 Vienna, Austria
[2]Institute of Chemical Technologies and Analytics, Vienna University of Technology, 1060 Vienna, Austria

Ge is the most attractive channel material for next generation p-channel metal-oxide semiconductor (pMOS) devices due to its highest hole mobility and its low dopant activation temperatures. The disadvantage of Ge not to offer a stable, natural homogenous oxide requires the application of an "extrinsic" heterogeneous oxide in terms of electrical and chemical compatibility. For ultrathin dielectric layers envisaged for future CMOS-devices, Atomic Layer Deposition (ALD) is one of the favored deposition processes for high-*k* dielectric materials due to its high uniformity, high conformity, and excellent thickness controllability of the layers. Several very capable approaches for Ge surface passivation techniques have been reported, and superior electrical behavior of the dielectrics by using Atomic Layer Deposition (ALD) mainly on interfacial GeO_2 has been observed. The rare earth oxide La_2O_3 is one of the most promising high-k dielectrics in order to passivate the hardly controllable Ge interface. It seems that La_2O_3 passivations can uniquely meet required scaling abilities and low interface trap densities. In this discussion, both aspects will be addressed: On the one hand, it will be shown that ALD grown La_2O_3 is capable to reach 0.5 nm equivalent oxide thickness (EOT) and on the other hand, a strong reduction of interface trap densities down to mid-10^{11} $eV^{-1}cm^{-2}$ will be presented by a Pt-assisted annealing approach of La_2O_3/ZrO_2 oxide stacks. Conductance measurements also indicate the absence of compromising mid-gap traps by using La_2O_3 passivation layers.

This work is funded by the Austrian Science Fund (FWF), project No. P19787-N14. The Gesellschaft für Mikro- und Nanoelektronik (GMe), as well as the ZMNS, are gratefully acknowledged.

References

[1] ITRS (2009), http://www.itrs.net/.

[2] Y. Kamata, Mater. Today 11, 30 (2008).

[3] A. Dimoulas et al., Appl.Phys.Lett. 96, 012902 (2010).

[4] S. Abermann et al., Appl.Phys.Lett. 94, 262904 (2009).

[5] C. Henkel et al., Appl.Phys.Lett., 97, 1529041 (2010).

[6] O. Bethge, et al., Appl.Phys.Lett. 96, 052902 (2010).

Sensors

Utilizing Pressure Waves for Sensing the Properties of Liquids

H. Antlinger[1], R. Beigelbeck[2], S. Clara[1], S. Cerimovic[3], F. Keplinger[3], B. Jakoby[1]

[1] Institute for Microelectronics and Microsensors, Johannes Kepler University Linz, 4040 Linz, Austria
[2] Institute for Integrated Sensor Systems, Austrian Academy of Sciences, 2700 Wiener Neustadt, Austria
[3] Institute of Sensor and Actuator Systems, Vienna University of Technology, 1040 Vienna, Austria

We report on a concept for a fluid sensor utilizing pressure waves for sensing the fluid properties (e.g. viscosity, sound of speed). The detection of fluid properties is of importance for many technical processes. Requirements for such sensors are small size, robustness, lightweight and a reasonable price. An approach utilizing pressure instead of shear waves is introduced. With this approach it is possible to overcome the drawback of the small penetration depth of shear waves in liquids. The theoretical background, a simple 1D model, simulation results and first measurement results are presented.

Introduction

Sensors for liquid condition monitoring are an important asset for process control. Industrial applications require reasonably priced sensors which are small in size, lightweight, robust, need little maintenance, and are preferably suited for online monitoring. A lot of recent work has been focused on viscosity sensors (see e.g. [1]). Laboratory equipment for determining the shear viscosity involves motors and rotating objects immersed in the liquid and is commonly bulky, maintenance intensive, and not suitable for online monitoring. Miniaturized sensors for fluid viscosity (e.g. small, vibrating structures immersed in the liquid) often utilize shear vibrations. With these devices only a thin film of the liquid is measured, due to the small penetration depth (in the range of a few micrometers depending on the exciting frequency) of the shear waves [1]. To overcome this crucial disadvantage for many applications we use an alternative approach which is based on pressure waves such that the bulk of the sample is probed. With this approach instead of the shear viscosity the so-called longitudinal viscosity is determined, which can be equally useful for condition monitoring. At the moment material data for the longitudinal viscosity of fluids is rare because this parameter has not been widely experimentally investigated. Some experimental studies determining this parameter using the principle of acoustic spectroscopy can be found in [2], [3]. Compared to this laboratory equipment based approaches, we intend to achieve an integrated, resonant sensor system.

Theory

We use an approach based on the attenuation of pressure waves in a fluid. From the theory of acoustic wave propagation, the behavior of pressure waves in liquids is well known [4]. Figure 1 shows the basic arrangement of the sensor. Two parallel boundaries separated by a distance *h* form a sample chamber. One boundary carries a trans-

ducer which imposes pressure waves, resonating between the two boundaries, in the liquid. In addition to using the transducers impedance change as sensor output signal the second boundary can be optionally equipped with a pressure sensor whose output can also be used as sensor signal.

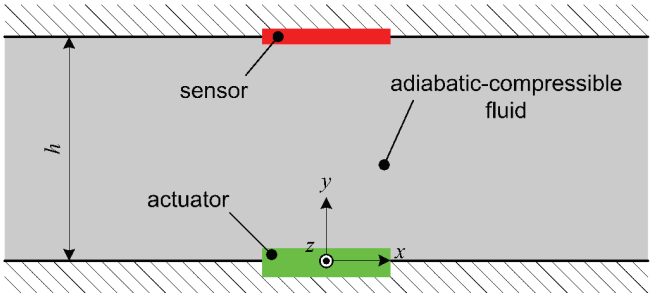

Fig. 1: Basic sensor arrangement.

Solving the linearized two-dimensional Navier-Stokes equation (displacement vector **u**, mass density ρ_0, and adiabatic compressibility ζ_S, μ is the coefficient which represents the shear viscosity and is often only termed viscosity, λ represents the dilatational viscosity associated with compressional stress components)

$$\rho_0 \ddot{\mathbf{u}} = \frac{1}{\zeta_S} \nabla(\nabla \cdot \mathbf{u}) + (\mu + \lambda) \nabla(\nabla \cdot \dot{\mathbf{u}}) + \mu \nabla^2 \dot{\mathbf{u}}$$

by using complex notation for time-harmonic signals and the spatial Fourier transform leads to an approximate solution for the fields which shows, that the attenuation due to viscous damping will always approximately depend on (λ+2μ) and that the two parameters can not be separated. So this concept only allows the measurement of the longitudinal viscosity (λ+2μ), [5] – [8].

Figure 2 shows the 1D model for the sensor setup. For the PZT disk, a commonly used three port model was applied [9], the fluid was modeled as acoustic transmission line and the boundaries of the fluid chamber as acoustic impedance. For a more detailed discussion see [5] – [7], [9].

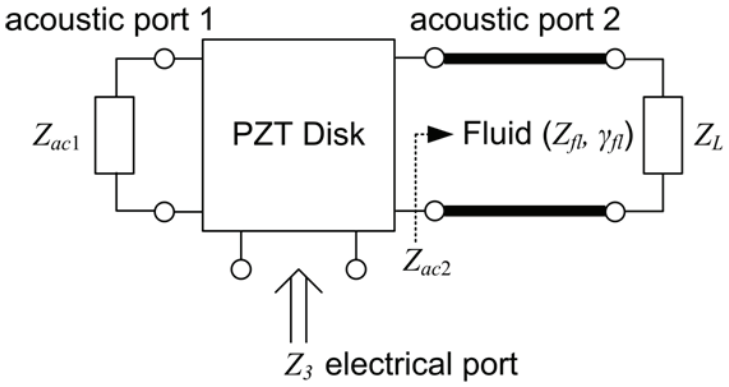

Fig. 2: 1D sensor model.

Results

In this section we provide some illustrative sample results of the approach, for more details we refer to [5] – [7]. Figure 3 shows simulation results for the 1D model with different media in the sample chamber while Fig. 4 shows measurement results obtained with a first prototype device. In this sensor setup, the fluid represents a resonating acoustic transmission line which yields a comb-like pattern in the transducer impedance. The spacing can be used to determine the sound velocity in the liquid while the damping is associated with the longitudinal viscosity [5]. The differences between model and experiment can be explained by several losses which are not yet included in the model such as losses induced by the mounting of the PZT disk and the non-ideal reflection of the acoustic wave at the boundaries.

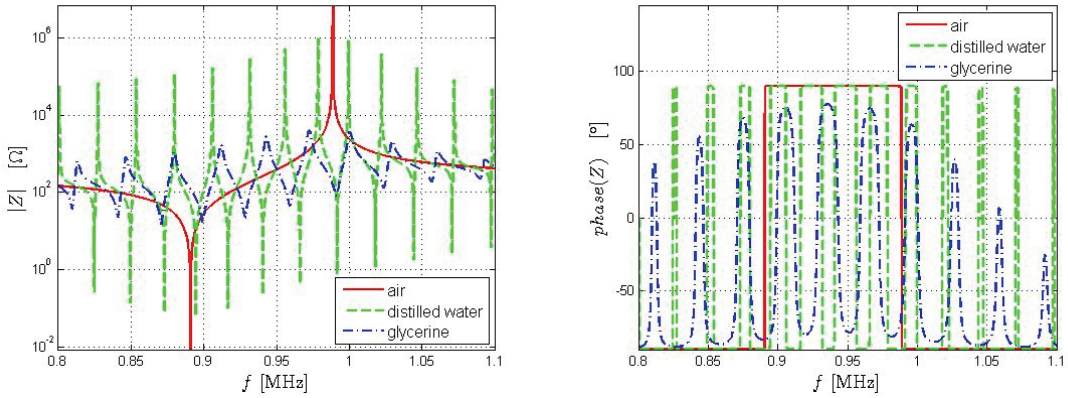

Fig. 3: Magnitude and phase of the piezo transducer for different media (simulation).

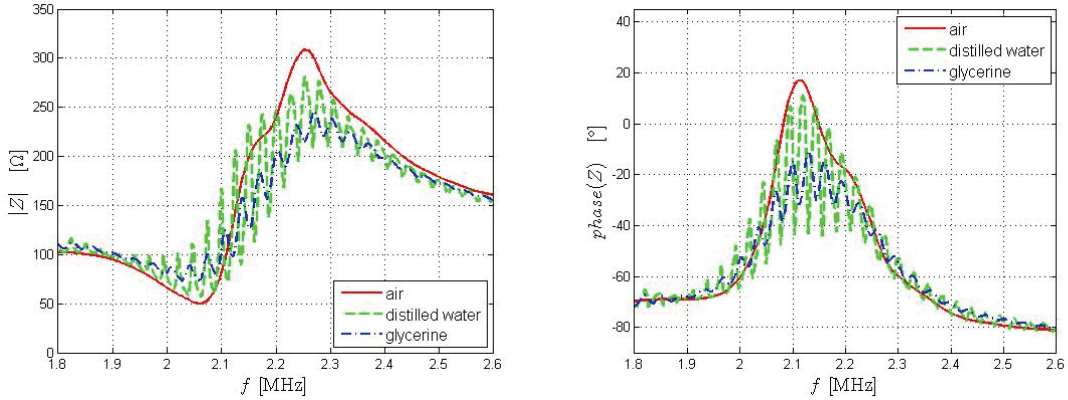

Fig. 4: Magnitude and phase of the piezo transducer for different media (measurement).

Conclusion

We presented a concept for a sensor measuring the so-called longitudinal viscosity. Results obtained with a first prototype device show a clear dependence of the electrical impedance on the fluid parameters. In particular the damping of the resonances is related to the viscosity and the spacing of the comb like resonances depends on the

speed of sound in the fluid. The simple 1D model enables qualitative predictions of the experimentally generated data but needs further refinements to narrow the gap between simulation and measurement data.

Acknowledgements

This work was supported by the Austrian Science Fund (FWF), grant L657-N16 and by the COMET K-project “Process Analytical Chemistry”.

References

[1] B. Jakoby, R. Beigelbeck, F. Keplinger, F. Lucklum, A. Niedermayer, E. Reichel, C. Riesch, T. Voglhuber-Brunnmaier, and B. Weiss, “Miniaturized sensors for the viscosity and density of liquids - performance and issues,” IEEE Trans. on Ultrason., Ferroelec., and Freq. Contr., vol. 1, no. 57, pp. 111–120, 2010.

[2] M.J. Holmes, N.G. Parker and M.J.W. Povey, “Temperature dependence of bulk viscosity in water using acoustic spectroscopy,” Journal of Physics: Conference Series, Proceedings of the Anglo-French Physical Acoustics Conference, January 2010, arXiv:1002.3029v1 [physics.flu-dyn].

[3] Andrei S. Dukhin and Philip J. Goetz , “Bulk viscosity and compressibility measurement using acoustic spectroscopy,” J. Chem. Phys. 130, 124519 (2009).

[4] L.D. Landau, E.M. Lifshitz, Fluid Mechanics, Second Edition: Volume 6 (Course of Theoretical Physics), Butterworth-Heinemann, 1987.

[5] H. Antlinger, R. Beigelbeck, S. Clara, S. Cerimovic, F. Keplinger, and B. Jakoby, “A liquid properties sensor utilizing pressure waves”, Proc. SPIE 8066, 80661Z (2011); doi:10.1117/12.886357

[6] H. Antlinger, R. Beigelbeck, S. Cerimovic, F. Keplinger, and B. Jakoby, “A sensor for mechanical liquid properties utilizing pressure waves”, Sensor + Test Conference 2011, Nürnberg, June 2011.

[7] H. Antlinger, S. Clara, R. Beigelbeck, S. Cerimovic, F. Keplinger, and B. Jakoby, “Utilizing acoustic pressure waves for sensing fluid properties”, Eurosensors 2011, Athens, September 2011 (to appear).

[8] Beigelbeck, R., and Jakoby, B. “A two-dimensional analysis of spurious compressional wave excitation by thickness-shear-mode resonators,” Journal of applied physics, 95(9):4989-4995, May 2004.

[9] Kino, Gordon S., Acoustic waves: devices, imaging, and analog signal processing, Prentice-Hall, Inc. 1987.

A Feasibility Study on Tunable Resonators for Rheological Measurements

M. Heinisch[1], E.K. Reichel[2] and B. Jakoby[1]

[1]Institute for Microelectronics and Microsensors, Johannes Kepler University, 4040 Linz, Austria
[2]Center for Surface Science and Catalysis, Katholieke Universiteit Leuven, 3001 Heverlee, Belgium

A feasibility study on resonating sensors for rheologic properties such as viscosity, facilitating measurements at tunable frequencies in the low kHz range is presented. Results from analytical models relating measurement data to the viscosity are compared to measurement results from sample liquids. The benefits of the presented sensor designs in terms of high tunability and their sensitivity to viscosity are briefly discussed.

Introduction

The emphasis of the work summarized here is on miniaturized, tunable, resonating rheometers in which we presently focus on two main aspects: Large penetration depths (of shear waves which are excited in the examined liquid by the resonator) and high tunability (of the resonator's resonance frequency). To allow for large penetration depths (several micrometers in case of aqueous liquids), the oscillator's resonance frequencies should be in the low kilohertz range. Large penetration depths become important when examining complex liquids such as multi-phase fluids such as, e.g., emulsions. For the investigation of liquids showing shear thinning (or thickening) or viscoelastic behavior, it is necessary to record the liquid's characteristics not only at one single frequency but in a range of different frequencies, which in the best case should cover several decades of resonance frequencies. For this purpose, especially in the case of resonating micro-sensors, it is desirable to have devices which can be operated at tunable frequencies without changing their geometries.

For this purpose, we designed and investigated two different types of tunable resonating sensors: A wire viscometer and a suspended plate rheometer (Fig. 1). For both concepts reviewed in this work, the ability of tuning the sensor's resonance frequency is based on varying the normal stresses within (resonating) tungsten wires. In both cases, sample liquids are subjected to time harmonic shear stresses induced by the resonating wire and the suspended resonating platelet, respectively. From the resulting frequency response the liquid's rheological properties can be deduced by fitting the parameters of an appropriate closed-form model representing the physical behavior of the sensors.

The use of appropriate materials and different micro-fabrication techniques were investigated and the applicability of the devices for rheological measurements was examined. In this contribution, the results from analytical closed form models, which were presented in [1] and [2], are compared to measurement results, and the capability of the particular resonator for accurate and reliable sensing is discussed.

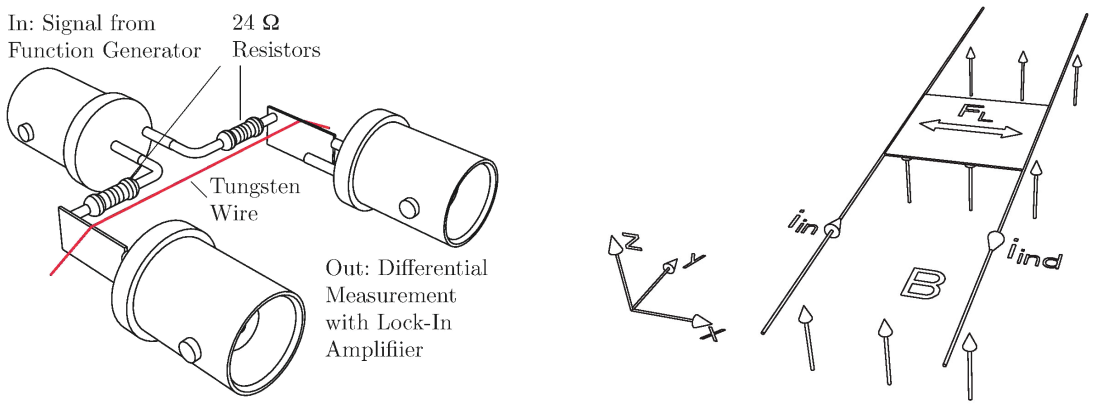

Fig. 1: Principles of the investigated sensor designs: Wire viscometer (left) and suspended plate rheometer (right).

Experimental Setups

Figure 1 shows the schematic drawings of the investigated sensor principles. The figure on the left shows the basic design of the wire viscometer. A 100 µm thick tungsten wire carrying sinusoidal currents is placed in an external magnetic field (not depicted) and thus oscillating due to Lorentz forces. For excitation, a function generator is connected to two 24 Ω resistors being connected in series with the tungsten wire. These resistors are used to limit the excitation current. For measuring the motion-induced voltage as read-out, a lock-in amplifier is used. On the right the suspended plate rheometer is illustrated. The sensor consists of two parallel wires placed in an external magnetic field **B**. In this figure, the left wire is used for exciting lateral vibrations by means of Lorentz forces. The second wire on the right used for pick-up is coupled to the excitation wire with a rigid plate, thus following the movement of the left wire. The induced voltage in the second wire is used as read-out. The platelet inducing (one-dimensional) shear waves into the liquid is the main part interacting with the sample. For both types of sensors, the resonance frequency can be changed by (mechanically) varying the normal stresses in the wires.

Measurements

Measurement Principle

For both types of sensors, their frequency response is recorded by sweeping the sinusoidal excitation current's frequency in the bandwidth of interest (containing the fundamental harmonic) and recording the (motion-) induced voltage with a lock-in amplifier. Once all the parameters of the analytical closed form model (except the fluid's dynamic viscosity and mass density) were identified with a set of calibration measurements, the liquid's viscosity can be determined by fitting the model into the measured resonance curve (already knowing the liquid's mass density which was e.g., evaluated by another measurement).

Electrical Cross Talk

In first measurements electrical cross talk was observed (Fig. 2 (left)). In air this electrical cross talk does not have a significant effect on the signal close to the fundamental harmonic. However, when measuring liquids, this effect can become disturbing. The

wires of the sensor connected to the wires for power supply and measuring form two loops (single-turn coils) with a certain cross-sectional area (Fig. 2 (right)). The magnetic flux generated by the current in the first loop penetrating the second loop induces a voltage in this second loop (Faraday's law) and vice versa. Displacing the wires mostly changes the cross-sectional areas of these loops and thus, resulting in a different induced voltage resulting from this electrical cross talk, making reliable measurements difficult. To reduce the effect of electrical cross talk, BNC-connectors are used, first, to minimize the effective cross-sectional area of the single-turn loops, and second, to keep this cross-sectional area constant, enabling reliable measurement with strongly reduced and constant electrical cross talk.

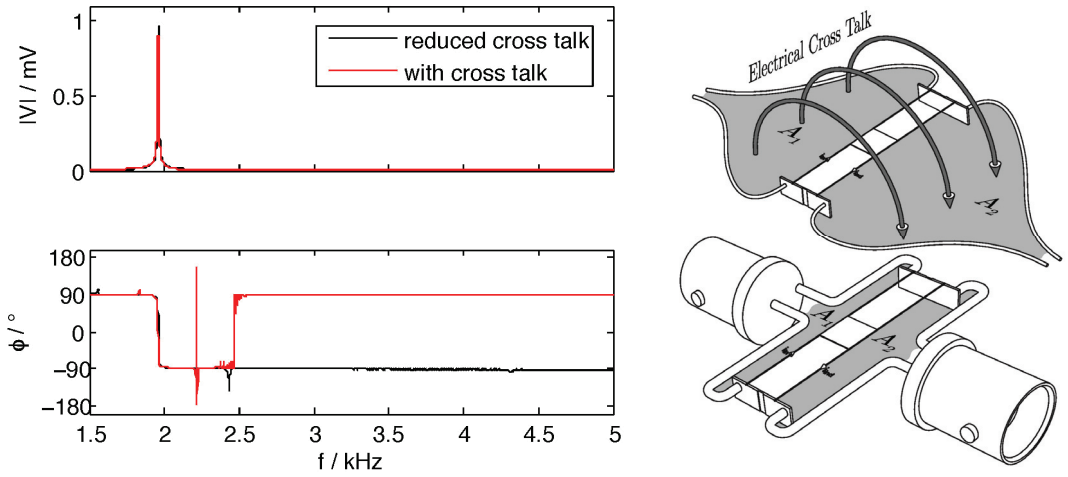

Fig. 2: Effect and explanation of electrical cross talk.

Tunability

The band width of achievable resonance frequencies (in air) using 3 cm long and 100 µm thick tungsten wires were investigated (Fig. 3). In each case a detailed view of one characteristic resonance is depicted as well. In case oft the wire viscometer (left) higher quality factors were obtained. (Note that the depicted bandwidths in the detailed views are 40 Hz for the wire viscometer and 200 Hz for the suspended plate rheometer.) The obtained resonances in these first measurements go from 1000 Hz to 4250 Hz in case of the wire viscometer and from 820 Hz to 4040 Hz for the suspended plate rheometer. In both cases, for changing the resonance frequencies for these measurements, the normal stresses in the wires were varied by tensioning the wires with micro-stages with micrometer screws.

To further investigate the tunable range of a wire when changing both, the normal stresses in the wire as well as its length, a setup as depicted in Fig. 4 was used. The conductive blades allow for electrical contact and for changing the wire's vibrating length. One end of the wire is rigidly affixed. The other is attached to a weight, which is varied for changing the normal stresses in the wire but keeping the normal stresses constant when changing the vibrating length only. On the right hand side of Fig. 4 the results from a theoretic estimation of achievable resonance frequencies, when changing the normal stresses as well as the wire's vibrating length for a 100 µm thick tungsten wire with lengths between 10 mm and 30 mm and normal stresses between 0 and 1.4 GPa, is depicted. (Note: Tungsten features yield stresses of 1.5 GPa, approximately.) These theoretical values were compared with first measuring results, and good accordance was observed.

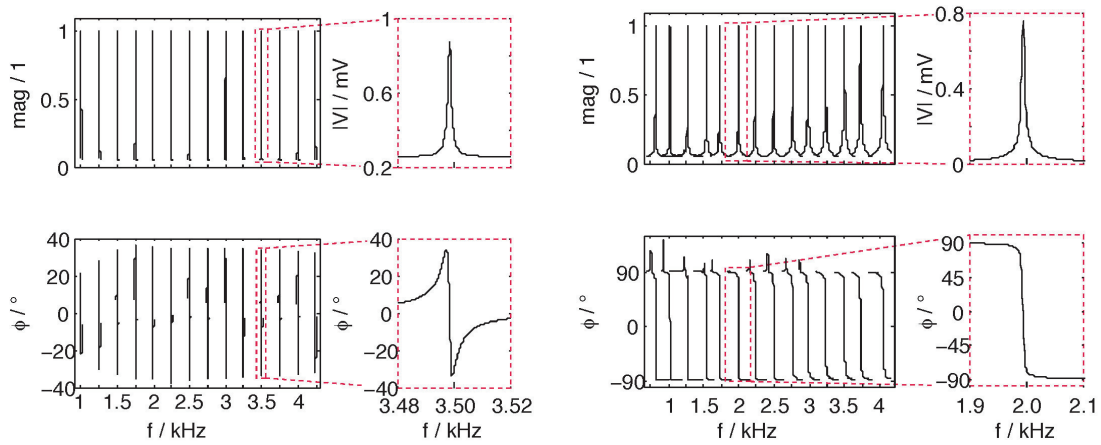

Fig. 3: Tunable range for a 3 cm long, 100 µm thick tungsten wire. Left: Wire viscometer, right: suspended plate rheometer.

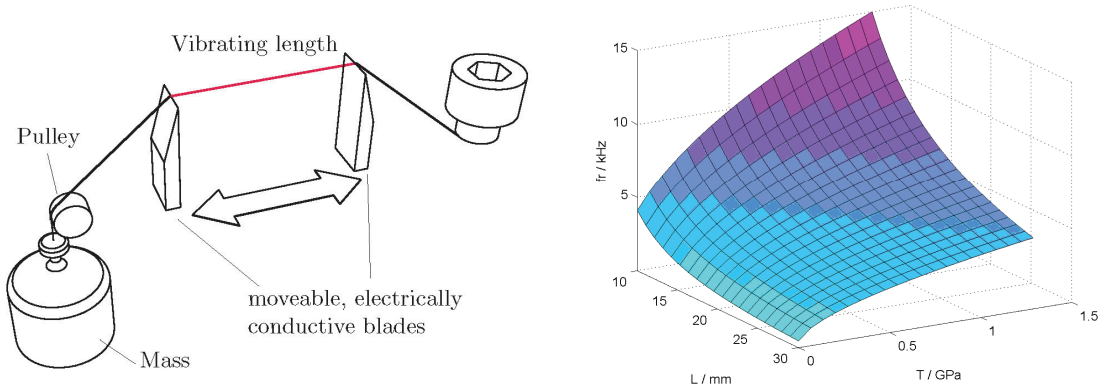

Fig. 4: Tunable range for changing both, normal stresses and vibrating length.

Response to Viscosity

The response to viscosity and the sensitivity to the latter were investigated by immersing the sensors into different sample liquids. Figure 5 shows a comparison of theoretic and measured data for four different liquids. (Acetone: mass-density ρ = 0.78 g/cm^3, dynamic viscosity µ = 0.21 mPas; Methanol: ρ = 0.79 g/cm^3, µ = 0.47 mPas; DI-water: ρ = 1 g/cm^3, µ = 0.86 mPas; Isopropanol: ρ = 0.78 g/cm^3, µ = 2.05 mPas; values measured at 25 °C with an Anton Paar ® SVM3000).

In this case the relative diameter of the resonance circle in the Nyquist plot in respect to DI-water was used as quantity, which relates to the dynamic viscosity. The solid lines represent the theoretic values gained from the models in respect of the according mass density. The dots are results from measurements. A deviation of the predicted (theoretical) values from the measured values is observed, which might be due to drawbacks in the setup and / or the modeling. However, the calculated curve and the measured points show the same behavior.

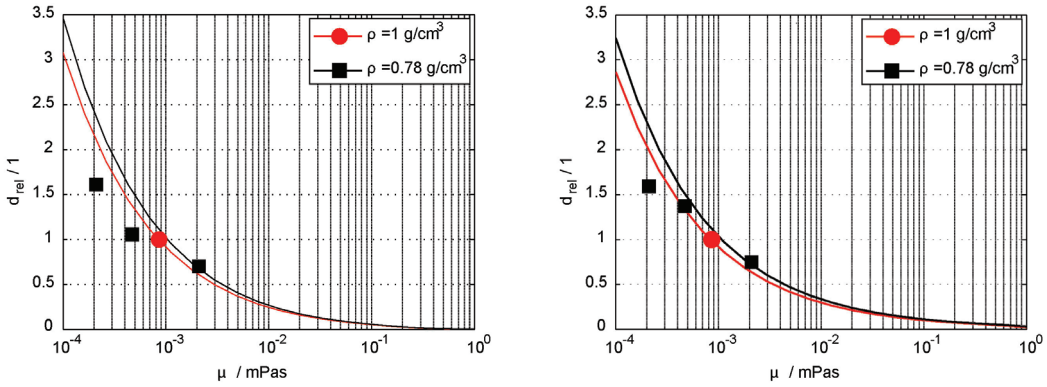

Fig. 5: Comparison between measured and theoretic data.

Conclusion and Outlook

Both of the presented principles seem to be well suited for measuring a liquid's viscosity in a large tunable range of resonance frequencies. Both principles show approximately the same sensitivity to viscosity as well as similar ranges of tunability. Thus, at this stage, it is hardly possible to meaningfully judge the benefits of one design over the other.

Regarding future work, we will comprehensively investigate the tunable range when varying both the normal stresses and the effective length of the vibrating mechanism. Furthermore, we will work on improving our setups for more reliable and accurate measurements as well on refining our analytical models to facilitate more accurate sensing.

Acknowledgements

We are indebted to the Austrian Competence Centre of Mechatronics (ACCM) for the financial support. We also want to thank Prof. Isabelle Dufour from Université de Bordeaux, Laboratoire de l'Intégration du Matériau au Système, France, for the very interesting and enriching discussions.

References

[1] M.Heinisch, E.K.Reichel, B.Jakoby: "A Suspended Plate In-Plane Resonator for Rheological Measurements at Tunable Frequencies", Proc. Sensor+Test, 2011, pp. 61-66.

[2] M.Heinisch, E.K.Reichel, B.Jakoby: "Miniaturized Resonating Viscometers Facilitating Measurements at Tunable Frequencies in the Low kHz-Range", Proc. Eurosensors, 2011, in print

Impedance Spectroscopic Measurements on Fluids in a Digital Microfluidic Platform

T. Lederer, S. Clara, B. Jakoby, W. Hilber

Johannes Kepler Universität, 4040 Linz, Austria

Digital microfluidics combines the advantages of low consumption of reagents with a high flexibility of processing fluid samples automatically. For applications in life sciences not only the processing but also the characterization of fluid analytes is crucial. In this contribution a microfluidic platform combining the actuation principle of electro wetting on dielectrics for droplet manipulations and the sensor principle of impedance spectroscopy for the characterization of fluid composition and condition is presented.

The fabrication process of the microfluidic platform comprises physical vapor deposition and structuring of the metal electrodes onto a substrate, the deposition of a dielectric isolator and a hydrophobic top coating.

The key advantage of this microfluidic chip is the common electric nature of the sensor and the actuation principle, so no additional sensor integration is necessary. Multiple measurements on fluids of different composition (including rigid particles and biologic cells) and of different conditions (temperature, sedimentation) were performed as well as online monitoring of in process parameters changing over time. These sample applications demonstrate the versatile applications of this combined technology.

A Microfluidic Chip for Infrared CH_2-stretch Ratio Measurements of Suspended Mammalian Cells

Ch. Haiden[1], S. van den Driesche[1], F. Iuliano[2], M.J. Vellekoop[1]

[1]Institute of Sensor and Actuator Systems, Vienna University of Technology, Vienna, Austria;
[2]Institute of Virology, Slovak Academy of Sciences, Bratislava, Slovak Republic

In this contribution we present a sensor system for measurements of the CH_2-stretch ratio of suspended mammalian cells. An infrared transparent CaF_2 microfluidic chip with three equal SU-8 structured sample chambers of 20 µm in height was fabricated. Cell samples were suspended in PBS (phosphate buffered saline) and introduced into the fluid chambers. The IR absorption of two epithelial kidney cell lines MDCK (Madin-Darby Canine Kidney) and Caki-1 was measured and we successfully distinguished normal MDCK from malignant Caki-1 by comparing their CH_2-stretch ratio.

Introduction

To increase the overall survival rate of cancer patients, an early detecting and accurate staging of primary tumours are highly important. While commonly used screening techniques are based on morphological features, e.g. visual inspection of suspicious tissue or cell samples after staining, these methods still result in a high number of false positives and negatives [1].

Previously, a four-wavelength mid-IR sensor system for measuring the CH_2-symmetric/ CH_2-antisymmetric stretch ratio of dried mammalian cell samples has been designed and realized as an alternative screening method. It was shown that the CH_2-stretch ratio is significantly increased for epithelial kidney carcinoma cells compared to the normal cell type [2].

Here we present a method for measurements of the CH_2-stretch ratio of suspended mammalian cells. Instead of the elaborate and time consuming preparation steps required for dried cell measurements to obtain a confluent cell monolayer attached to an infrared transparent CaF_2 slide, the cell sample is now suspended in PBS and directly introduced into an IR transparent sample chip.

Theory

Instead of recording the whole IR spectrum of cell samples with an IR spectrometer, the IR absorbance at only four specific wavelengths is measured with a sensor setup based on IR-LEDs, narrow bandpass filters and a photodiode detector. The IR absorbance at 3.33 µm and 3.57 µm is used for base-line correction, while the absorption peaks due to lipid CH_2-stretches in the cell membrane are located at the wavelengths 3.42 µm (CH_2-antisymmetric stretch) and 3.51 µm (CH_2-symmetric stretch). The base-line corrected absorbance at 3.42 µm and 3.51 µm is used to calculate the CH_2-symmetric/CH_2-antisymmetric stretch ratio of a cell sample (Fig. 1).

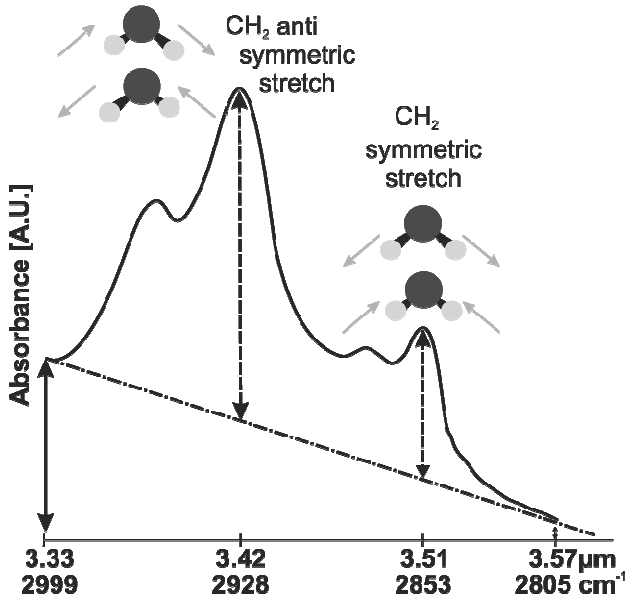

Fig. 1: Illustration of the cell type discrimination method. The infrared absorbance at four specific wavelengths is measured and the baseline corrected absorbance at 3.42 µm and 3.51 µm is used to derive the CH_2-stretch ratio.

This CH_2-stretch ratio of mammalian cells increases when the concentration of membrane stabilizing agents such as cholesterol in the plasma membrane decreases or is reallocated. This stretch ratio increase was shown for MDCK epithelial kidney cells exposed to the cholesterol reducing agent methyl-β-cyclo-dextrin [3].

Experimental

Chip Fabrication

To allow for CH_2-stretch ratio measurements of cell samples in suspension a microfluidic chip was designed and realized. The chip consists of two bonded 1 mm thick infrared transparent CaF_2 wafers with 20 µm high SU-8 chamber structures in between. With this chamber height the strong infrared absorbance of water can be reduced while an even distribution of approximately 15 µm large epithelial kidney cells throughout the sample chamber is guaranteed. A sample chip consists of three chambers, each with a diameter of 3.5 mm allowing multiple 1.5 mm diameter spots to be measured and a volume of about 0.3 µL.

The in-house fabrication consisted of the following steps (Fig. 2): SU-8 50 was spun on the cleaned top and bottom CaF_2 wafers and UV-exposed such that unexposed SU-8 was still enclosed by exposed SU-8 (Fig. 2 (a) – (b)). Then a copper layer was deposited on it and patterned (Fig. 2 (c) – (d)). SU-8 which was not protected by the metal layer was removed with developer to form the chamber structures on both wafers (Fig. 2 (e)) before the Cu layer was etched away (Fig. 2 (f)). Eventually, inlet and outlet holes of 600 µm diameter were drilled in the bottom wafer before the wafers were aligned and bonded (Fig. 2 (g) – (h)). The soft, thermoplastic SU-8 from the top wafer filled the gaps by capillary forces when heated during wafer bonding. At 150 – 200 °C, unexposed SU-8 is thermally cross-linked, serving as an adhesive layer between the

wafers in order to increase bonding strength [4]. Dicing of the wafer yielded single chips as shown in Fig. 3.

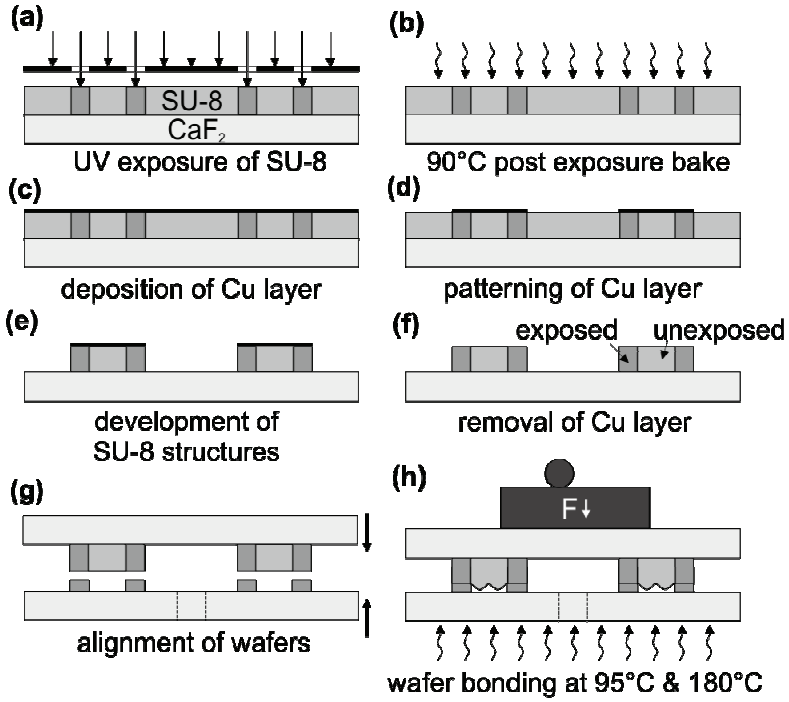

Fig. 2: Patterning of SU-8 on bottom and top wafer to form fluidic chamber structures comprising unexposed SU-8 enclosed by UV-exposed SU-8 sidewalls ((a) – (f)), followed by wafer bonding and thermal cross-linking of unexposed SU-8 ((g) – (h)).

Fig. 3: Photograph of the 11x15x2 mm³ microfluidic sample chip. Each chip consists of three sample chambers of 3.5 mm diameter and a volume of about 0.3 µL.

Suspended Cell Measurements

Two MDCK and two Caki-1 cell samples were investigated in order to measure and compare their CH_2-stretch ratios in suspension. Of each cell line two different cell generations (cell passages) were prepared. Cells were removed from the culture flask by

means of trypsination, washed with PBS two times, and resuspended in PBS. Before cell sample measurements, chambers were filled with PBS and the IR absorbance was recorded as reference. Consequently, the PBS was removed and cell suspension was filled into the chambers (Fig. 4). The time between subsequent measurements of both normal MDCK and malignant Caki-1 samples was approximately five weeks. Of each sample five spots were measured.

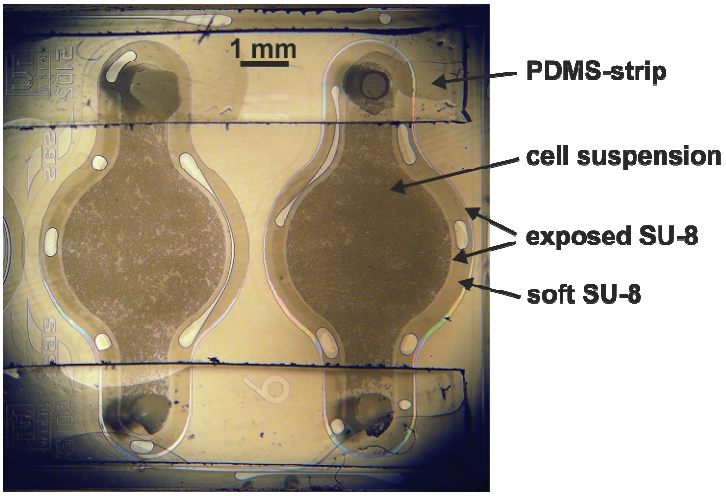

Fig. 4: Two sample chambers containing mammalian cells suspended in PBS. The inlets and outlets were sealed with PDMS strips to avoid evaporation.

Each bar in Fig. 5 represents the average value of the CH_2-stretch ratio and standard deviation of all spots recorded for one of the four samples. The MDCK cell samples yielded a CH_2-stretch ratio of 0.45 ± 0.01 and 0.44 ± 0.01, respectively. Malignant Caki-1 showed CH_2-stretch ratios of 0.49 ± 0.01 and 0.48 ± 0.01.

Compared to previously conducted CH_2-stretch ratio measurements on dried samples, suspended cell measurements all yielded lower stretch ratio values due to changes in the protein hydration levels [5].

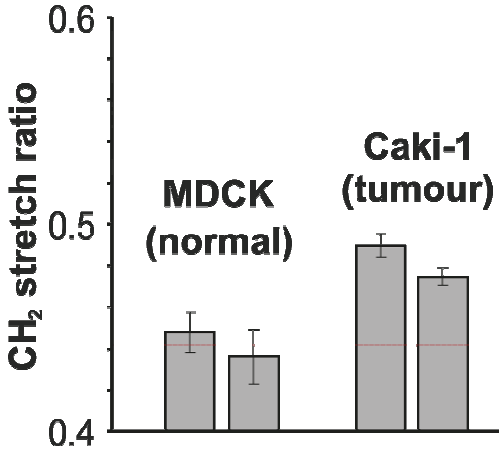

Fig. 5: Two MDCK and Caki-1 cell samples were measured. Each bar represents the average value and standard deviation of the CH_2-stretch ratio of multiple spots.

Conclusions

Suspended viable cell measurements offer much shorter preparation times (≈ 1/2 hour) compared to dried cells. The measurement results show the feasibility to distinguish normal (MDCK) from tumor (Caki-1) epithelial kidney cell lines. Furthermore, a miniaturization of the sensor system could enable the realization of devices for point-of-care diagnostics, since the CH_2-stretch ratio is a promising indicator for the detection of tumor cells.

Acknowledgements

This project is a part of the EU Marie Curie Research Training Network (MRTN) On-Chip Cell Handling and Analysis: CellCheck. Project no. MRTN-CT-2006-035854. We would like to thank A. Jachimowicz, E. Svasek and P. Svasek from the Sensor Technology Lab at ISAS and the Center for Micro- and Nanostructures (ZMNS), TU Vienna.

References

[1] M. H. Stoler and M. Schiffman: “Interobserver reproducibility of cervical cytologic and histologic interpretations: realistic estimates from the ASCUS-LSIL Triage Study”, J. Am. Med. Assoc., 258, 2001, pp. 1500-1505.

[2] S. van den Driesche, W. Witarski, S. Pastorekova and M. Vellekoop: “A quadruple wavelength IR sensor system for label-free tumour screening “, Meas. Sci. Technol., 20, 2009, pp. 124015.

[3] S. van den Driesche, W. Witarski, S. Pastorekova, H. Breiteneder, Ch. Hafner and M. Vellekoop: “A label-free indicator for tumor cells based on the CH_2-stretch ratio”, Analyst, 136, 2011, pp. 2397-2402.

[4] P. Svasek, E. Svasek, B. Lendl and M. Vellekoop: “Fabrication of miniaturized fluidic devices using SU-8 based lithography and low temperature wafer bonding”, Sens. Actuators A, 115, 2004, pp. 591-599.

[5] A. Pevsner and M. Diem: “Infrared Spectroscopic Studies of Major Cellular Components. Part I: The Effect of Hydration on the Spectra of Proteins”, Appl. Spectrosc., 55, 2001, pp. 788-793.

Cell Separation in a Continuous Flow by Traveling Wave Dielectrophoresis

D. Puchberger-Enengl[1], S. van den Driesche[1], V. Rao[1], W. Witarski[2], M.J. Vellekoop[1]

[1]Institute of Sensor and Actuator Systems, Vienna University of Technology, 1040 Vienna, Austria
[2]Institute of Virology, Slovak Academy of Sciences, 84245 Bratislava, Slovak Republic

In this contribution we present a microfluidic chip for the continuous and label-free separation of cells. Strip electrodes produce a traveling electric field perpendicular to the pressure driven flow. Viable cells are deflected parallel to the field by traveling wave dielectrophoresis (twDEP) according to their volume and dielectric properties. With the present device we have successfully separated viable *Saccharomyces cerevisiae* and *Jurkat* T-cells from debris, non-viable cells *and Lactobacillus casei*.

Introduction

Common techniques to separate suspension-grown cells, such as Fluorescent Activated Cell Sorting (FACS), require elaborate protocols and equipment. Dielectrophoresis (DEP) has widely been applied for the label-free separation of particles and biological cells [1]. Traveling wave dielectrophoresis is the linear motion of particles and cells induced by a traveling electric field that is produced by multi-phase excited microelectrodes (Fig. 1). In contrast to conventional dielectrophoresis, twDEP does not require a nonuniform electric field. Therefore, the force does not decay with distance and cells can be moved with a better efficiency [2]. The force on a particle in a traveling electric field is given by

$$\vec{F}_{twDEP} = -\frac{4\pi^2 r^3 \varepsilon_m}{\lambda} \Im\{K(\omega)\} E^2_{rms} \tag{1}$$

where r is the particle radius, ε_m the medium permittivity, E the field magnitude, λ the electrode distance and $\Im\{K(\omega)\}$ the imaginary part of the Clausius-Mosotti factor.

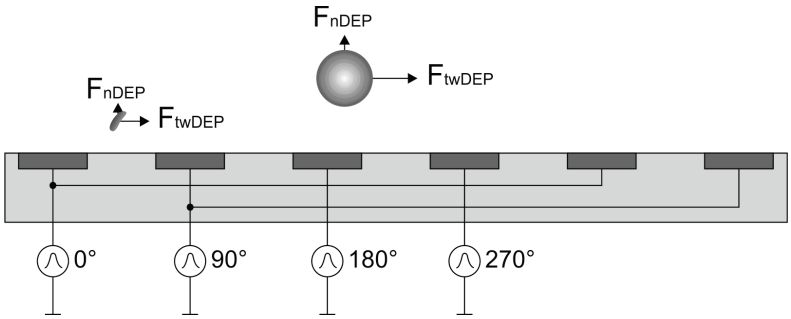

Fig.1: Forces on suspended cells of different size exposed to a traveling field. The cells are levitated by negative Dielectrophoresis ($\Re\{K(\omega)\} < 0$) and propelled across the electrodes according to the imaginary part of the Clausius-Mosotti $\Im\{K(\omega)\}$ [3].

Materials and Methods

The medium for cell experiments consisted of 10% (w/w) sucrose (Sigma S9378) and 2% (w/w) dextrose (Sigma D9559) in deionized water. The conductivity was set to 40 mS/m by adding PBS. *Jurkat* T-lymphocytes were cultivated at 37 °C in a DMEM medium containing 4.5 g/l glucose, 2 mM L-glutamine, 10% fetal calf serum and antibiotics (100 units/ml penicillin, 100 µg/ml streptomycin and 0.25 µg/ml amphotericin B). Baker's yeast (*Saccharomyces cerevisiae*) was obtained fresh from a supermarket. Contaminated samples were prepared by adding *L. casei* bacteria (DSM20011) to the cells in suspension. Prior the experiments the cells were washed twice and resuspended in DEP medium.

The fabricated chip and its operation principle are illustrated in Fig. 2. A set of parallel platinum electrodes of 20 µm width and gap size was fabricated on a glass wafer by a lift-off process. Holes for fluidic access were drilled through the glass substrate. The 200 µm wide and 30 µm high channel was fabricated by soft-lithography in PDMS and placed on top of the electrodes.

For the continuous experiments the cell samples are introduced into the chip by a syringe pump (KD Scientific 210P). A sheath flow from the second inlet is used to focus the cells to one side of the channel (Fig. 2). Two signal generators (Agilent 33220A) and broadband transducers are utilized to produce the decoupled and phase-shifted excitation voltage. According to the chosen frequency of the traveling field the target cells are dragged across the channel and leave the device separated from contamination and debris.

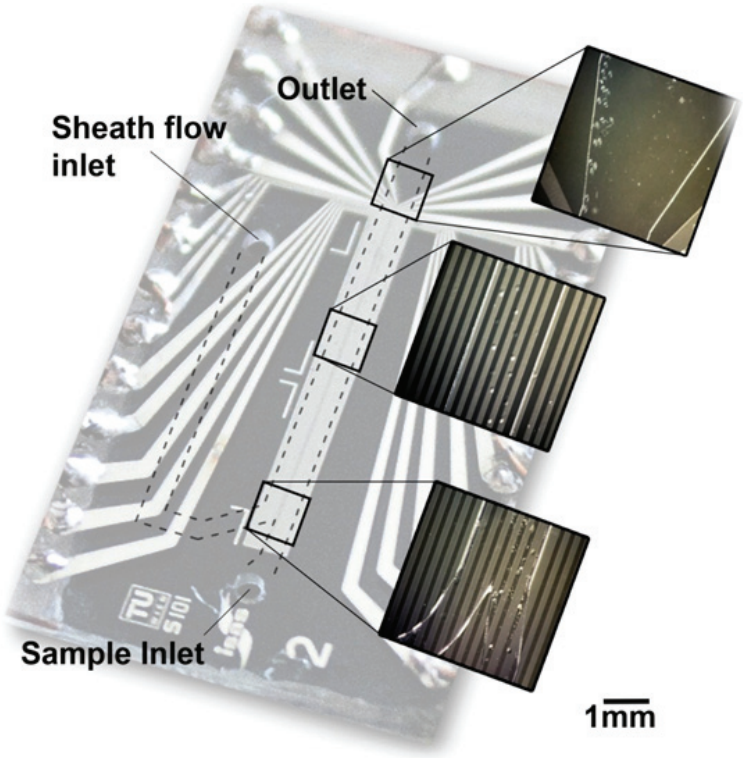

Fig. 2: Separation chip: The sample stream is focused to one side and target cells are moved across the electrodes towards the channel wall.

Results and Discussion

To determine the optimal frequency for cell-cell separation the imaginary parts of the Clausius-Mosotti factor $\Im\{K(\omega)\}$ of the three cell types were evaluated by electrorotation (ROT).

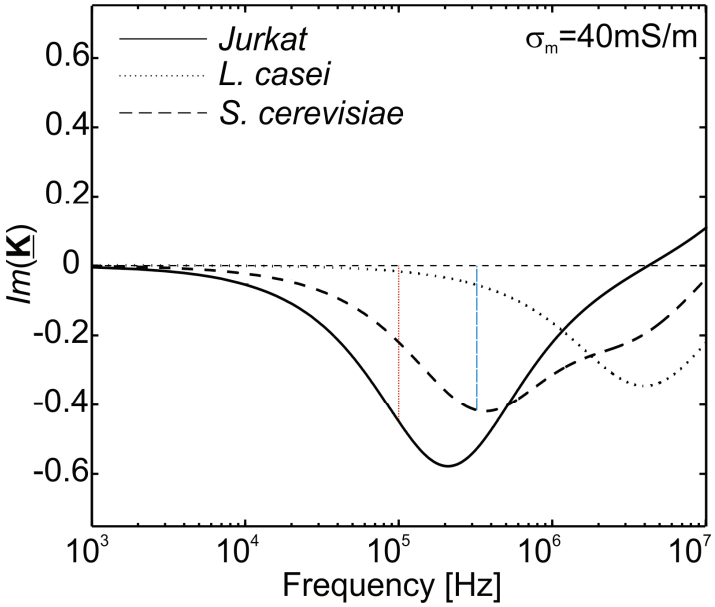

Fig. 3: Imaginary parts of Clausius-Mosotti factor of *Jurkat* T-cells (~14µm), *Saccharomyces cerevisiae* (~5µm) and *L. casei* (~1x3µm).

A quadruple electrode configuration was used to measure cell rotations per second with varying frequency. Cell models with multiple shells, representing the cytoplasm, cell membrane and cell wall, were fitted to the experimental data [4]. The modeled frequency responses of $\Im\{K(\omega)\}$ for the used cell types are plotted in Fig. 3. The vertical lines indicate the frequencies used for separation experiments. According to Eq.1 the differences of $\Im\{K(\omega)\}$ at these frequencies in combination with the distinct cell radii suggest a great difference of the resulting twDEP force and enable efficient separation.

Results of the separation experiments are illustrated by cell counts at the chip outlet shown in Fig. 4. The cell samples were introduced with a flow rate of 0.1 µl/min and focused by a sheath flow of 0.15 µl/min. Without an applied voltage the cells left the device as they were introduced, only on one side of the channel (DEP off diagrams in Fig. 4). After applying a voltage, viable cells were forced towards the other side of the channel. Non-viable cells did not experience a twDEP force due to disruption of the cell membrane. Furthermore, the *L. casei* bacteria were not affected by traveling wave DEP and left the device at local field minima above the electrodes in the range of 0 – 100 µm. Altogether 86.5% of the *Jurkat* cells were found in the 170 to 200 µm region. This percentage corresponds to a viability test with trypan blue staining prior the experiments that revealed a cell viability of 90%. In experiments with yeast 87% left the channel in the 185 to 200 µm region. Unaffected cells left at the local field minimum above the first electrode, suggesting to decrease the electrode width for smaller cells.

Conclusion

Traveling wave dielectrophoresis has been shown to yield an efficient, label-free purification of biological cells from a contaminated sample solution. Only rough sample fo-

cusing is required and the separation is robust against flow rate fluctuations. Besides separation the presented device also enables viability studies since only cells with intact membranes are affected by the twDEP force.

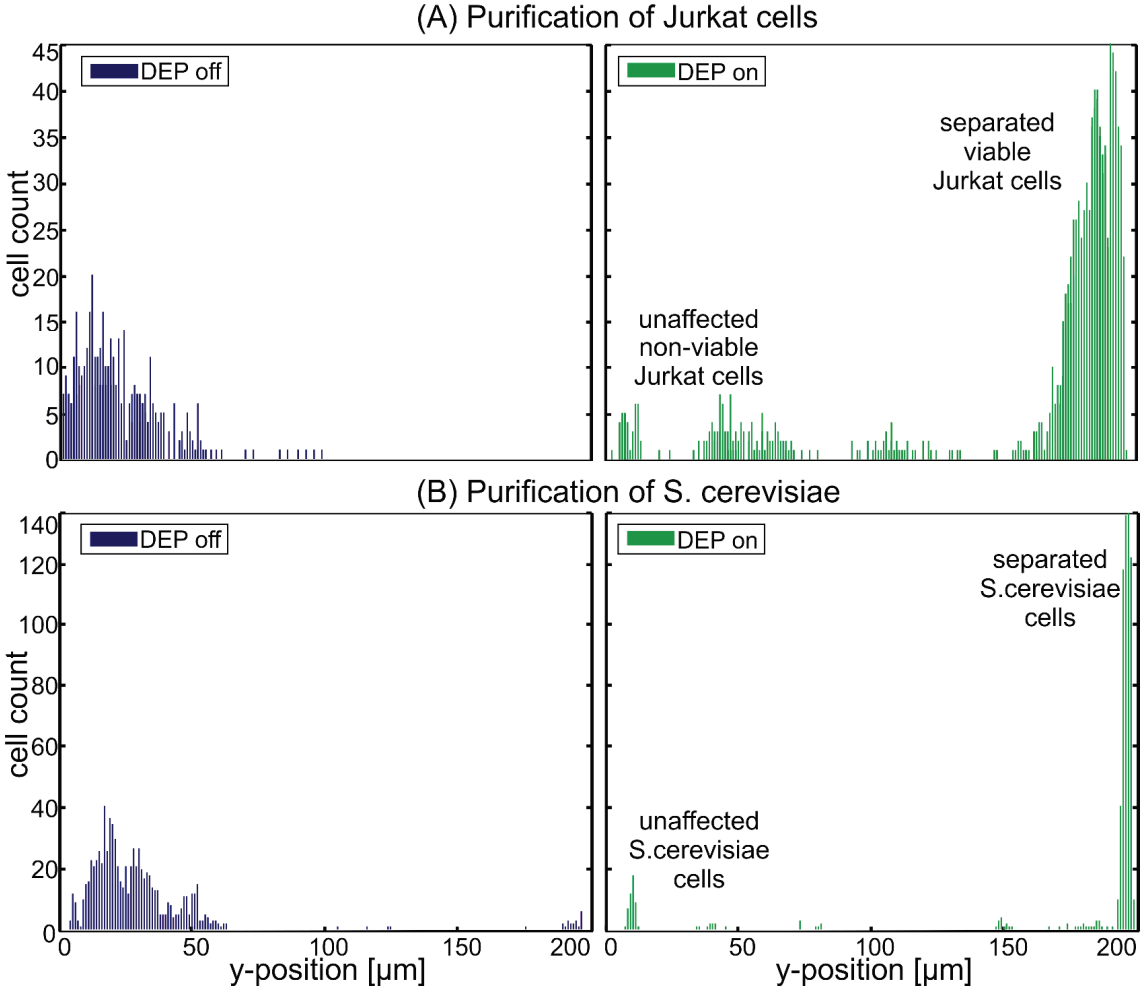

Fig. 4: Histograms of the separation results (total flow rate 0.25 µL/min, medium conductivity 40 mS/m). (A): Viable *Jurkat* cells separated from cell culture debris containing non-viable cells and *L. casei* (voltage 3.5 Vrms, 100 kHz). (B): *S. cerevisiae* cells separated from cell culture debris containing non-viable cells and *L. casei* bacteria (voltage 5 Vrms, 350 kHz).

Acknowledgements

This project is part of a joint EU Marie Curie Research Training Network (MCRTN) "On-Chip Cell Handling and Analysis" – Cellcheck; Project no. MRTN-CT-2006-035854; http://www.cellcheck.eu

References

[1] R. Pethig: "Review Article-Dielectrophoresis: Status of the theory, technology, and applications", Biomicrofluidics, 2010 Jun 29;4 (2)

[2] S. van den Driesche, V. Rao, D. Puchberger-Enengl, W. Witarski, M. J. Vellekoop: “Continuous cell from cell separation by traveling wave dielectrophoresis”, Sensors and Actuators B: Chemical, 2011, Article in Press

[3] T. B. Jones: “Basic Theory of Dielectrophoresis and Electrorotation” IEEE Eng Med Biol Mag. 2003 Nov-Dec;22(6): 33-42

[4] P. Gascoyne, F.F. Becker, X.-B. Wang: “Numerical analysis of the influence of experimental conditions on the accuracy of dielectric parameters derived from electrorotation measurements”, Bioelectrochemistry and Bioenergetics, Vol. 36, 2, 1995, 115-125

An Imaging Platform for Mammalian Cell Migration Monitoring

N. Moscelli[1], W. Witarski[2], S. van den Driesche[1], M.J. Vellekoop[1]

[1]Institute of Sensor and Actuator Systems, Vienna University of Technology, 1040 Vienna, Austria
[2]Institute of Virology, Slovak Academy of Sciences, 84245 Bratislava, Slovak Republic

Here we present an imaging platform that operates in standard lab incubators for the real-time investigation of multiple cell cultures in disposable multi-well plates. The system consists of four CCD (Charge-Coupled Devices) image sensors built into a custom-made holder, in which the multi-well plate is fixed. Above the multi-well plate, white light emitting LEDs provide vertical illumination on the cell samples and the sensors. The system allows simultaneous motility measurements of individual adherently grown cells over four wells, enabling high throughput and the extraction of statistically relevant biological data. In order to test it, we have monitored stimulated (with Hepatocyte Growth Factor) and control samples of MDCK (Madin-Darby Canine Kidney) cells.

Introduction

For the understanding of tumor progression, cell migration studies are of great importance [1]. Normally, optical cell investigation is carried out by microscopy. Nevertheless, in order to preserve optimal mammalian cell cultivation conditions (37 °C, 5% CO_2 concentration, high humidity level), the only alternative to time-lapse observations out of the incubator is to provide optical microscopes with expensive additional incubation stages for temperature and carbon dioxide control [2]. This way, real-time cell monitoring is achieved. In this work we present a compact and cost-effective alternative to conventional optical microscopy: it operates in standard lab incubators and it operates on multiple in-vitro assays from conventional multi-well plates. In a previous work, we have demonstrated that our system can successfully detect individual and aggregated adherent cells [3]. In this contribution, we prove that our system can simultaneously monitor multiple cell samples in real-time, enabling the extraction of statistically relevant biological parameters. The imaging platform was tested by observing HGF-stimulated (Hepatocyte Growth Factor) and control samples of MDCK (Madin-Darby Canine Kidney) cells and therefore extracting typical migration parameters, such as trajectories and mean cell velocities.

Sensor System

In Fig. 1, the setup of the mammalian cell imaging platform is depicted. The illumination is provided by vertically-aligned white light emitting LEDs, placed above the cell samples and the image sensors. The 10° focused radiation beam is further collimated by 8 mm diameter-apertures. Four CCD image sensors (VGA frame format, 640 x 480 pixels, 5.6 x 5.6 μm^2 pixel size) achieve near-field focusing by employing mini lenses featuring *f* 2.0 and 4.3 mm focal length. The distance between the sensor array and the mini lens was adjusted in order to position the focal plane exactly on the substrate of the well under investigation. In order to withstand the incubation conditions, the sen-

sors and the electronics have been protected by possible humidity condensation by hermetically sealing them with insulating polymeric films and tapes.

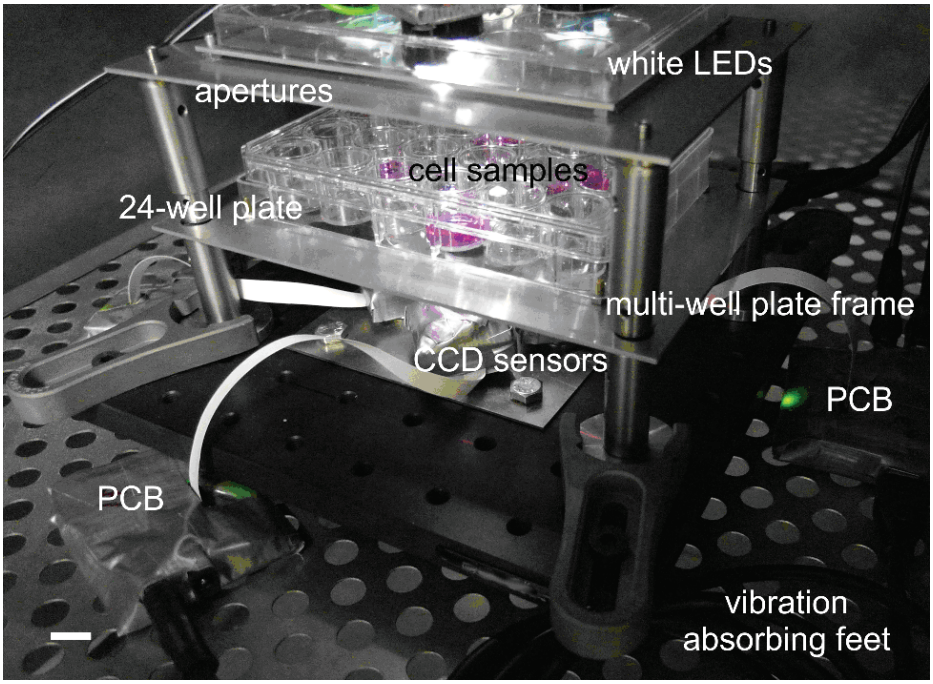

Fig. 1: The imaging platform setup for mammalian cell monitoring placed in a conventional lab incubator with a standard 24-well plate (well diameter: 16 mm).

Experimental

Sample Preparation

Four MDCK cell colonies (ATCC CCL-34) have been seeded in four different wells of a disposable 24-well plate (Greiner Bio-One GmbH, Germany) and incubated in standard conditions (37 °C, 5% CO_2, and high humidity level). The cells have been cultivated in DMEM (Dulbecco's Modified Eagle Medium), 4.5 g/L glucose, 2 mM glutamine, 10% FCS (Fetal Calf Serum) and antibiotics. After 12 hours incubation, all cell samples have been set to starvation with a medium containing 0.5% FCS.

Measurements

In order to test the imaging platform, cell motility experiments have been simultaneously carried out on four MDCK cell colonies. Two of them have been supplemented with HGF in a concentration of 20 ng/mL, while the remaining two cell samples have been left without any stimulation to investigate differences in cell activity. In mammalian organisms, HGF has a major role in embryonic organ development, in adult organ regeneration and in wound healing. Thus, a marked cell motility promotion is expected in the exposed cell colonies. The cell samples have been grown all as described above. After cell sedimentation and adhesion to the bottom of the wells, we have recorded cell activity of each population for 8 hours. The frames have been recorded every 3 minutes from the four sensors. Magnified portions of the acquired frames showing stimulated individual MDCK cells are shown in Fig. 2. To determine the individual cell motility, the *xy* coordinates of each cell in consecutive frames have been semi-automatically

tracked using ImageJ (NIH, USA). From the extracted coordinates, the cell trajectories have been derived in terms of Euclidean distance between two points. Four samples of stimulated and control cell migration trajectories are shown in Fig. 3. The difference in terms of covered paths between stimulated and non-stimulated cells is clearly visible. The distances covered by the monitored cells have been then used to calculate the mean velocity of *n* cells of the same population [4]. This parameter statistically quantifies the effects of drug exposure on cell motility.

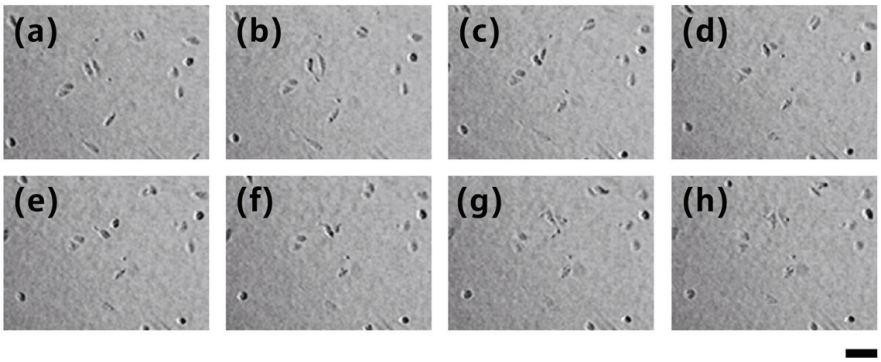

Fig. 2: Frames showing individual HGF-stimulated MDCK cells. Scale bar: 100 µm.

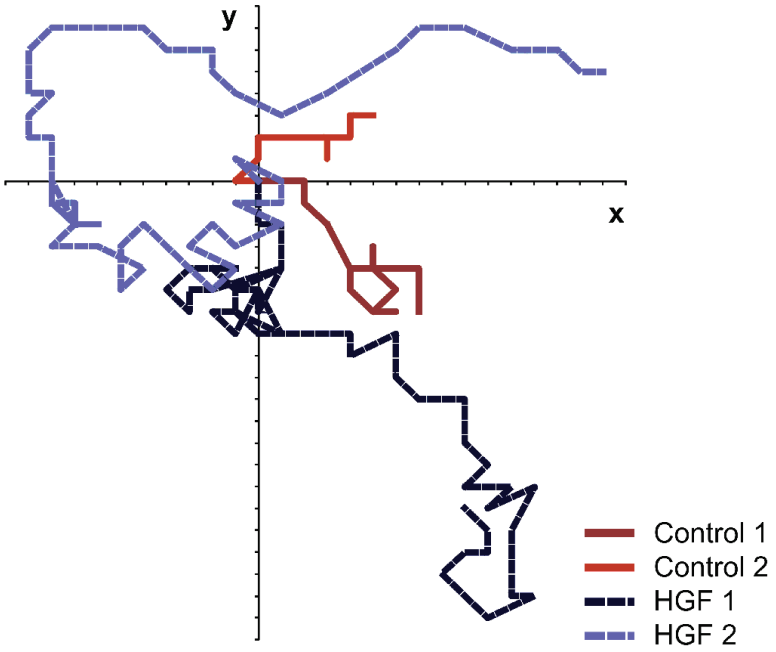

Fig. 3: Individual cell motility plot. The trajectories of HGF-stimulated and control cells are compared over a period of 8 hours.

By tracking and analyzing a population of 10 cells per each of the four colonies, we have extracted the mean cell velocity of stimulated and control cell populations, as shown in Fig. 4. From the plot it is possible to clearly observe that stimulated cell migration results in a mean cell velocity higher than 40 µm/h: approximately 4 times the mean cell velocity of the control samples. These results are in good agreement with the average velocities derived from the cell trajectories shown in Fig. 3.

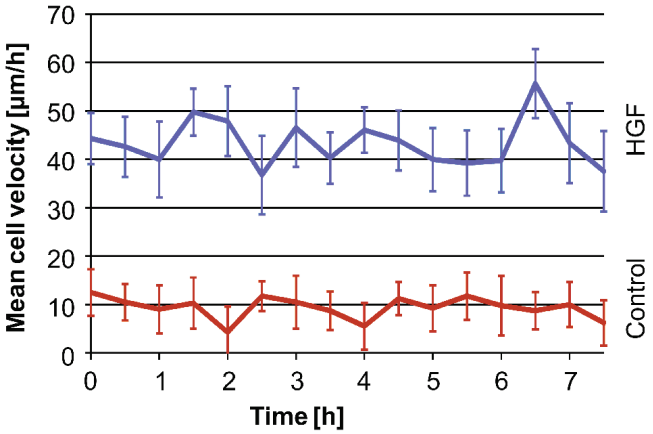

Fig. 4: Mean cell velocity in time. A significant change in the motility of the stimulated cells can be observed after half an hour; after 1 hour, the mean cell velocity reaches its maximum. Error bars: standard deviation.

Conclusions

We have realized, characterized and experimentally tested a live cell imaging platform for the real-time investigation of individual cell motility. The obtained results show that with our live cell monitoring platform we are able to successfully extract and measure every cell motility parameter. Furthermore, the compatibility with lab disposables and standard lab incubators and the ability to simultaneously track up to four biological samples in different conditions make our system attractive to achieve statistically relevant measurements.

Acknowledgements

This project is a part of the EU Marie Curie Research Training Network (MRTN) CellCheck “On-Chip Cell Handling and Analysis”, Project No. MRTN-CT-2006-035854. The authors gratefully acknowledge Filippo Iuliano of the Institute of Virology of the Slovak Academy of Sciences in Bratislava for his valuable help during the early testing phase of the device. They also thank Ewald Pirker of the Institute of Sensor and Actuator Systems, Vienna University of Technology, for fabricating the platform holder.

References

[1] S. Suresh: “Biomechanics and biophysics of cancer cells”, Acta Biomater, Vol. 3, 2007, pp. 413 – 438

[2] M. Poujade, E. Grasland-Mongrain, A. Hertzog, J. Jouanneau, P. Chavrier, B. Ladoux, A. Buguin, P. Silberzan: “Collective migration of an epithelial monolayer in response to a model wound”, PNAS, Vol. 104, 2007, pp. 15988 – 15993

[3] N. Moscelli, S. van den Driesche, W. Witarski, S. Pastorekova, M.J. Vellekoop: “An imaging system for real-time monitoring of adherently grown cells”, Sens Act A Phys, accepted for publication, doi: 10.1016/j.sna.2011.05.010

[4] R. Hartmann-Petersen, P.S. Walmod, A. Berezin, V. Berezin, E. Bock: “Individual cell motility studied by time-lapse video recording: influence of experimental conditions”, Cyt A, Vol. 40, 2000, pp. 260 – 270

Diagnostic Polymer Disc for Process Speed-Up in Microarray-based Bacterial Classification

J.R. Peham[1], L. Recnik[1], W. Grienauer[2], M.J. Vellekoop[3], C. Nöhammer[1], H. Wiesinger-Mayr[1]

[1]Austrian Institute of Technology, Health & Environment Department, 1190 Wien, Austria
[2]Aerospace and Advanced Composites GmbH, 2444 Seibersdorf, Austria
[3]Institute of Sensor and Actuator Systems, Vienna University of Technology, 1040 Wien, Austria

We present an injection molded microfluidic polymer disc enabling DNA amplification and fluorescent labeling within one step. The device is ready for large-lot production and biocompatible. The fluorescently labeled product generated in our flow-through reaction device can be directly hybridized onto microarrays to classify bacterial species. Combining DNA amplification with labeling and the application of a continuous-flow polymerase chain reaction reduced the overall microarray processing time by a factor of four. DNA amounts equivalent to 100 cells per reaction could be detected, which validates this polymer disc as a sensitive and rapid assay for bacterial classification.

Introduction

Infectious diseases are a major health threat including diseases like sepsis, pulmonary tract infections and meningitis. The most effective therapy is still early treatment, which requires early and fast diagnosis. In addition the causative bacterial species are rarely identified prior to initiation of therapy, which decreases treatment efficiency and promotes a further increase in antibiotic resistances. Therefore a rapid assay for species-specific identification is of great importance for a targeted therapy, a most effective patient convalescence and for confining drug resistances of pathogens.

While culturing of the specimen is still the gold standard, it is time-consuming and can last up to days for slowly growing bacterial species. More rapid assays are often implemented with molecular methods like quantitative polymerase chain reaction (qPCR) or DNA microarray technology. They have a clear time advantage and reduce analysis time from days to hours. For example DNA microarray analysis of 65 different pathogens can be performed within 6 hours [1].

A typical microarray workflow consists of DNA amplification by PCR, fluorescence DNA labeling by linear PCR (forward primer only), microarray hybridization and signal read-out, including statistical analysis (Fig. 1). In the workflow, PCR and labeling account for over 80% of the overall processing time and are therefore the processes which are accelerated with the presented microfluidic device. Applying our newly developed polymer disc, we can reduce processing and hands-on time and increase process automation. Rapid diagnosis of bacterial pathogens is therefore possible, which can very much improve therapy success.

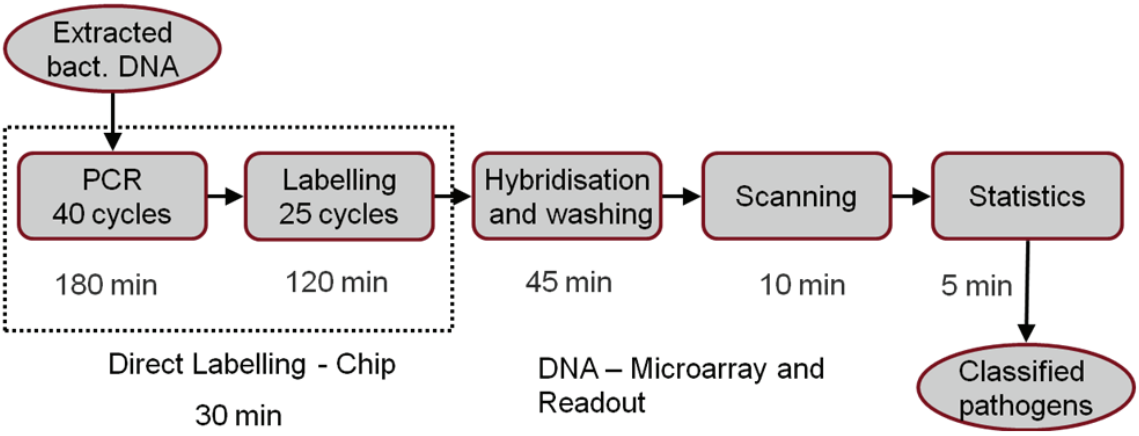

Fig. 1: DNA microarray workflow: The polymer device replaces the conventional and time-consuming PCR- and labeling step in the protocol, resulting in an overall 4-fold process speed-up

Design and Fabrication

The newly developed polycarbonate chip is designed to transform low amounts of bacterial DNA into fluorescently labeled amplicons, ready for microarray hybridization. This is performed in a spiral microfluidic channel with 40 turns and two meanders for predenaturation and post-annealing respectively (Fig. 2).

The chip was fabricated by injection molding, which makes it suitable for mass production, essential for a disposable device. The channels are 290 µm wide and the rims between are 150 µm. To achieve a constant volume per turn the channel depth decreases with increasing radius (from 597 µm to 175 µm). To seal the channels a polycarbonate film (125 µm) was thermally bonded to the injection molded substrate.

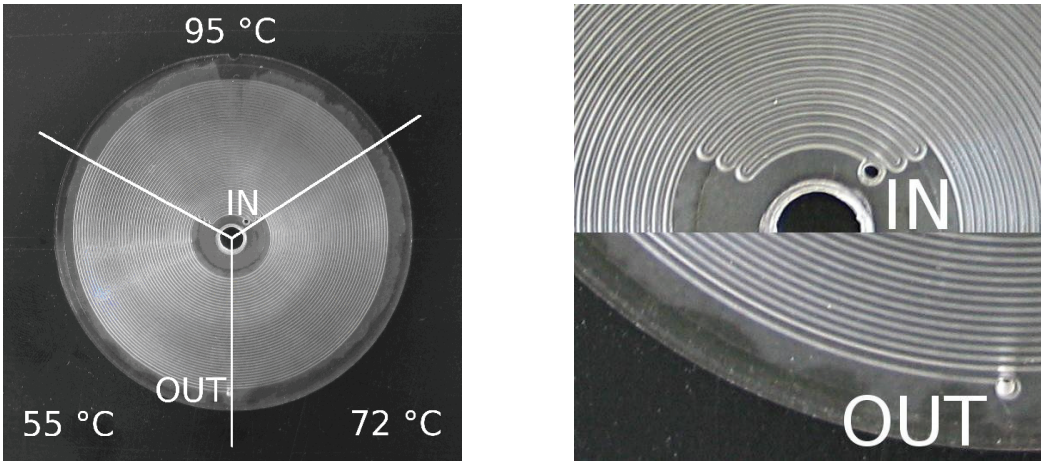

(a) (b)

Fig. 2: Chip design: (a) top view with the three temperature zones, (b) detail of predenaturation meander with inlet (top) and post-extension meander with outlet (bottom)

The whole chip is tempered with three symmetric external heating sectors for denaturation (95 °C), annealing (55 °C) and extension (72 °C) (Fig. 2). When the samples are

pumped through the spiral, they undergo a polymerase chain reaction (PCR) protocol. Cy3-conjugated primers are used for direct labeling the DNA within the PCR. All processed samples are interspaced with silicone oil as transport buffer. Before the reaction the sample sequence is aspirated in a loading column as described before [2].

Results

The fabricated polycarbonate disc was compatible to all biological samples and reagents. No adhesion of polymerases or nucleotides was observed, which would have resulted in significant efficiency loss. However it was crucial, that bovine serum albumin was included in the used PCR mastermix, as presented before [2]. In addition the transport buffer did not affect the polycarbonate material or the bonding interface.

The disc itself showed high quality, where channels were molded correctly and there was no major deviation of the desired geometry. The sealing with the polycarbonate film was successful and no cross-talk between channels was observed (Fig. 3). In the experiments the bonding withstood the used flow rates of 111 $nl.s^{-1}$. Therefore the fabrication technologies are appropriate for large-scale production, which is important for the application as a disposable device. The thermal distribution across the polycarbonate disc showed deviations of maximal 1.5 °C in the outer regions, which was appropriate for fast transitions between the temperature stages.

The chip was tested with *Staphylococcus aureus* and lead to a sensitivity of 100 cells per reaction, which qualifies the system for clinical applications. The direct comparison of microarray results using our new disc chip and the standard method showed lower signal intensities for PCR amplicons synthesized by the chip. Although the absolute signals were lower, the correct bacterial species could be classified (Fig. 4).

Performing the reaction in the microfluidic disc showed a 10-fold acceleration of PCR and labelling (Fig. 1), because of absent ramping times between temperature stages, which limit the speed in conventional thermocyclers. This resulted in a decrease of the total processing time for microarray analysis from 6 h to 1.5 h.

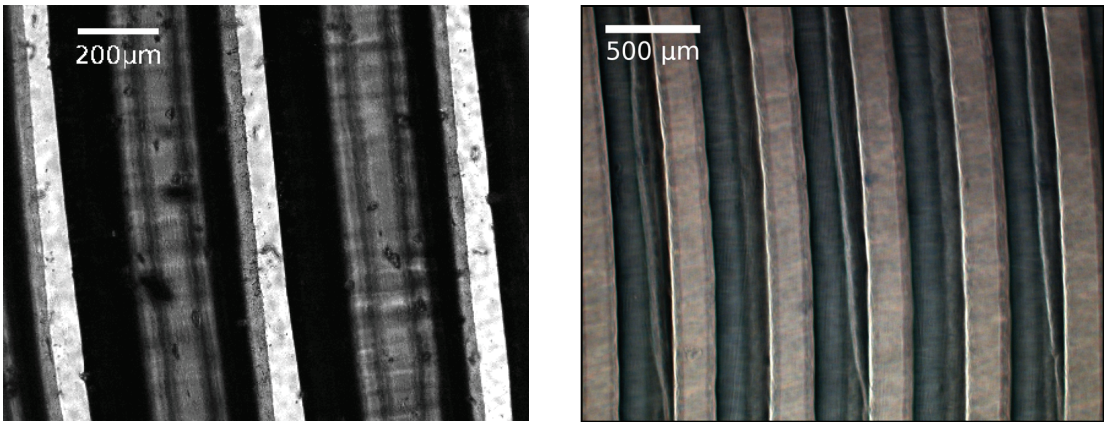

(a) (b)

Fig. 3: Sealing of channels: (a) empty channels, bright parts represent the bonding interface between rims and film; (b) channels filled with methylene blue stained water for testing the tightness of the chip

Conclusion

The combination of DNA amplification and fluorescence labeling in a one-step approach reduced hands-on time and increased process automation. We have overcome the limit of analysis time for microarrays by accelerating the overall process 4-fold, resulting now in a processing time of only 1.5 h. The fabricated disc is biocompatible and the production technique is capable for mass production. Therefore our diagnostic disc device enables very rapid identification of pathogen species in a disposable assay format.

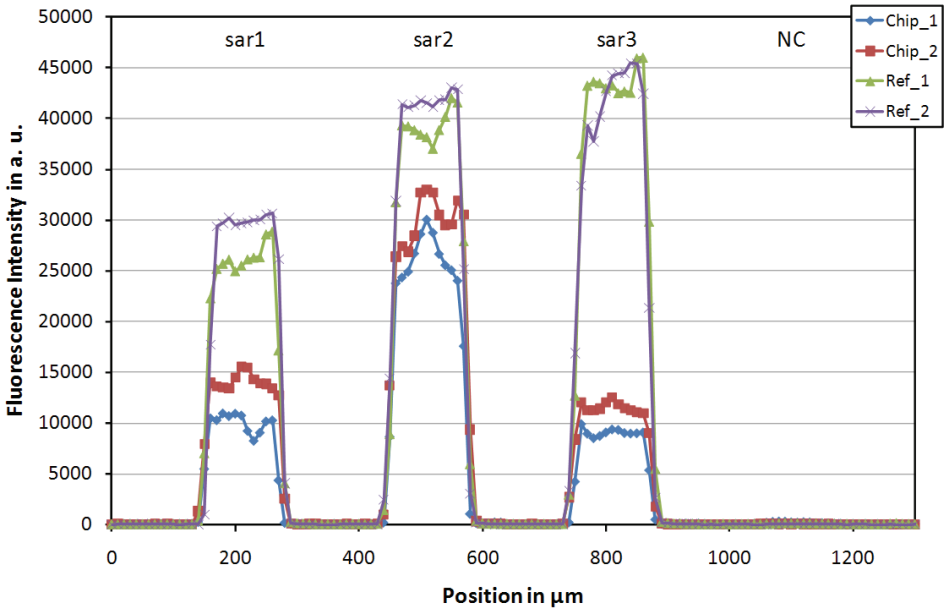

Fig. 4: Line-plots of scanned microarray slides: The output of the polymer disc (Chip_1, Chip_2) is compared to the standard method (Ref_1, Ref_2). Although the absolute signals from the chip were lower, the bacterial species could be classified correctly; sar1-3: species specific DNA probes for *Staphylococcus aureus*.

Acknowledgements

The authors gratefully acknowledge Silvia Schönthaler for the expert technical assistance.

References

[1] H. Wiesinger-Mayr, K. Vierlinger, R. Pichler, A. Kriegner, A. M. Hirschl, E. Presterl, L. Bodrossy, C. Nöhammer: " Identification of human pathogens isolated from blood using microarray hybridisation and signal pattern recognition", BMC Microbiol, Vol. 7, 2007, pp. 1-17.

[2] J. R. Peham, W. Grienauer, H. Steiner, R. Heer, M. J. Vellekoop, C. Nöhammer, H. Wiesinger-Mayr: " Long target droplet polymerase chain reaction with a microfluidic device for high-throughput detection of pathogenic bacteria at clinical sensitivity", Biomed Microdevices, Vol. 13, 2011, pp. 463-473.

Analytical, Numerical and Experimental Analysis of Capacitive Transducers Damping Constant

M. Sachse[1], M. Stifter[1], W. Hortschitz[1], F. Keplinger[2]

[1]Institute for Integrated Sensor Systems, Austrian Academie of Sciences, Wr. Neustadt, Austria
[2]Institute of Sensor and Actuator Systems, Vienna University of Technology, Vienna, Austria

Designing a tailored transducer for specific applications needs the knowledge of mechanical system parameters like mass, spring constant and damping constant. Latter one can be determined analytically, numerically and by setting up an experimental design. Numerical and analytical solutions have the advantage that they don't afford expensive manufacturing of test samples and don't need test equipment. However, mathematical solutions have to be accurate in order to be of advantage for the design process.

To investigate the benefit of analytical and numerical damping calculations for the design process of micromachined transducers, capacitive MEMS prototypes with varying damper geometries were produced and an experimental setup was engineered. The setup contains a custom made vacuum chamber and a custom made shaker unit. Both allow the analysis of the damping behavior in the continuum flow and in the slip flow regime. Especially the latter regime is important for capacitive transducers as it is an often found condition in microstructures due to small geometry dimensions.

The analytical solution of the damping behavior shows differences compared to experimental data. This is in consequence of tight boundary conditions in order to solve analytical equations. Furthermore, not all conditions in the prototyped microstructure are regarded in state of the art solutions. Despite this, analytical equations are a sufficient method for the first designs iteration of micromachined transducers. In contrast to the analytical data, numerical data are corresponding with experimental data. This is due to the fact that the boundary conditions of the prototype devices are mainly included in the simulations model. However, configuration parameters of the numerical Navier-Stokes simulation are based on analytical calculations. Therefore, both approaches, analytical and numerical, are necessary for the design of tailored transducers, especially if complex geometries with a broad set of boundary conditions are used.

ISBN: 978-3-901578-23-6